Natural convection in single slope solar stills

Benhadji Serradj Djamal Eddine

A thesis submitted to
Auckland University of Technology
In fulfilment of the requirements for the degree of

Doctor of Philosophy

2022

School of Engineering, Computer and Mathematical Sciences

ABSTRACT

Solar thermal distillation systems remain one of the most viable solutions to mitigate water crises in arid locations. Previous research has shown that single slope solar stills remain the simplest and lowest-cost means of desalination in off-grid rural or remote environments. Improved potable water production from these structures is primarily dependent on the natural convection inside the still, and this has been the subject of numerous studies. Natural convection inside single slope solar still enclosures is affected by the geometrical parameters of the cavity. However, the numerous existing correlations that have been developed for solar stills, including the most used equation of Dunkle [1], do not consider the fact that the cover angle and the aspect ratio (the absorber length over the mean height of the still) may play a role in the volume of water produced by these systems. Moreover, a comprehensive review of the literature revealed that when cover angle and cavity aspect ratio of single solar stills was considered, the results were often in conflict between studies.

As a pilot study, this research first investigated the validity of the previously developed correlations (from literature) by constructing, instrumenting and operating a single slope solar still. The data from these experiments was compared with results from thermal models using the literature correlations. These results clearly indicated that the previous correlations overpredicted the magnitude of natural convection and the yield by 30% to 130%. From this pilot, it was clear that a much more detailed parametric study was required to determine and understand the relationship between natural convection and the internal geometry of the still.

To address this issue, computational fluid dynamics simulations (CFD) were undertaken for a single slope solar still with cover angles between 0^{o} and 60^{o} and aspect ratios ranging from 8 to 1.2, with the results validated experimentally using particle image

velocimetry. It was found that both aspect ratio and cover angle significantly altered the heat transfer coefficient, with changes arising from mono- and multicellular flow patterns. These changes in the flow directly impacted the convective heat transfer coefficient, consequently, an improved correlation for Nusselt number was developed. The correlation was then verified against existing experimental data for different angles and aspect ratios, a good agreement was found in predicting distilled water production.

Having found that multicellular flow increased the natural convection in a single solar still geometry, it was decided to investigate the use of baffles as a means of altering the flow inside these devices and encouraging multicellular flow. To address this issue, the study examined the effect of vertically mounted passive baffles on the natural convection inside a single slope solar still geometry, again using CFD. These simulations explored the effect of baffle length and position on natural convection inside solar still with cover angles from 10˚- 60˚ and were validated experimentally using particle image velocimetry. The results showed that baffles did have a marked impact on the natural convection flow field and could increase the natural convection heat transfer coefficient. However, it was also found that in some cases the baffle obstructed the flow hence decreasing heat exchange between the boundary layers. The work led to the development of a relationship to describe the effect of baffles on natural convection, that will aid designers of single slope solar stills in the future.

Finally, a daily performance comparison between conventional and baffle single slope solar still was performed using both developed correlations. The results showed that both aspect ratio and cover angle have a direct effect on the water production and efficiency of both solar stills. Furthermore, the solar still equipped with a baffle delivered a higher yield of fresh water than that of the conventional single slope solar still geometry across different aspect ratios and cover angles.

By investigating natural convection inside single slope solar stills in a generalisable way, this work has, for the first time, demonstrated the relationship between the aspect ratio, cover angle, convective heat transfer coefficient and still yield. Moreover, the study has shown that the inclusion of a passive baffle can enhance solar still performance. Combining these elements, this research constitutes a major advance in the knowledge of single slope solar still design.

TABLE OF CONTENT

CHAPTER 3: A GENERALISED RELATIONSHIP FOR MODELLING THE EFFECT OF GEOMETRY ON NATURAL CONVECTIVE HEAT TRANSFER IN A SINGLE SLOPE SOLAR STILL 59

CHAPTER 4: INVESTIGATING THE INFLUENCE OF MOUNTED BAFFLE LENGTH AND POSITION ON THE NATURAL CONVECTION INSIDE SINGLE SLOPE SOLAR STILL GEOMETRY 88

LIST OF FIGURES

LIST OF TABLES

NOMENCLATURE

AR:	Aspect ratio
A_B:	Basin area (m^2)
A_W:	Area of water layer (m^2)
A_G:	Area of glass (m^2)
A_p:	Characteristic length of heat loss from basin to water
C:	Constant
C_B:	Heat capacity of the basin (j/kg.K)
C_{pa}:	Specific heat of air (j/kg.K)
C_W:	Water heat capacity (j/kg.K)
C_G:	Heat capacity of the glass (j/kg.K)
B:	Base (m)
b:	Baffle horizontal position (m)
d:	Baffle heigh (m)
d_p:	Tracer particle diameter (m)
D:	Specific height of baffle (m)
g:	Gravity (m/s^2)
Gr:	Grashof number (m)
H_l:	Front height (m)
H_r:	Back height (m)
$h_{cB\text{-}W}$:	Convective heat loss from basin to water ($W/m^2.K$)
$h_{c\ W\text{-}G}$:	Convective heat loss from water to glass ($W/m^2.K$)
$h_{e\ W\text{-}G}$:	Evaporative heat loss from water to glass ($W/m^2.K$)
$h_{r\ W\text{-}G}$:	Radiative heat loss from water to glass ($W/m^2.K$)
$h_{r\ G\text{-}S}$:	Radiative heat loss from glass to sky ($W/m^2.K$)
$h_{c\ Ins\text{-}A}$:	Convective heat loss from insulation to ambient air ($W/m^2.K$)
I_t:	Total irradiation (W/m^2)
L:	Characteristic length
L_B:	Basin thickness (m)
L_{ply}:	Plywood thickness (m)
Lins:	Insulation thickness (m)
Lmax:	Highest characteristic length at constant cover angle (m)
L_v:	Latent heat of condensation (j/kg)
M_B:	Mass of basin (kg)

M_c Mass or mole flux of water evaporated at cover level (kg/m^2.s)

M_h Mass or mole flux of water evaporated at water level (kg/m^2.s)

M_W: Mass of water (kg)

M_{ew}: Cumulative water yield (kg)

$\dot{m}_{ew}$: Instantaneous yield (ml)

n: Constant

Nu’: Modified Nusselt number

Nu: Nusselt number

P_B: Perimeter of basin (m)

P_W: Partial pressure at water layer (N/m^2)

P_G: Partial pressure at glass (N/m^2)

P(T): Partial pressure variation with temperature (N/m^2)

Ra’: Modified Rayleigh number

Ra: Rayleigh number

R: Coefficient of determination

T_B: Basin temperature (^{o}C)

T_c: Temperature of cold surface (^{o}C)

T_h: Temperature of hot surface (^{o}C)

T_W: Water temperature (^{o}C)

T_A: Ambient temperature (^{o}C)

T_S: Sky temperature (^{o}C)

T_G: Glass temperature

t: Time (S)

U_{G-A}: Total heat loss from glass to ambient air (W/m^2.K)

U_{B-A}: Total heat loss from basin to ambient air (W/m^2.K)

U_g: Gravitational induced velocity (m/s)

v: Wind velocity (m/s)

ΔT: Temperature difference between water and glass (^{o}C)

$\Delta T'$: Modified Temperature difference between water and glass (^{o}C)

Y^+: Yplus value

α_b: Basin absorptance

α_g: Glass absorptance

α_w: Water absorptance

ρ_p: Density of tracer particles (kg/m^3)

ρ_w: Reflectivity of water

ρ_p: Density of tracer particles (kg/m^3)

ρ_{sil}: Silicon oil density (kg/m^3)

ρ_a: Reflectivity of basin

ρ_g: Reflectivity of glass

ρ_W: Water density (kg/m^3)

τ_g: Transmissivity of glass

τ_w: Transmissivity of water

τ_s: Response time

λ_W: Water conductivity (w/m.ºC)

λ_{hair}: Conductivity of humid air (w/m.ºC)

λ_{air}: Conductivity of air (w/m.ºC)

ε_W: Water emissivity

ε_G: Glass emissivity

μ_{sil}: Dynamic viscosity of silicon oil (Pa s)

θ: Cover angle (º)

LIST OF PUBLICATIONS

Benhadji Serradj, D.E., T.N. Anderson, and Nates, R., The use of passive baffles to increase the yield of a single slope solar still. Solar Energy, 2021. 226: p. 297-308.

Benhadji Serradj, D.E., T.N. Anderson, and Nates, R., 2021, “The effect of passive baffles on the thermal performance of single slope solar still”, Proceedings of the Asia-Pacific Solar Research Conference 2021, Sydney, December 2021.

Benhadji Serradj, D.E., T.N. Anderson, and Nates, R., 2019, “Predicting the yield of a single slope solar still: A comparison of models”, Proceedings of the Asia-Pacific Solar Research Conference 2019, Sydney, December 2019.

Benhadji Serradj, D.E., T.N. Anderson, and Nates, R., 2019, “A numerical study of heat transfer inside a single slope solar still”, Proceedings of the 11th Australian Natural Convection Workshop, Massey, November 2019.

ATTESTATION OF AUTHORSHIP

I hereby declare that this submission is my own work and that, to the best of my knowledge and belief, it contains no material previously published or written by another person (except where explicitly defined in the acknowledgments), nor material which to a substantial extent has been submitted for the award of any other degree or diploma of a university or other institution of higher learning.

Auckland: 21/02/2022 Signature

Benhadji Serradj Djamal Eddine

ACKNOWLEDGEMENT

First and foremost, I would like to praise Allah the Almighty, the Most Gracious, and the Most Merciful for His blessing given to me during my study and in completing this thesis.

I Would like to express my sincere gratitude to my supervisors Assoc/Prof. Timothy Anderson and Assoc/Prof. Roy Nates, for the encouragement and their support provided during the course of my PhD journey. Their involvement as supervisors has developed myself as an academic through critical appraisal and helpful discussions. Without their guidance over the 4 years, the completion of this thesis may have not come to fruition.

I extend my gratitude to the Auckland University of Technology (AUT) for providing me with all equipment and space to carry out my research. I would like also to thank the staff of the Mechanical and Electronic Workshops (especially Stephen Hartley) for machining of mechanical components and setting up the equipment to carry out experiments.

A very special gratitude goes out to the New Zealand government and AUT scholarship office staff for their crucial support during my stay in New Zealand.

I would like also to thank my parents, Nour Eddine Benhadji Serradj and Nassima Bouchaour for their love and support, without them, this day would not have been possible. Also, sincere thanks to my lovely wife RabahAllah Nesrine, my sister Hafsa, my brother Mohamed for their continuous moral and emotional support.

Finally, I would like to thank my brother (from another mother) Sulaiman for his guidance and my friends Si Thu and Delight for their support in my difficult times.

CHAPTER 1: LITERATURE REVIEW

1.1. Overview

Even though Earth is called the blue planet, many countries in the world are vulnerable to water shortages as highlighted in Figure 1 [2]. In fact, fresh water represents 2% of the total available water on earth, and only 0.008% is in form of easily accessible surface water [3]. With population growth, increasing industrial activities and the rising temperature of the globe, the world's water resources continuously decrease and threaten the lives of over 1 billion people over the world. With water being the backbone of many industrial and domestic processes worldwide, its availability remains one of the main challenges currently faced by humanity [4]. It is estimated that by 2030 water demand could exceed water supply by about 40%, and close to half of the global population would be facing water shortages [5, 6]. Historically, most civilisations arose in regions where fresh water was abundant and fertile lands were available. However, freshwater accessibility was not always guaranteed. Therefore, humankind has been forced to develop means to convert underground and sea water to a clean form, though the use of desalination techniques [7].

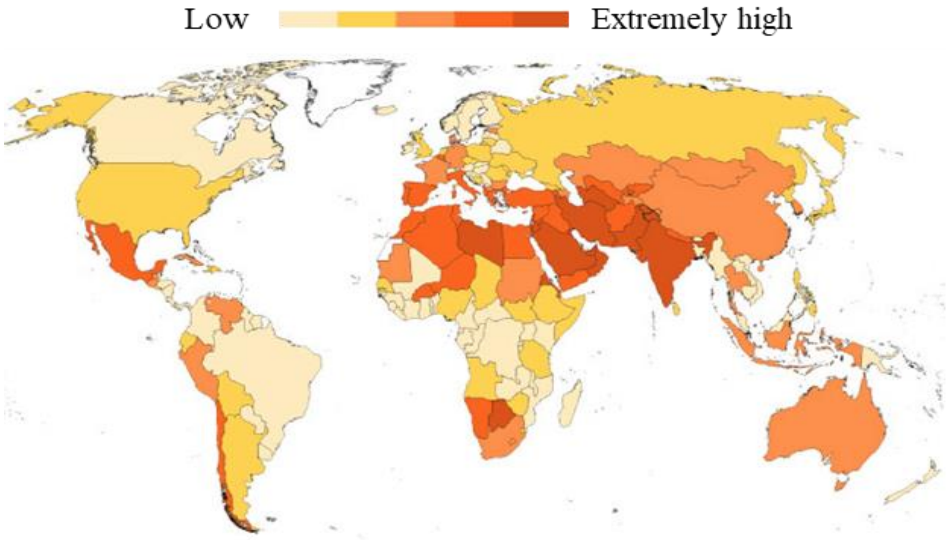

Figure 1: Water scarcity in the world [2].

1.2. Desalination Techniques

One of the oldest and simplest means of water desalination used by human beings involves evaporation and condensation using energy from the sun. The first description of solar desalination process goes back to (BC 384-322) when the Greek physicist Aristotle reported that the water produced from condensation is “sweet” [7]. The first reported solar desalination system where solar irradiation was directed to a bottle filled with seawater using a polished Damascus mirror was attributed to an Arabian alchemist in the middle ages [7]. As a result of the extensive use of water, rapid progress in technology lead to the development of several desalination technologies. These methods are divided into two general groups: thermal and non-thermal processes (Figure 2) [8].

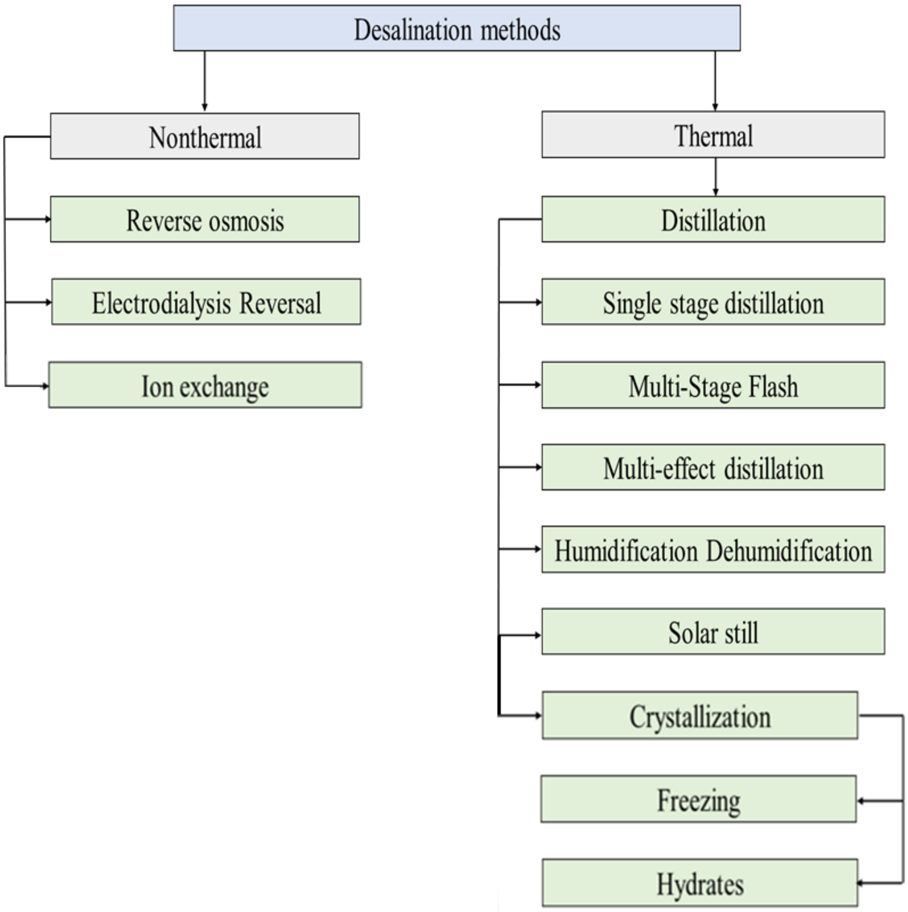

Figure 2: Desalination techniques [8].

1.2.1. Nonthermal Processes

One of the most common techniques used in non-thermal processes is reverse osmosis. The principal requirement of the reverse osmosis technique is the supply of sufficient pressure to the system in order to overcome the osmotic pressure of sea water. This creates a reverse flow, which allows the filtration of fresh water molecules from salt content through synthetic membrane (Figure 3) [8]. No phase separation and heating are required. However, there are four major components in the plant: feed water pre-treatment, membrane separation, high-pressure pumping, and permeate post-treatment. Since 1973 reverse osmosis has been commercialised all over the world, and now representing 50% of all existing desalination plants. Despite all its advantages, reverse osmosis is considered to be an energy intensive technology due to the high pressure required. Moreover, the regular maintenance due to membrane fouling increases the cost making from it cost effective only for large scale projects [9].

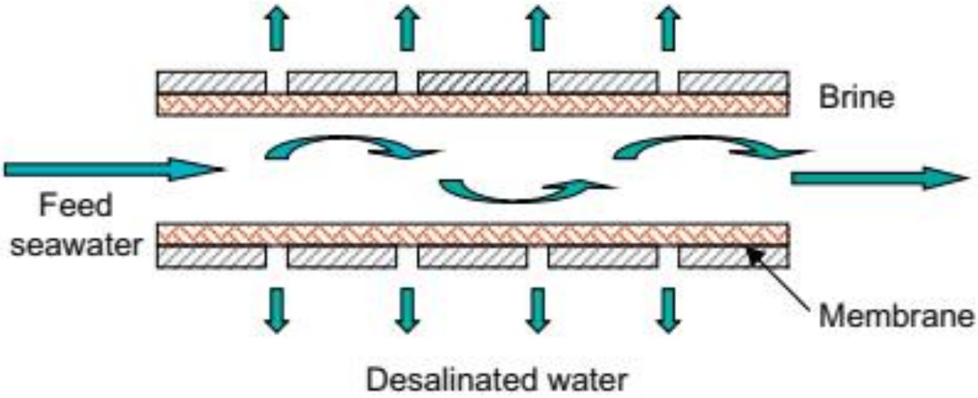

Figure 3: Reverse osmosis process [8].

Electrodialysis and electrodialysis reversal are water desalination processes in which electricity is supplied to electrodes to pull molecules of salt through an ion exchange membrane and separate the water from the salts. Due to the applied electric field, anions move toward the anode and cations to the cathode (Figure 4) [8]. The energy required for these systems is proportional to the salinity of the feed water. These techniques are used where highly purified water is required by the pharmaceutical and food industry. The difference between the two methods is the reversal of electrical potential polarity in electrodialysis reversal which reduces significantly scale growth on the membranes [10].

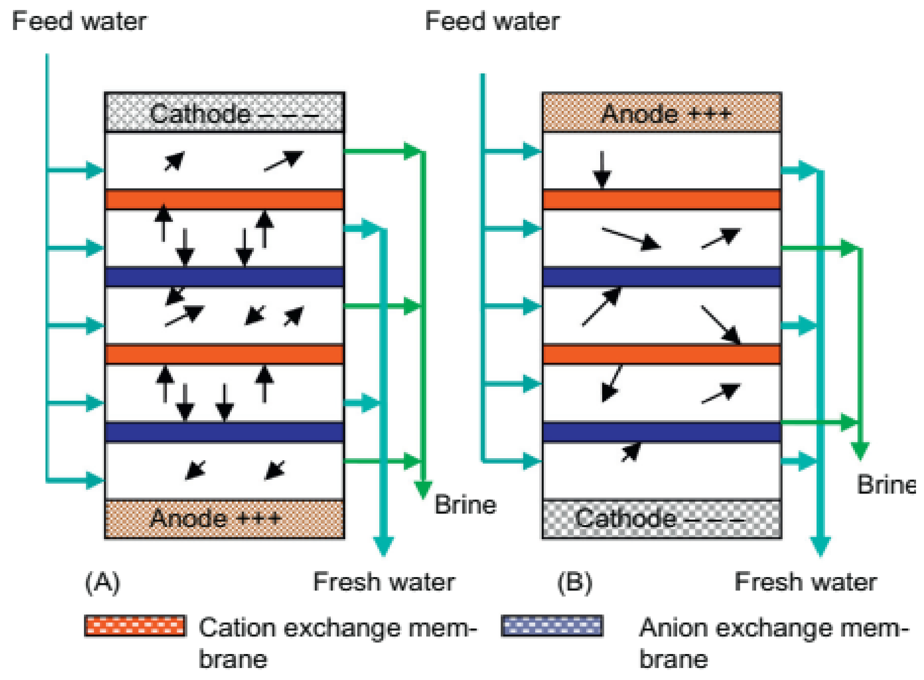

Figure 4: Electrodialysis process [8].

1.2.2. Thermal Processes

Contrary to non-thermal processes, thermal desalination techniques use heating and cooling to achieve phase changes. To induce solidification or evaporation of contaminated water, sufficient heat is added or removed. In the case of evaporation, condensation occurs by the removal of the latent heat of condensation from the water vapour. The collected condensate is pure water, leaving behind all impurities. On the other hand, in case of low temperature technologies, formation of crystals allows the creation of pure water.

Crystallisation entails either the freezing of salty water or hydrate formation. First, freezing is considered to be one of the simplest procedures to produce pure water. This is because, when sea water freezes, crystals (pure water) form, leaving dissolved salts in the solution. On the other hand, Hydrate Formation is an alternative method for producing water crystals using other substances such as propane or butane. However, to date these processes have not been commercialised due to the numerous challenges occurring in the course of operation [8, 11].

Figure 5 shows the working principle of a single stage distillation [12]. In this system, sea water is evaporated by directly supplying heat into the evaporation chamber. Subsequently, the water vapour produced is fed to the condenser where cooling water removes heat from the vapour which produces distilled water. The single stage distillation technique is considered economically viable when a compact size of desalination system is required. It is noted that the performance of single stage distillation technology depends greatly on the amount of energy supplied to the system as there is no heat recovery from the condenser. This challenge has been surmounted by the introduction of multi-stage flash and multi-effect distillation technologies.

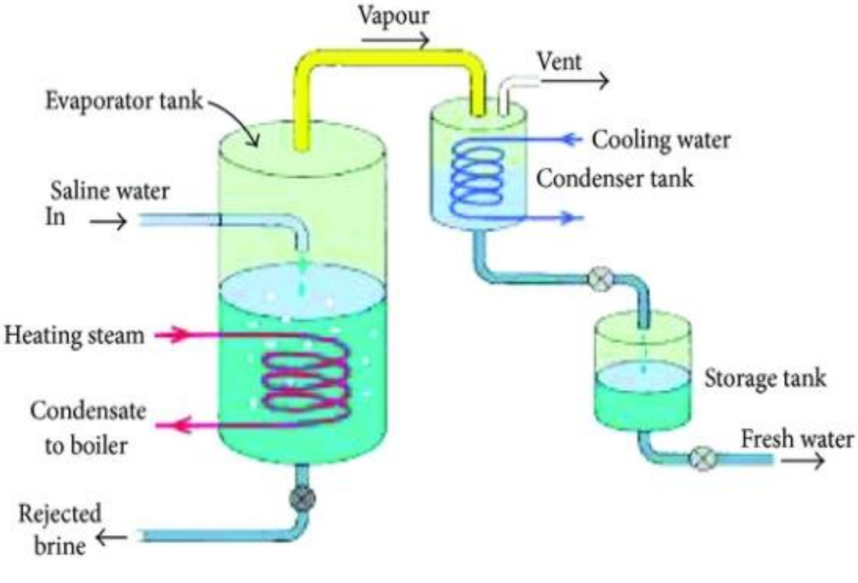

Figure 5: Single stage distillation [12].

Multi-stage flash desalination is a low-temperature desalination technique: a series of heat exchangers are used to evaporate sea water. As shown in Figure 6, cold sea water is injected to remove the latent heat of condensation from water vapour in the heat exchangers [8]. Like multi-stage flash technique, the multi-effect distillation working principle relies on the use of multiple heat exchangers in series each operating at lower pressure than the previous one, however, in the latter systems latent heat of condensation is reused to achieve higher efficiencies. To increase the produced water in multi-stage flash technique and multi-effect distillation systems, a higher energy input is required to achieve higher sea water temperature as well as low pressure after each stage. However, it was reported by Zhao J. et al [13], that high temperatures increase the deposit of scale in heat exchangers walls. Both techniques are considered economically feasible only at medium or high capacity.

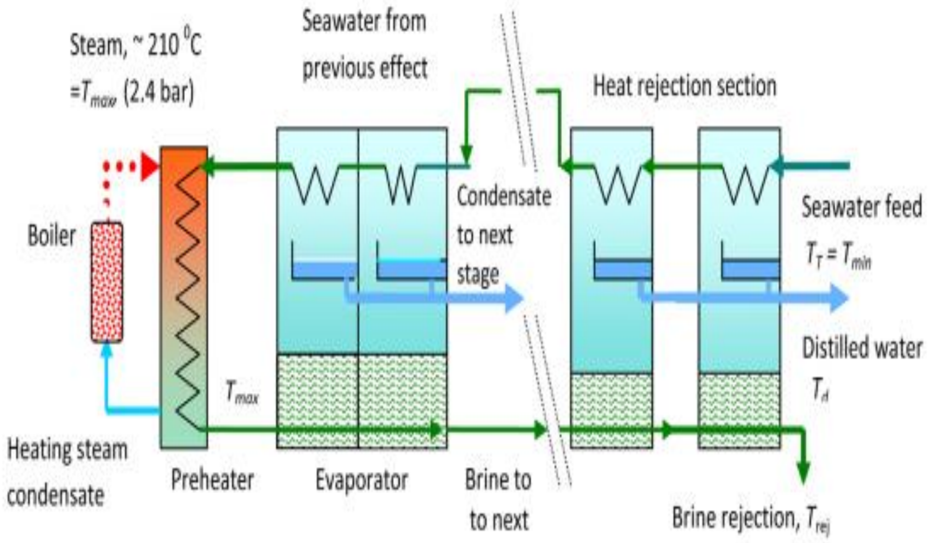

Figure 6: Multi-stage flash desalination technique [8].

Figure 7 shows a humidification-dehumidification desalination system in which two separate chambers or towers are required for the evaporation (humidification) and condensation (dehumidification) processes. An external heater like a flat plate solar collector is used to increase the temperature of sea water and transferred to the first chamber (humidifier) to humidify the air. Subsequently, humid air from the humidifier is cooled and condenses, producing distilled water.

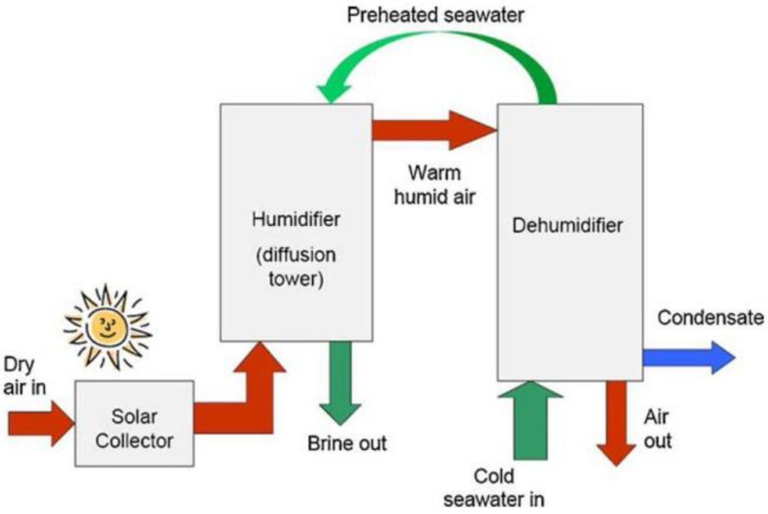

Figure 7: Humidification Dehumidification process [14].

Solar stills are considered to be the simplest solar powered method for water desalination [7]. Solar irradiation penetrates the enclosure through the glass and gets absorbed by the basin below which is usually painted black. Due to the increased temperature of the absorber, brackish water evaporates from the basin (absorber) and the pure vapour rises to the glass cover where it condenses due to cooling from the ambient air. Because of the glass slope, water droplets trickle down where they get collected in channels as shown in Figure 8. Solar stills are considered to be passive when the heat and mass transfer occur due to natural convection, however, if any component is introduced to enhance the productivity (e.g. fans, pumps, electric heater), the solar still is considered to be active. Several parameters can be used to classify passive solar stills, for example, heat storage, cavities shape, materials and number of basins.

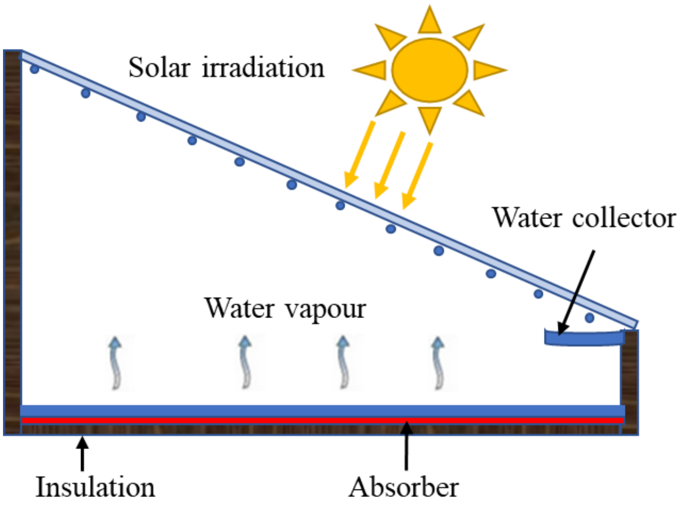

Figure 8: Solar still.

The main advantages of passive solar stills are: simple system (easy to construct and accommodate according to the preferred geometry), low investment costs because the materials are widely available, variety of possible design configurations and easy to operate and maintain in remote areas. Passive solar stills are considered a clean solution for treating water since they do not require any other sources of energy apart from solar irradiation, thus there is no effect on the environment. Furthermore, passive solar stills utilise solar energy to directly evaporate the fresh water from salt-water leaving behind concentrated brine. In this regard and given the different advantages that solar stills present, this technology is still widely used around the world [7].

1.3. Parameters Affecting Solar Still Performance

In order to increase the yield of passive solar stills, several researchers investigated the effect of different operating conditions, climatic conditions, and design conditions on its performance [15].

1.3.1. Operational Conditions

Operational conditions affecting the yield of solar stills, including salt concentration, surfactants additives, nanofluids and water colouring have been subject of many investigations. It has been demonstrated in many studies that salt concentration has an effect on productivity [16-18]. Dumka et al. [16] reported that, increasing the concentration of salt in water decreases the yield. This is because of the increased surface tension leading to a lower convective and evaporative heat transfer coefficient. Moreover, high concentrations of salt in water increase the chances of corrosion of solar still components.

It is known that adding surfactants reduces surface stress by reducing skin friction in tubes and enhancing boiling heat transfer, thereby increasing the productivity of solar stills. Nazmul et al. [19] demonstrated experimentally that increasing the concentration of surfactant in impure water increases the yield. Among surfactants that have been utilised are sodium lauryl sulphate, sodium dodecylbenzene sulfonate and polyoxymethylene tridecyl ether.

To increase the absorbed solar irradiation in solar stills, colouring the water using a dye was also found to be effective. To enhance the radiation absorbance of water, various concentrations of several dyes i.e., black naphthylamine, red carmoisine and dark green can be utilised [20]. Rajvanshi and Anil [21] demonstrated experimentally that the efficiency of a solar still can be enhanced by up to 29% by using dyes. However, the selection of dyes needs to be carefully studied as they can affect the quality of the produced water making it unsafe for human consumption [20].

The use of nanoparticles to increase the performance of solar stills has been the interest of many researchers in the field of solar desalination. Due to their thermal and optical properties, nanoparticles were found to increase the efficiency of solar stills by up to 30% by Hasanianpour et al. [22]. Several studies investigated the optimum configuration of nanoparticles while also considering both the cost, and the physical properties of the particles which depend on the size (i.e., 20 nm 40 nm and 60 nm) and the material (i.e., aluminium oxide, zinc oxide and tin oxide) [23].

1.3.2. Weather Conditions

Working under non-controlled outdoor conditions, solar stills are subject to the effect of different weather conditions such as solar irradiation, wind velocity, ambient temperature and dust deposits. Solar irradiation is considered to be the most vital factor affecting solar still performance, this is due to the irradiation being the only energy input of the system. Small increases in solar irradiation increase the yield enormously. Consequently, several researchers tried to incorporate mirrors into solar stills in order to increase the incident solar irradiation. Numerous experimental and numerical studies have successfully demonstrated the strong relation between solar irradiation and solar still yield, see [24, 25].

Driven by the temperature difference between the water and the glass cover, natural convection in the still is strongly dependent on weather conditions. When the ambient wind carries more heat from the glass cover through convection, the temperature difference increases resulting in a higher yield. Several researchers investigated the effect of wind velocity on the yield; results show an increase in the yield when moderate wind velocity (v) ($1 \text{ m/s} < v < 4 \text{ m/s}$) is encountered [15]. However, it was also observed that excessive wind speeds (9 m/s) increase heat losses from the glass cover and absorber leading to a low temperature difference that adversely affect solar still by reducing its efficiency up to 13% [26].

There has been extensive research on the effect of ambient temperature on solar still yield. Experimental work has shown that it is preferable to have a solar still in an environment with a high ambient temperature, in fact an increase in ambient temperature of 10ºC can increase the yield by up to 10% because evaporation rate is proportional to water layer temperature. Further theoretical investigations demonstrated that the overall effect of ambient temperature is small as increasing the temperature by 5 ºC increases the yield only by 3% [27].

1.3.3. Geometry and structure

During the design stage of solar stills manufacturing process, the best shape geometry needs to be selected to increase the water yield. Several researchers have examined and investigated the performance of different shapes, some of the most studied geometries are shown in Figure 9. Aiming to increase the performance of Single Slope (SS) solar still shown in Figure 9 (a) by improving received solar irradiation and natural convection, many studies attempted designing different cover shapes as shown in Figure 9 (b-f), however, in many cases authors have reported the better performance of SS solar still over other geometries [28].

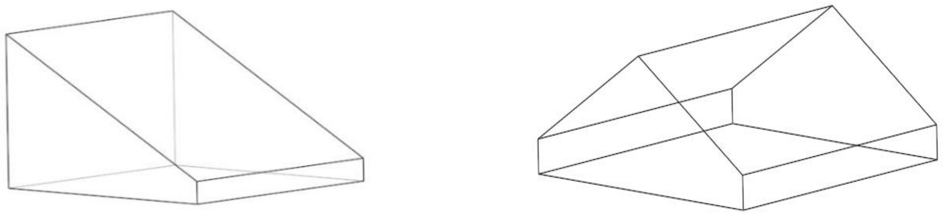

a: Single slope b: Double slope

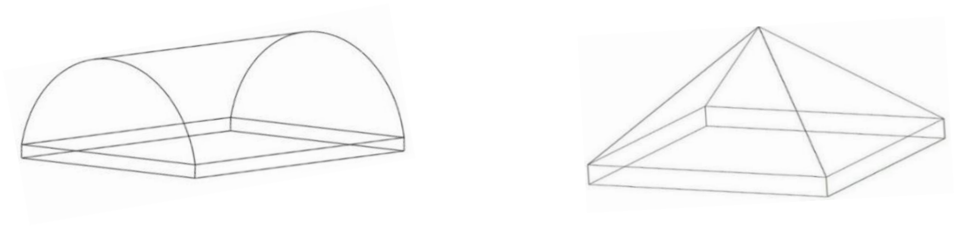

c: Parabolic d: Pyramid

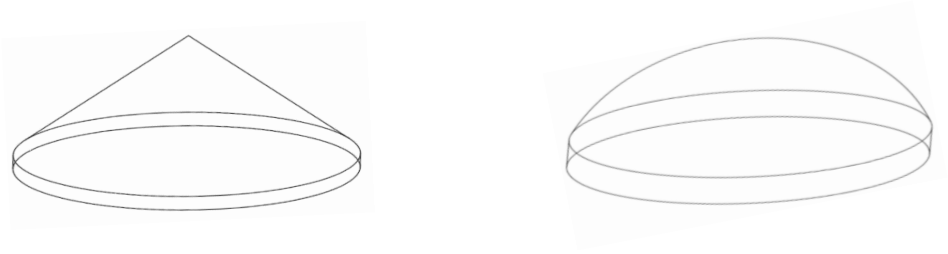

e: Cone f: Hemisphere

Figure 9: Solar still shape designs.

Among all existing geometries, the SS solar still as shown in Figure 9 (a), is usually referred to as the oldest geometry used for water distillation using solar energy, and frequently serves as the basis of comparison with other designs [28]. Moreover, the simple geometry of the SS solar still makes it easier to construct with easily accessible materials and at much lower cost. Therefore, the passive SS solar still is believed to be a promising option for water distillation in arid regions especially in remote areas [11, 22, 29, 30].

Over the years extensive research has been carried out in an attempt to enhance the productivity of SS solar still. Several inventive methods, such as utilising different absorber materials [31, 32], including thermal energy storage [33, 34], , adding external condensers [35, 36], adding features to increase the absorption area [37, 38], using fins within the enclosure [39, 40], using mirrors to increase the incident radiation [41, 42] and varying the cover tilt angle and aspect ratio [43-45] have all been examined. Given this extensive body of literature, the area has also been the subject of research reviews describing the different parameters that influence the performance of single slope solar stills [46, 47].

In general, the heat transfer in solar stills is divided into two parts: internal and external heat transfer. Internal heat transfer occurs through convection, evaporation and radiation, whereas the external heat transfer happens in form of conduction, convection, and radiation. The internal heat transfer results in transferring pure water vapour through a mixture of air and vapour reaching the glass cover where the external heat transfer (due to wind) causes the heat loss that will allow condensation of water vapour. Among all heat transfer processes that are involved in SS solar stills, modelling of the convective and evaporative heat transfer coefficients has been the subject of much research [1, 48-

54]. This is because potable water production from these structures is primarily dependent on heat exchange between the water and glass cover.

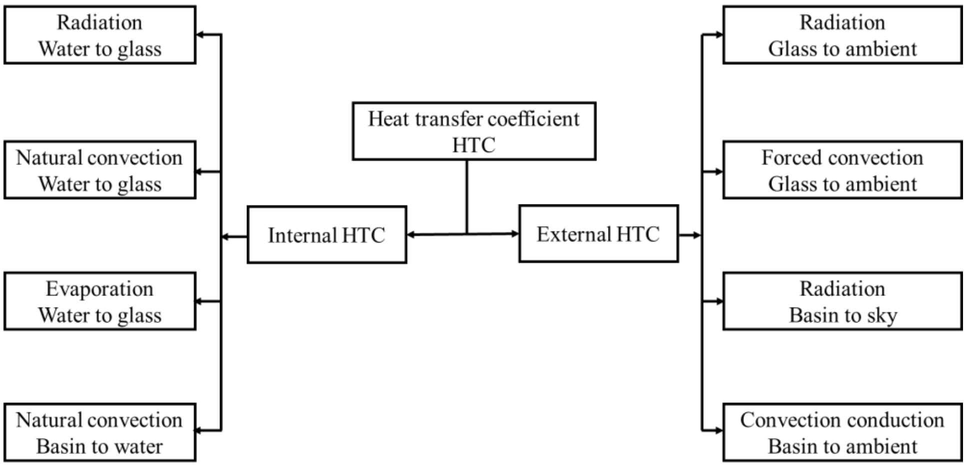

Figure 10: Solar still heat transfer

In solar stills, natural convection heat transfer between the water surface and glass cover is responsible for providing the energy needed for evaporative heat transfer to take place, with the two mechanisms linked through the Chilton-Colburn analogy between heat and mass transfer, an improved understanding of the natural convective heat transfer has formed the basis of many studies looking to determine or improve the yield of SS solar still. Nonetheless, several researchers over the years have attempted to develop correlations to estimate the magnitude of natural convection. Other researchers have investigated the effect of the geometry variation such as changes in the cover angle (θ) and aspect ratio (the breadth of the still divided by the mean height B/L) on natural convection heat transfer coefficient, thus the solar still productivity (Figure 11).

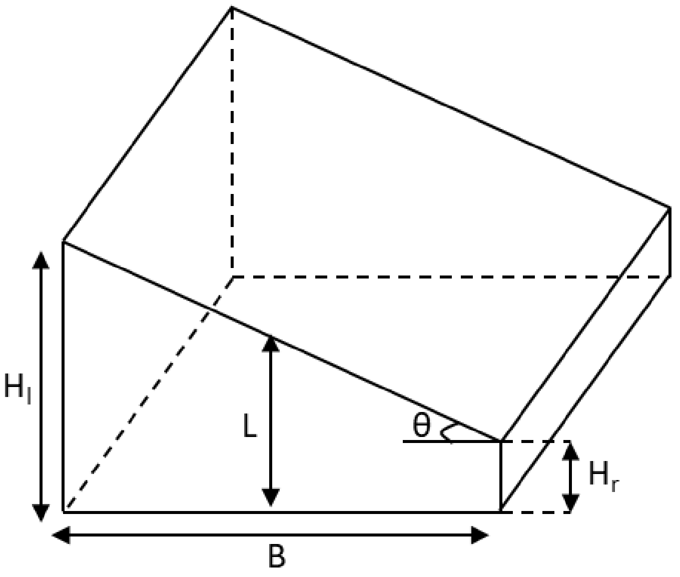

Figure 11: SS solar still geometry.

One of the oldest and most widely used approaches to describe the heat transfer exchange between the glass cover and water basin is Dunkle's correlation [1]. To develop his equation, Dunkle [1] used the correlation developed by Jakob and Max [55] using experimental data published by Mull and Reiher [56] for a flow between two close parallel plates. By assuming a temperature difference and a mean air temperature of 50 ˚C and 17 ˚C, respectively, Dunkle deduced a correlation independent from the solar still geometry and air properties. In this respect it is a poor representation of the geometry seen in a typical SS solar still and limits the ability to undertake a systematic analysis of SS solar stills. This equation has been widely used [16, 57-69] to estimate the convective heat transfer coefficient. To overcome the shortcomings of Dunkle's correlation, numerous alternative correlations have been developed by researchers over the years [24, 48-50, 52, 53, 70-74], principally addressing the convective heat transfer coefficient.

Due to the limitations of Dunkle's correlation, Clark [74] experimentally examined the steady state performance of a SS solar still. This study considered stills with small inclinations of the condensing surface (≤ 15°) and found that the heat transfer coefficient was half that predicted by Dunkle's correlation. In particular, the results showed that, at high radiation fluxes, Dunkle's model overpredicts water yield from solar stills by almost 50%. To lower the predicted performance by Dunkle, Clark [74] suggested to halve the previous correlation developed by Dunkle. Clark [74] did not investigate either the effect of aspect ratio or the cover angle effect on the performance of SS solar still.

In another study, Shawaqfeh et al. [52] performed an indoor experimental investigation on a SS solar still with a cover angle of 19^o and an aspect ratio of 3.67. The study results were compared with Dunkle's model predicted yield and it was established that Dunkle's model overestimated water production by almost 30%. Based on the study's findings, a new correlation was developed to describe the heat transfer process; but although the range of Rayleigh numbers was varied (by varying the temperature difference), the aspect ratio and cover angle were not considered.

In another study, Adhikari et al. [53] developed a correlation for predicting the convective heat transfer coefficient (in the form $Nu=CRa^n$) using experimental data. However, the equation does not take into account the effect of the aspect ratio or the cover angle on the natural convection within the cavity. Using the same approach, Kumar and Tiwari [75] noted that there was a need to modify the values of C and n to predict the exact performance of SS solar stills for different ranges of Rayleigh number, suggesting a lack of generalisability. Despite this limitation, the approach has been used in other studies [25, 76, 77]. It is noteworthy that multiple C and n values are suggested in the literature using the same methodology and these are typically contradictory because of the different weather and geometrical experimental conditions [25, 53, 75, 77-80].

The natural convection in SS solar stills has also been numerically investigated by Rahbar and Esfahani [49]. In this study, computational fluid dynamics (CFD) was used to highlight the effect of Rayleigh number ($5 \times 10^6 < Ra < 5 \times 10^7$) and aspect ratio

($2.5 < AR < 5.5$) on the convective heat transfer coefficient. The effect of increasing the Rayleigh number (by increasing the temperature difference between the glass and the absorber) at a constant aspect ratio was found to increase the convective heat transfer coefficient [49]. Furthermore, at a constant Rayleigh number, decreasing the aspect ratio was found to increase the heat transfer coefficient [49]. However, study [49] did not take into consideration the effect of the inclination angle on the convective heat transfer coefficient. In the previous study, the cover angle was varied as a result of changing the aspect ratio, therefore, the conclusion on drawn on the effect of aspect ratio lacks pertinence in terms of separating the effect of aspect ratio on natural convection.

Looking to overcome the shortcoming of previous developed models, Jamil and Akhtar [48] recently developed using experimental data a new correlation to determine the heat transfer coefficient. In their study, constant cover angle of 28° was considered while the aspect ratio was varied. Therefore, the correlation developed does not take into consideration the cover angle as an independent parameter in the Nusselt equation. Results of the study demonstrated that increasing the aspect ratio increases the performance of the SS solar still. The authors believe that the increase in performance is due to the short distance between the water basin and cover glass (high aspect ratio) leading to a quicker heat exchange between the two boundary layers. The latter finding contradicts the results presented by Rahbar and Esfahani [49] who argued that low aspect ratio leads to high flow velocity inside the enclosure resulting in a greater heat transfer coefficient. Comparing the developed model results to the previously available correlations, Jamil and Akhtar [48] concluded that both the Dunkle [1] and Shawaqfeh et al. [52] correlations predict a constant heat transfer coefficient for different aspect ratios. Moreover, Rahbar and Esfahani predicts higher Nusselt number values due to the low number of cases used to generate the correlation.

Recently, Keshktar et al. [22] investigated the effect of the angle and aspect ratio on the performance of SS solar stills using transient CFD modelling. The results of the study suggested that, at a 30° cover angle, a high aspect ratio reduced productivity because of the water basin being close to the glass cover (ambient conditions). Moreover, decreasing aspect ratio resulted in a significant decrease in productivity because of the creation of large weak vortex. Within the range of aspect ratios examined, the authors reported an optimum aspect delivering the highest productivity.

An experimental investigation was performed by Azooz and Younis [44] to identify the effect of the cover angle and aspect ratio on the performance of a SS solar still. To do this, different SS solar stills were constructed with various cover angles and aspect ratios and water production data was collected over several days of experimental work. It was found that a SS solar still with a cover angle equal to 35° (equivalent to the latitude of the location) and an aspect ratio 1.8 produces less water than a SS solar still with a 25° cover angle and aspect ratio 2.4. Furthermore, high cover angles with high aspect ratio geometries were found to produce more water than solar stills with cover angle equal to the latitude 35°. As such these findings contradict the conclusion made by Jamil and Akhtar [24] and Keshktar et al. [22] regarding the selection of the optimum aspect ratio. These contradictions raise several interesting questions about the effect of geometry on performance of SS solar stills.

Knowing that such extensive research is available in the literature, it was decided to assess the choice of aspect ratio by different researchers. Figure 12 depicts the choice of aspect ratio for different theoretical and experimental studies. It can be seen that the selection is coherent and scattered for the latitude of each location. Moreover, it is clearly shown that aspect ratio is selected according to the cover angle, as increasing the angle directly decreases the aspect ratio. Therefore, one can conclude that the foundation behind selecting the aspect ratio follows the cover angle rather than the effect of this parameter has on the heat and mass transfer inside solar stills.

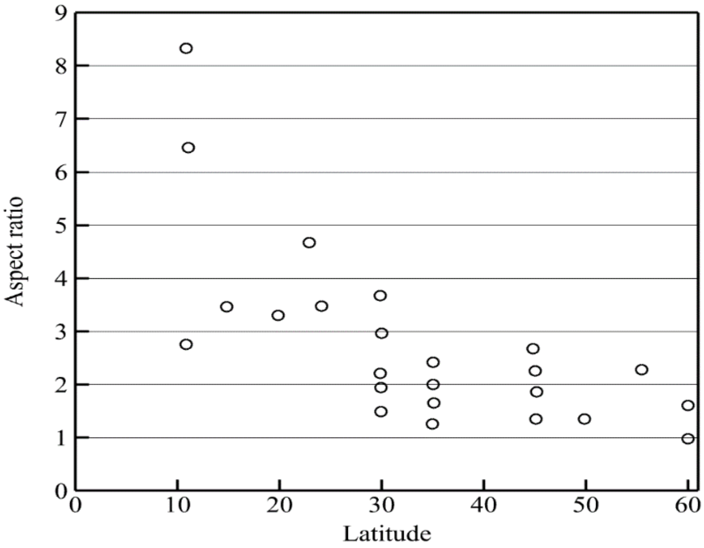

Figure 12: Aspect ratio choice across various theoretical and experimental studies [35, 48, 81-93].

With respect to the choice of the cover angle in the literature, several researchers have suggested that the angle should be equal to the latitude of the case study location [48, 94-98], or high during the winter season and low during summer, although the rationale supporting this assertion appears to be tenuous. This is because a recent study [99] has demonstrated, by using a solar ray tracing technique, that the cover angle does not affect the received solar irradiation according to the seasons of the year. As a case in point, some of the studies recorded [100] show a clear disparity between the optimum inclination angle and the latitudes of the locations under consideration. Similarly, an investigation into the optimum cover inclination angle for maximum yield in a SS solar still under New Delhi climate conditions was established to be 10° in summer [101] which is quite different to New Delhi’s latitude of 28.6° N. To fully clarify the discrepancy of angle selection, it was decided to assess, through a broad survey of the literature, the choice of angle made by several researchers in the field of solar stills. Figure 13 and 14 illustrate the variation of angle selection for summer and winter, respectively. It shows clearly that the research is scattered and does not follow a clear trend. Moreover, it can be noticed that most of the research has done at locations between latitude 20˚ and 40˚ corresponding to the latitude range of countries facing water scarcity. However, a slight tendency can be seen with regard to selecting the cover angle equal to the latitude of the location. Having said that, one can conclude that no firm conclusion or strong justifications are withdrawn concerning the selection of the cover angle.

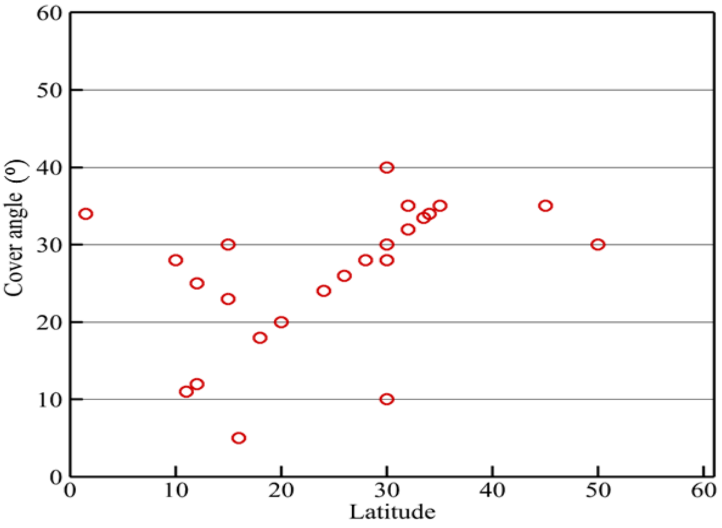

Figure 13: Summer cover angle choice across various theoretical and experimental studies [33, 35, 36, 48, 63, 87, 91, 102-122].

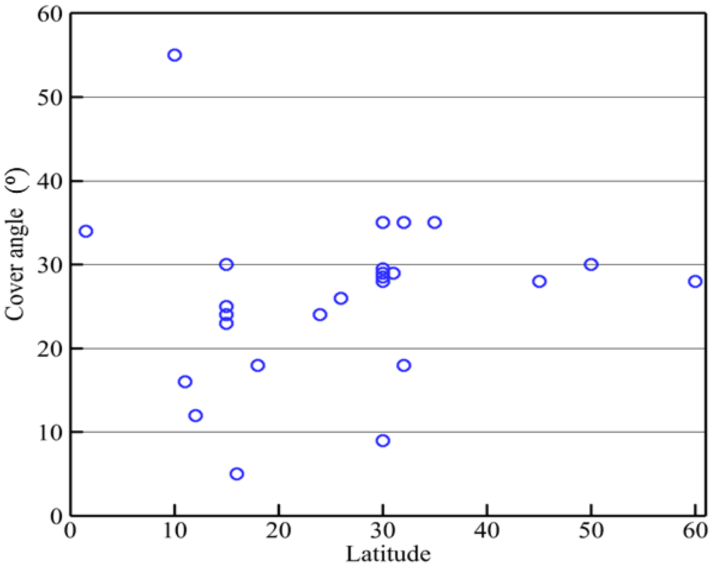

Figure 14: Winter cover angle choice across various theoretical and experimental studies [33, 35, 36, 88-91, 104, 105, 108-114, 119, 120, 123-130].

Based on the existing literature, the SS solar still has been subject of extensive research. Several researchers attempted to increase the efficiency of these devices by investigating several innovative methods such as the utilisation of different materials, external condenser etc. However, one of the challenges of these studies is that different and conflicting conclusions are drawn regarding the effect of the cover angle and aspect ratio on the performance of SS solar still. These contradictory results are also reflected on the developed correlations, making them less suitable for practitioners and researchers in this field. Based on this, it is apparent that there is a gap in knowledge and a need to deliver a better understanding of natural convection inside these devices. Therefore, the present study aims to determine:

What is the effect of single slope solar still geometry on the heat and mass transfer process, and is there a way to enhance its performance?

CHAPTER 2: MATHEMATICAL MODELLING OF SINGLE SLOPE SOLAR STILL

2.1. Introduction

To commence tackling the research question, this chapter attempts to investigate experimentally the use of the previously discussed correlations in predicting the thermal state condition of the SS solar still as well as the predicted yield. A general investigation of the SS solar still system, as well as examining the existing convective heat transfer models on the solar still thermal state conditions and yield is required. In this respect, a mathematical model of the system needs to be established.

2.2 Model development

In order to investigate the thermal performance of SS solar still, a one-dimensional steady state thermal model was established. As shown in Figure 15, the SS solar still system is composed of three main components, Basin (absorber), water layer and cover (glass). The subsequent section presents in detail the mathematical model for each of these parts. The model was developed considering the following assumptions:

- For a given Δt, the system is considered to be working under steady state conditions.
- The enclosure is perfectly sealed so that no leakage occurs from the solar still.
- The saline water properties are similar to brine water.
- The air inside the enclosure is considered to be saturated humid air.
- For a given Δt, the temperature of the basin, water and glass cover is constant and uniform.
- The side walls are perfectly insulated; thus, thermal losses are negligible.

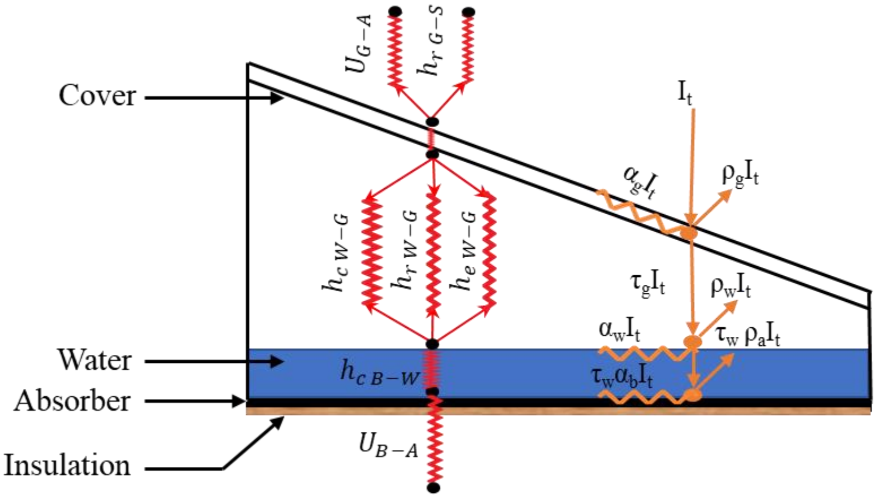

Figure 15: Resistance schematic for solar still.

Considering the above-mentioned assumptions, the energy balance equations for the different components of SS solar still were articulated as follows:

For the basin

$$C_B M_B \frac{dT_B}{dt} = \tau_W \tau_G \alpha_B I A_B - h_{c\,B-W} A_B (T_B - T_W) - U_{B-A} A_B (T_B - T_A) \tag{1}$$

For the brine water

$$C_W (M_W - M_{ew}) \frac{dT_W}{dt} = \tau_G \alpha_W I A_W + h_{c\,B-W} A_B (T_B - T_W) - h_{c\,W-G} A_W (T_W - T_G) -$$

$$h_{e\,W-G} A_W (T_W - T_G) - h_{r\,W-G} A_W (T_W - T_G) \tag{2}$$

For the glass cover

$$C_G M_G \frac{dT_G}{dt} = \alpha_G I A_G + h_{e\,W-G} A_W (T_W - T_G) + h_{r\,W-G} A_W (T_W - T_G) +$$

$$h_{c\,W-G} A_W (T_W - T_G) - h_{r\,G-S} A_G (T_G - T_S) - U_{G-A} A_G (T_G - T_A) \tag{3}$$

Where $h_{c\,B-W}$ is convective heat transfer coefficient between the basin and water layer and is calculated using bottom hot surface to top cold quiescent fluid correlation defined as [131]:

$$h_{c\,B-W} = 0.54 \times (Ra^{0.25}) \lambda / A_p \tag{4}$$

With the characteristic length A_p defined as $A_p = A_B / P_B$ and $Ra = \frac{\rho_{air}^2\, g\, \beta\, \Delta T'\, Cp_{air}\ L^3}{\lambda_{air} \mu_{air}}$

To estimate the overall losses from the absorber to the ambient environment, U_{B-A}, can be written as:

$$U_{B-A} = \quad 1/(\frac{L_{Ins}}{\lambda_{Ins}} + \frac{L_B}{\lambda_B} + \frac{L_{Ply}}{\lambda_{Ply}} + \frac{1}{h_{c\ Ins-A}}) \tag{5}$$

Where, $h_{c\ Ins-A}$ is the convective heat transfer from wood insulation to the environment and calculated using bottom hot surface to bottom cold quiescent fluid correlation defined as [131]:

$$h_{c\ Ins-A} = 0.27 \times (Ra^{0.25})\lambda_{Ins}/A_p \tag{6}$$

With $\frac{L_{Ins}}{\lambda_{Ins}}, \frac{L_{Ply}}{\lambda_{Ply}}$ and $\frac{L_B}{\lambda_B}$ represents conductive heat loss from the bottom of solar still to the ambient air.

$h_{r\ W-G}$ is the radiation heat exchange between the water surface and glass cover, and can be computed using equation 7 [131].

$$h_{r\ W-G} = 5.67\ 10^{-8}\ \times \varepsilon_w((T_W + 273.15) + (T_G + 273.15))((T_W + 273.15)^2 + (T_G + 273.15)^2)$$

(7)

The radiation heat loss from the glass cover to the ambient $h_{r\ G-S}$ was expressed as heat transfer coefficient in terms of sky temperature, glass temperature and glass emissivity as shown in the following equation [131]:

$$h_{r\ G-S} = 5.67\ 10^{-8}\ \times \varepsilon_G((T_G + 273.15) + (T_S + 273.15))((T_G + 273.15)^2 + (T_S + 273.15)^2) \tag{8}$$

Where the temperature of the sky is computed based on the measured ambient temperature as shown in equation 9 [132]:

$$T_S = 0.0552 \times T_A^{1.5} \tag{9}$$

U_{G-A} is the summation of conductive and convective heat loss from the cover surface to the ambient air and can be calculates from equation 10:

$$U_{G-A} = 1/(\frac{L_G}{\lambda_G} + \frac{1}{h_{c\ G-A}}) \tag{10}$$

With $h_{c\,G-A}$ representing the convective heat transfer coefficient loss from the cover to the ambient air induced by the wind velocity as shown in the following equation [133]:

$$h_{c\,G-A} = \begin{cases} 2.8 + 3 \times v \; for \; v \leq 5m/s \\ 6.15 \times v^{0.8} \; for \; v > 5m/s \end{cases} \tag{11}$$

$h_{c\,W-G}$ is the convective heat transfer coefficient between the water surface and glass cover, as discussed earlier, this mathematical model will consider different correlations to predict $h_{c\,W-G}$. The selected well-known models are described as follows:

- Dunkle model (1961) [1]:

$$h_{c\,W-G} = 0.884 \times [\Delta T']^{\frac{1}{3}} \tag{12}$$

With

$$\Delta T' = (T_W - T_G) + \frac{(P_W - P_G)(T_W + 273.15)}{268.9\;10^3 - P_W} \tag{13}$$

While P_W and P_G are partial pressures of humid air at water and cover surfaces, respectively, and can be calculated depending on the temperature as follows [7]:

$$P(T) = e^{\left[25.317 - \left(\frac{5144}{273.15 + T}\right)\right]}$$

- Jamil and Akhtar (2017) [48]:

$$h_{c\,W-G} = 0.0462\;(AR^{0.15})(Ra'^{0.34})(\lambda_{hair}/L) \tag{14}$$

With $Ra' = \frac{\rho_{hair}^2\, g\, \beta\, \Delta T'\, Cp_{hair}\; L^3}{\lambda_{hair}\mu_{hair}}$

- Adhikari et al. (1990) [53]:

$$h_{c\,W-G} = C\;(Gr)^n \left(\frac{\lambda_{hair}}{L}\right) \tag{15}$$

$$with \begin{cases} C = 0.21; n = \frac{1}{4} \text{ for } 10^4 < Gr < 2.51 \times 10^7 \\ C = 0.2155; n = \frac{1}{3} \text{ for } 2.51 \times 10^5 < Gr < 2.51 \times 10^7 \end{cases} \tag{15}$$

- Rahbar and Esfahani (2012) [49]:

$$h_{c\,W-G} = 0.28\;(AR^{-0.16})(Ra'^{0.25})(\lambda_{hair}/L) \tag{16}$$

To estimate the mass transfer between the water surface and glass cover, most researchers use the simplified form of Chilton-Colburn analogy defined as [1, 53, 54]:

$$h_{e\,W-G} = 0.0163 \times h_{c\,W-G} \frac{(P_W - P_G)}{(T_W - T_G)} \quad (17)$$

The rate at which distilled water is produced from the condensation can therefore be calculated from $h_{e\,W-G}$ as follows:

$$\dot{m}_{ew} = 1000 \times h_{e\,W-G}(T_W - T_G)/L_V \quad (18)$$

Accumulated water was than calculates using the following equation:

$$M_{ew} = \sum_{i=1}^{n} \dot{m}_{ew} * t \quad (19)$$

2.3. Computational solution

The purpose of this chapter was to present the different models that have been developed to estimate natural convection between water surface and glass cover, to model a SS solar still and to highlight the importance of the convective heat transfer coefficient $h_{c\,W-G}$ in predicting the thermal state condition of the distillation system.

In this respect, the inputs of the thermal model were the ambient air temperature, incident radiation, wind velocity, and operating parameters such as humid air and water properties. Figure 16 shows the iterative approach that was used to develop the solution for the SS solar still. The input (weather conditions) was measured experimentally, subsequently, thermal state conditions and distilled water production were examined and compared to the simulated results acquired from the mathematical model using the different selected correlations of convective heat transfer coefficient. The mathematical model was solved using the Fourth Order Runge-Kutta method code in MatLab R2019a.

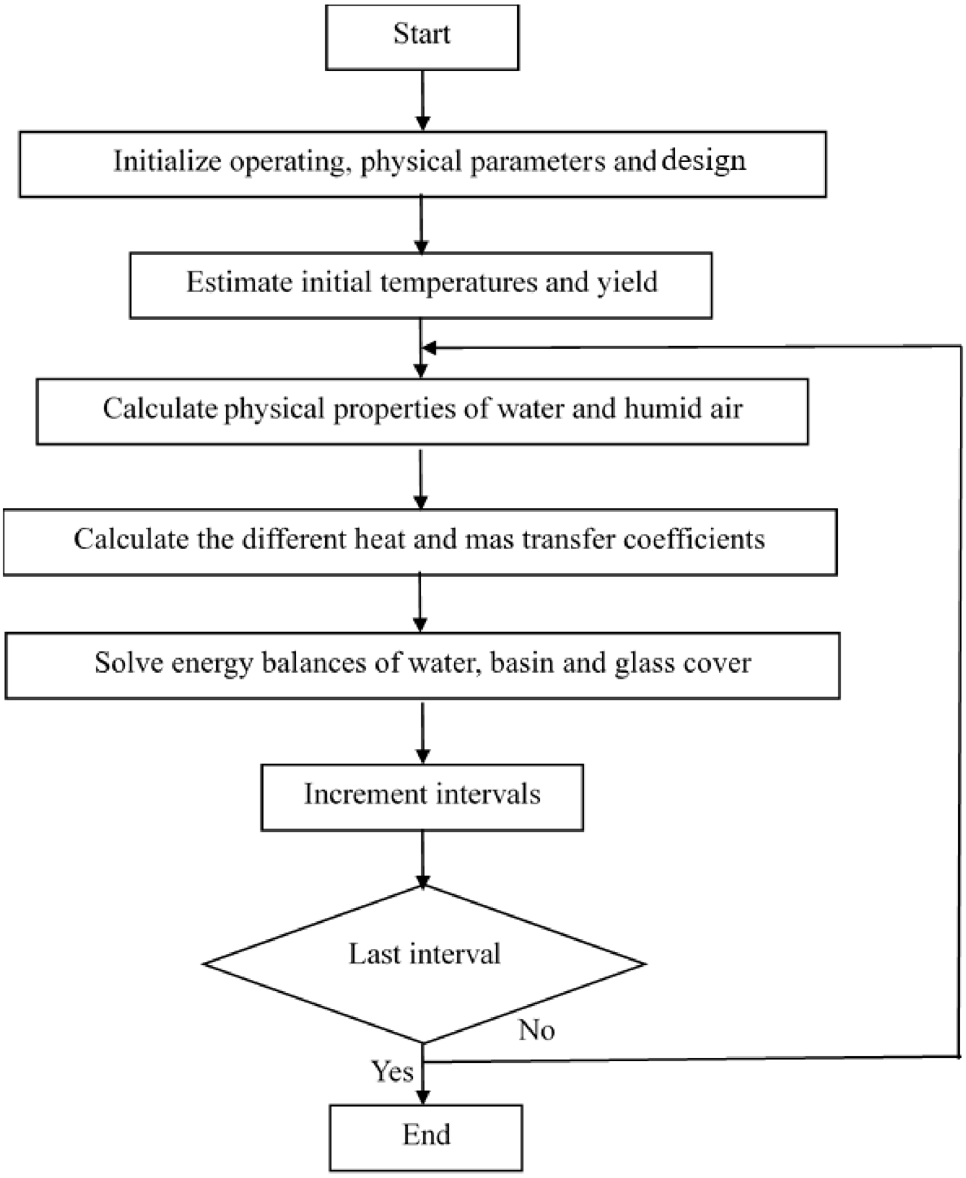

Figure 16: Flow chart of computational model.

2.4. Experimental setup

In order to properly examine the performance of the solar still, outdoor experimental work was carried out. The rationale for selecting an outdoor experiment is because the data acquired is based on the real solar spectrum. Even though it is possible to test the fabricated SS solar still under controlled “weather” conditions, reproducing constant heat flux identical to the solar spectrum is particularly challenging. Moreover, the former argument has been supported by the poor results obtained from solar simulators in replicating the uniform solar spectrum [134].

The experimental system consisted of a SS solar still and data acquisition structure. As illustrated in Figure 17, the solar still's side walls were made of low thermal conductivity plywood to reduce heat losses to the environment. To allow solar irradiation penetration, the top cover was made of low iron glass having a high transmissivity coefficient. Moreover, the inner water basin lying on the bottom surface was made of black painted (for higher solar irradiation absorption) aluminum sheet. Moreover, to reduce further heat losses from the SS solar still, all surfaces made of plywood were insulated using polystyrene sheets. The values of design and working parameters utilized in this experiment are shown in Table 1 and Table 2. The solar still was installed on the roof of the Mechanical Engineering department at Auckland University of Technology (latitude: 36.8509° S, longitude: 174.7645° E); the solar still box was fixed facing north on an unimpeded location. To start the experiment, the basin was filled with 16 kg of water as initial condition.

Figure 17: Perspective view of the SS solar still.

Table 1: Design parameters.

Parameter	Design value
Basin area	1m^2
Glass cover area	1.15m^2
Glass thickness	0.01m
Front height	0.2m
Back height	0.8m
Inclination Angle	30.0°
Plywood sheet thickness	0.01m
Polystyrene sheet thickness	0.05m
Aluminum thickness	0.003m

Table 2: Material properties [37, 135, 136].

Material	Value		Value
Density of aluminum	2710 kg/m^3	Conductivity of glass	0.8 W/m^2.K
Heat capacity of aluminum	900 J/kg.K	Absorptivity of glass	0.05
Conductivity of aluminum	250 W/m^2.K	Transmittance of glass	0.91
Absorptivity of aluminum	0.8	Absorptivity of water	0.05
Density of Plywood	600 kg/m^3	Transmittance of water	0.6
Conductivity of Plywood	0.2 W/m^2.K	Emissivity of glass	0.95
Density of glass	2500 kg/m^3	Emissivity of water	0.9
Heat capacity of glass	840 J/kg.K		

2.5. Data acquisition system

In order to compare the thermal state conditions of the system and the mathematical modelling results, it is necessary to accurately measure the inputs of the mathematical model (weather data: global incident solar irradiation, wind velocity and ambient temperature), thermal conditions (water and cover temperatures) and distilled water production. Figure 18 shows the different equipment used to instantaneously measure weather conditions. To evaluate the global incident solar irradiation which is considered as the most influential environment parameters in solar systems, a calibrated sunshine pyranometer type SPN1 class A was used. Moreover, to estimate losses due to incident wind, a Delta-T Device anemometer was selected to measure wind speed and direction. The latter was selected due to its wide range of velocity magnitude and low error percentage. Both the irradiation and wind speed sensors were installed at the same location as the solar still.

Figure 18: Location of solar still measurement sensors, 1: Data logger, 2: Anemometer, 3: Pyranometer.

The temperature of the ambient air, water and glass cover were measured using T-type thermocouples. This type of thermocouple is known for its low error percentage compared to J type and K type thermocouples [137], and was selected because the range of working temperature in solar stills is low which makes them suitable for the current experiment. To measure the ambient temperature, two sensors were installed away from the solar still in the shade at 1 metre above the ground to avoid uncertainties caused by heat losses from the stills and gains from the ground. To measure the temperature of the water layer six thermocouples have been used to reduce the effect of the no-uniform temperature. However, to measure glass temperature, only two thermocouples were used to minimise the shade on the absorber surface. Figure 19 shows distribution of the thermocouples on the water basin and glass cover. As suggested by Nishioka et al. [138], the thermocouples were equally spaced along the X and Y direction, and attached to the selected surfaces using aluminium tape (thickness 100µm).

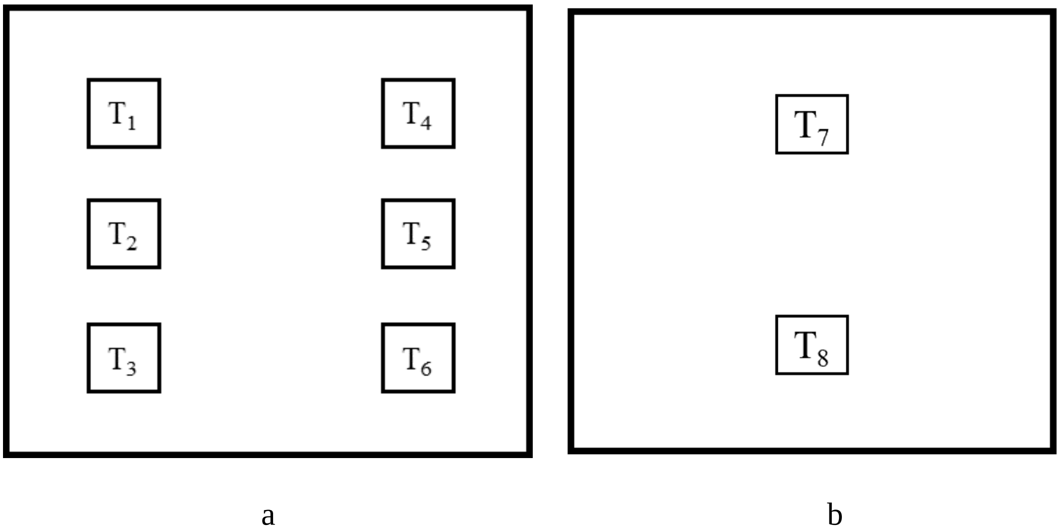

Figure 19:Thermocouples distribution, a: Water layer, b: Glass cover.

A data logger was used to save all the information captured from the sensors. Keysight 34970A Data Acquisition system was used due to its high number of channels (250) and frequent polling rate of 1scan/second. Moreover, the built-in signal conditioning reduces the errors caused by noise that can alter sensors signals [139]. To measure the collected water from the solar still, an insulated graduated beaker was used to avoid the evaporation of the yield, and measurements of produced water were conducted on an hourly basis.

The experiment was carried out simulating the climatic conditions of a typical summer day (20th November 2020) in Auckland, New Zealand. Data recording started at 10:00 and stopped at 20:00 (Figure 20 shows the recorded weather data solar irradiation, wind speed and ambient temperature).

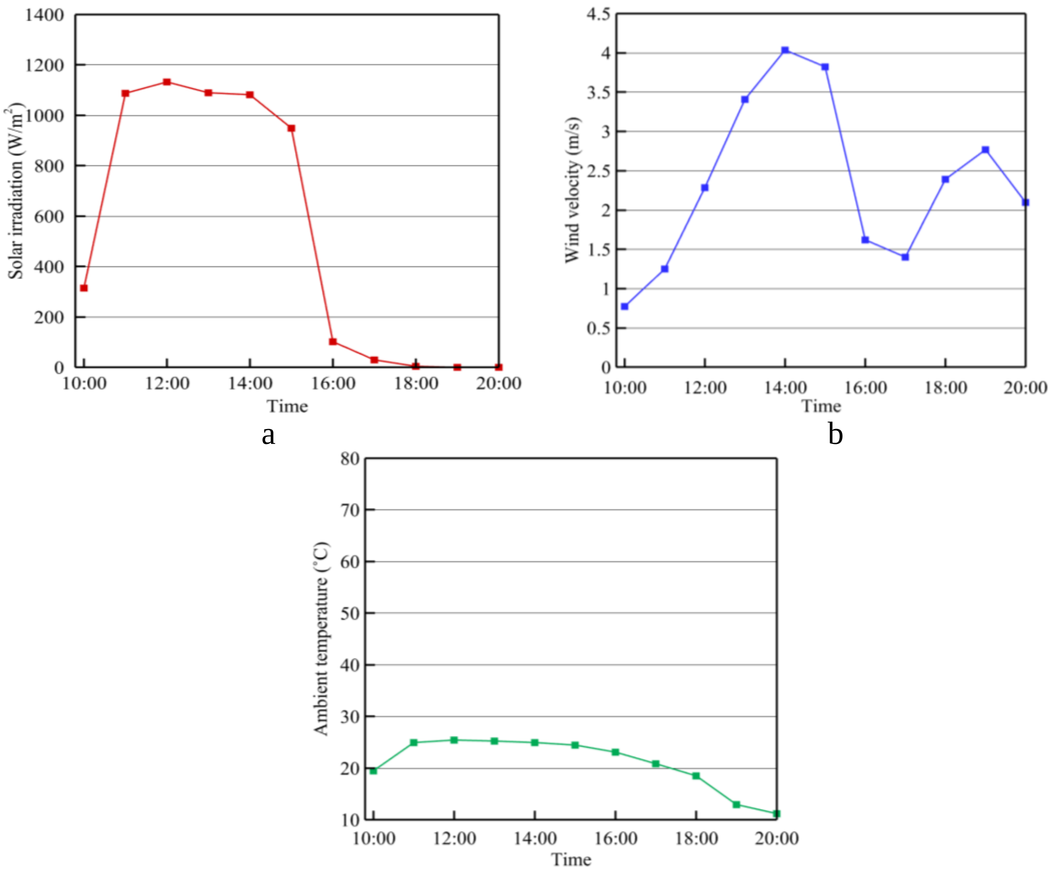

a

b

c

Figure 20: Variation of solar irradiation (a), wind speed (b) and ambient temperature (c).

2.6. Results and discussion

Figure 21 shows the variation of the temperature of the water (T_W) for both the experiment and the selected models. As expected, temperature of the water surface increases as solar irradiation increases and reaches the maximum at approximately 14:00. By carefully examining the water temperature, it can be seen that the models predict lower temperatures than the experimental measurements. This is due to natural convection correlations overestimating the heat transfer coefficient between the water surface and glass cover. Evidently, high heat transfer coefficient correlation leads to more losses from the water surface leading to lower absorber and water layer temperatures. Patently, one can observe that the Adhikari et al. [140] model predicts the lowest water temperature followed by Dunkle [1], Jamil and Akhtar [48] and Rahbar and Esfahani [49]. Moreover, the temperature difference is more pronounced around 14:00 and that is due to the higher solar irradiation leading to high water temperature and high heat losses from water surface.

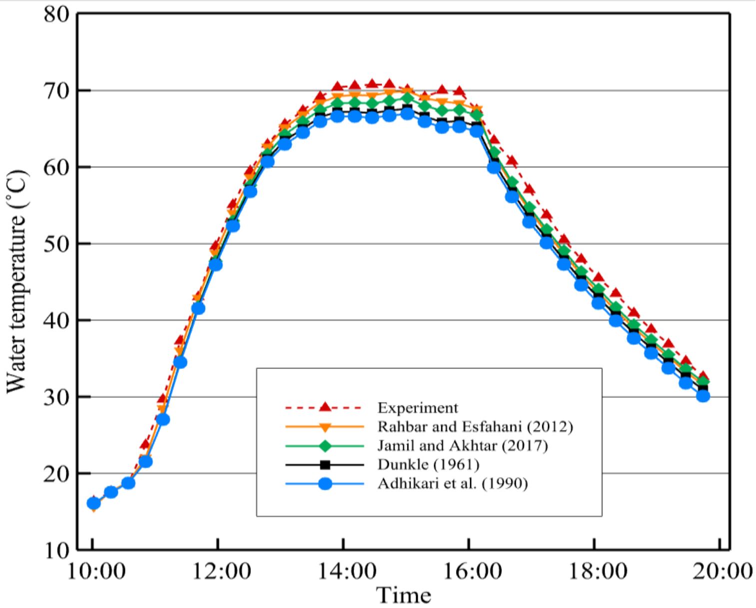

Figure 21: Variation of experimental and simulated temperatures of the water.

It is also seen from Figure 22 that the measured temperature of the cover glass is at variance with the models. However, an opposite trend in the prediction is noticed in contrast to the water, in fact, it can be seen that the models over-predict the temperature of the cover. This trend is ascribed to the heat transfer correlation over-predicting heat losses from water surface to glass cover leading to a predicted higher temperature of the cover compared to experiment. It can also be seen that a fluctuation exists in the measurements at around 16:00, this is believed to be due to the cloud shade resulting in a sudden solar irradiation decrease.

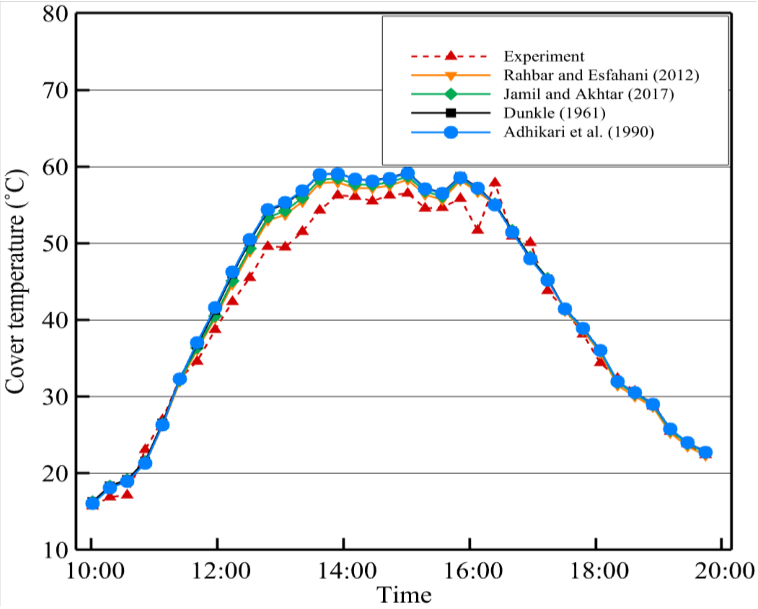

Figure 22: Variation of experimental and simulated temperatures of the cover.

Figure 23 shows the temperature difference between the cover glass and water surface. This clearly shows that the change in the temperature difference between cover and water is more evident compared to previous graphs. This observation is due to both low water and high cover temperature predictions. As expected, the same trend in the difference between the models and experimental measurements is observed in the temperature gradient. These observations are consistent with the findings of previous works such as Shawaqfeh and Esfahani [52] and Adhikari et al. [48].

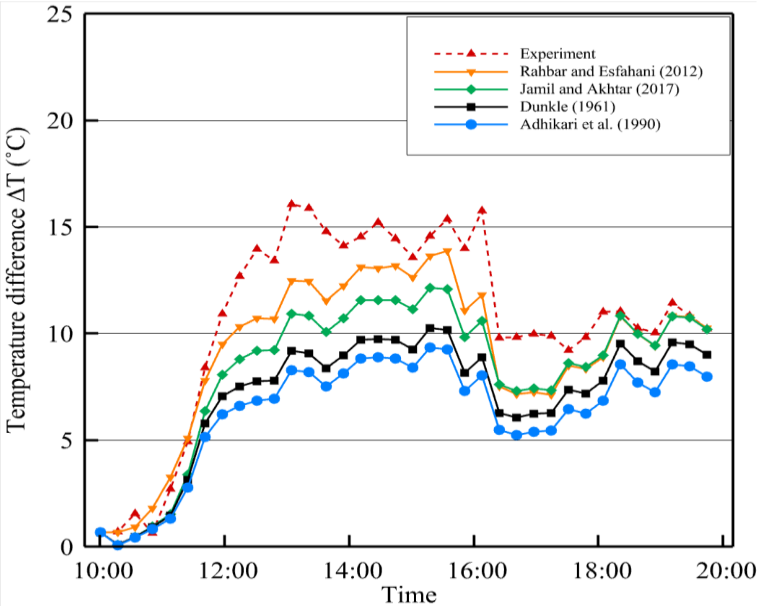

Figure 23: Variation of experimental and simulated temperature difference between glass and water layer.

Figure 24 shows the variation of hourly and cumulative water production of the experimental measurements and simulated results. As expected, the production at the beginning is low because of the small temperature difference between the water and glass cover between 10:00 and 11:00. Even though the predicted temperature differences in simulation are lower than the experiment, that the simulated hourly and cumulative production results are higher than experimental measurements. Knowing that the general understanding is that water production is proportional to the temperature difference between water surface and glass cover, these findings are in conflict with the temperature profile generated by the simulation results. In fact, by looking closely at the water production, all models predict a higher yield than found in the experiment even though the modelled temperature difference is significantly less than experimental measurements. This is believed to be due to the correlations overpredicting the convective heat transfer between water and glass surface, and their shortcomings for consideration of the effect that the geometry (aspect ratio and cover angle) can have on the convection process inside the solar still.

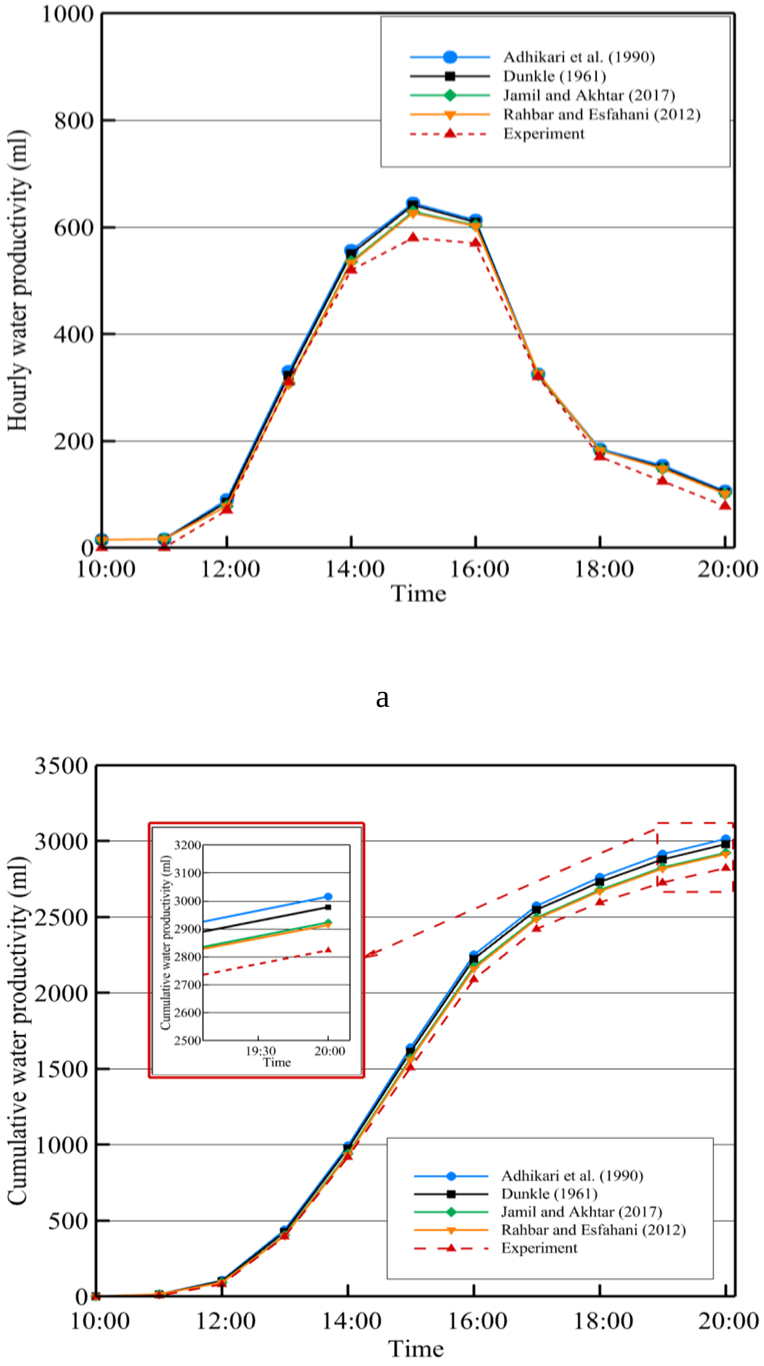

a

b

Figure 24: Variation of experimental and simulated water production.

Having found that the existing correlations underestimate the temperature difference between the water and cover surface while predicting higher yield than the experiment, it is necessary to investigate the correlations independently by using outdoor temperature measurements of water and glass cover. The usage of measured T_W and T_G in the prediction of the $\dot{m}_{ew}$ eliminates all the errors that may be caused by the model assumptions or the use of inaccurate values of solar still parameters [52]. Moreover, this will allow the determination of the magnitude with which the selected heat transfer coefficients overpredict the water yield for the actual measured temperatures. To do this, the original flow chart has been modified and instead of using weather conditions as inputs to the simulation, the measured temperatures of the glass cover and water layer were used. Figure 25 shows the flow chart used in the current investigation.

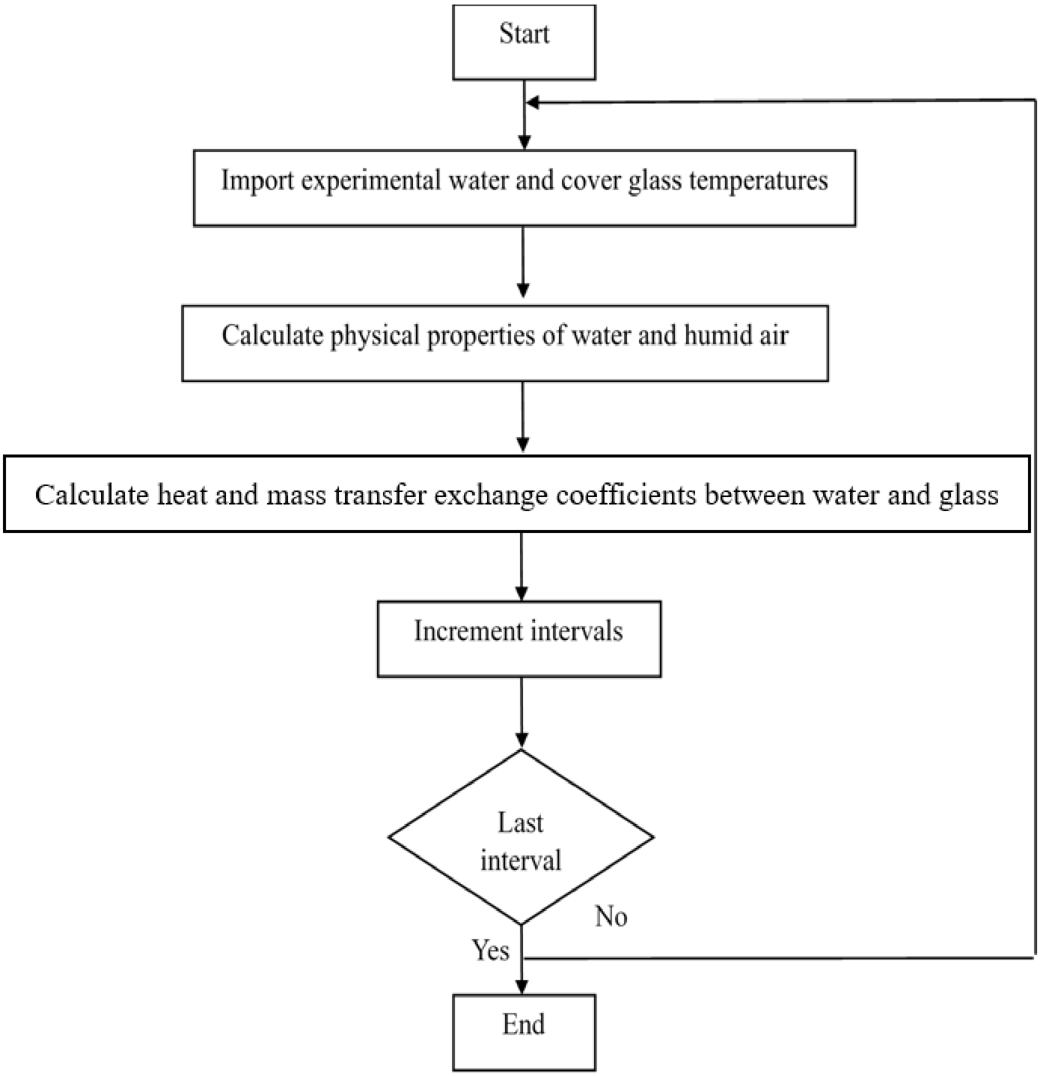

Figure 25: Modified flow chart.

Figure 26 shows the variation of hourly and cumulative water production difference between experimental measurements and selected correlations. It is evident that by using the measurements of the temperature as inputs of the correlations, the predicted results deviate from the actual yield. Moreover, the error in the hourly yield between the correlations and experimental results increases with temperature difference as observed between 14:00 and 16:00 in Figure 26 (a). In addition, the data shown in Figure 26 (b) indicates that the Adhikari et al [53] model overpredicts the daily water production by about 130%, the Dunkle [1] model by 80%, the Jamil and Akhtar [48] model by 38% and the Rahbar and Esfahani [49] model by 30%. This confirms that the previous models do not reflect exactly what occurs in SS solar still geometry under the real temperature profiles of the water and glass cover. It is worth noting that the previous correlations have been developed either based on experimental results or for a limited geometrical configuration.

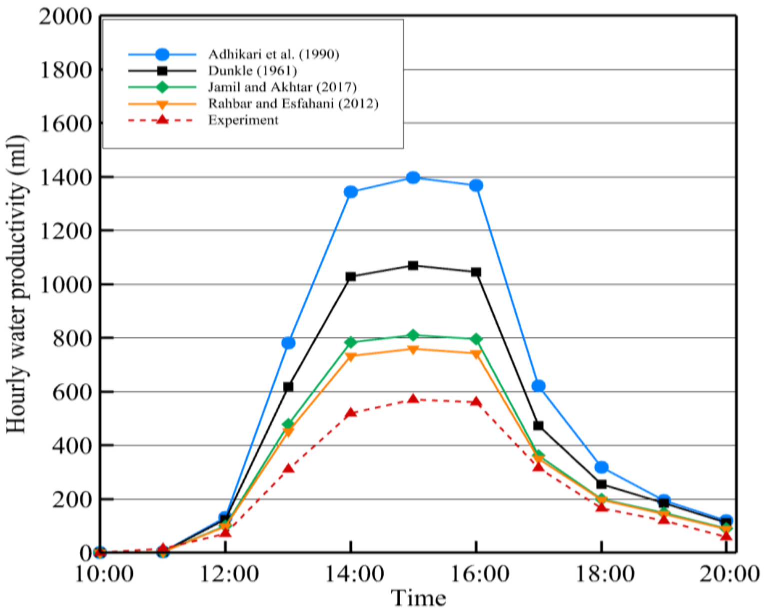

a

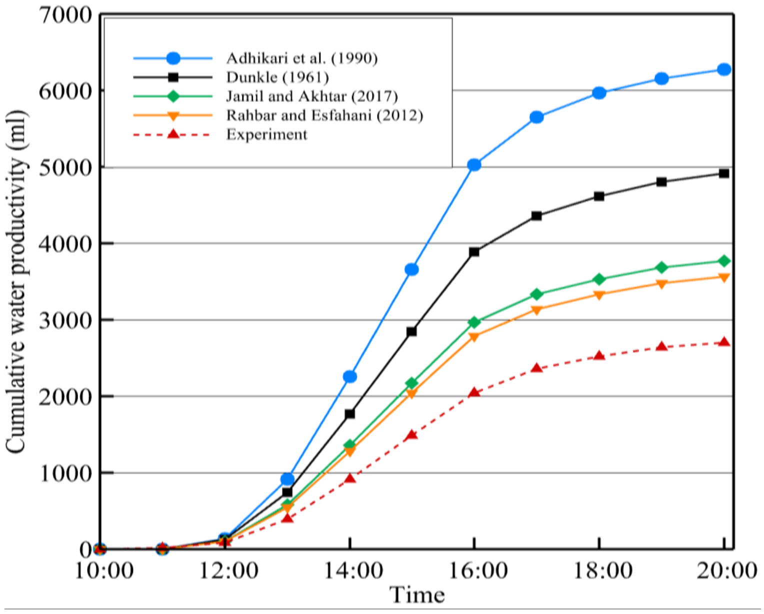

b

Figure 26: Variation of experimental and models water production (modified flow chart).

2.7. Conclusion

In this chapter, a simplified mathematical model for predicting SS solar still performance has been presented. Different internal natural convection correlations developed by previous researchers have been used and investigated in the model. Moreover, an experimental setup was established in order verify the validity of these correlations in the prediction of the temperature profiles of water and glass cover as well as the water production. Results of the experiment and the simulations have shown that the selected correlations overpredicted the heat transfer coefficient by predicting different temperature profiles for the water layer and glass cover. Furthermore, by examining the hourly and cumulative water production, yields predicted by the models using the selected correlations was inconsistent with the temperature difference between water surface and cover. In fact, for a lower predicted temperature difference than found by the experimental measurements, all the models projected higher water production than observed in the experiment.

To investigate independently the magnitude with which the correlations overpredict heat and mass transfer in SS solar stills, measured temperatures of the water layer and glass cover were used as inputs for the models. Following this approach, results have shown that by using experimental temperature measurements the models overpredicted significantly the water production.

Given the above results, one can conclude that there is a need to meticulously study natural convection inside SS solar still geometry and overcome the shortcomings of previously developed correlations.

CHAPTER 3: A GENERALISED RELATIONSHIP FOR MODELLING THE EFFECT OF GEOMETRY ON NATURAL CONVECTIVE HEAT TRANSFER IN A SINGLE SLOPE SOLAR STILL

3.1. Introduction

In Chapter 1, it was noted that extensive research on SS solar stills has been undertaken so it is surprising that there is no clear distinction between the effects that the inclination angle and aspect ratio each have on the convective heat transfer. This is despite the fact that numerous studies have investigated the effect of geometrical parameters on the natural convection inside SS solar stills. However, most of these studies have been performed on specific geometries where the derived correlations are only valid for a limited range of aspect ratios and do not consider the cover angle as a parameter; a fact noted by the authors.

Where an attempt has been made to take into account the aspect ratio or cover angle, it is apparent that the studies tend to treat the effect of cover angle and aspect ratio as a single entity. As such, they do not show the effect of either parameter independently albeit convective heat transfer inside enclosures is known to be dominated by the internal shape of the cavity. Consequently, the previously investigated and existing correlations have limited ability to predict the yield of SS solar stills over a wide range of geometries.

This Chapter therefore aims to separate the effects of aspect ratio and cover angle to quantify the relationship between the natural convection heat transfer, the SS aspect ratio and the cover angle which will help future researchers and practitioners to undertake systematic parametric analyses of the productivity of SS solar stills.

3.2. Model development:

Steady-state simulations of the convective heat transfer inside SS solar stills were performed using ANSYS's commercial computational fluid dynamics (CFD) software, FLUENT 19.2. CFD has proven to be a powerful tool for obtaining reliable results when considering natural convection flow inside enclosures and has been extensively utilised in SS solar still studies due to its low cost compared to performing experiments [49, 51, 72, 141, 142]. Moreover, it allows testing to be easily undertaken over a wide range of parameters.

Determination of natural convection heat transfer coefficients in 3D geometries using CFD is reported to be complex due to the difficulty of attaining convergence and the high computational cost compared to 2D modelling [143]. Therefore, most studies have considered 2D planes when dealing with such problems [7, 24, 49, 78]. This assumption has also been made in this study since SS solar still geometry does not vary along the length of the still.

An experimental investigation of the flow patterns inside a double slope solar still type geometry established that the transition regime occurs at approximatively $Ra = 0.7 \times 10^5$ [144] and an investigation on natural convection in a triangular enclosure (SS solar still geometry) using flow visualisation found that the flow became turbulent at $Ra = 4.7 \times 10^8$ [145]. Therefore, this study has considered the flow to be turbulent since the range of the Rayleigh number was between 3.37×10^6 and 3.03×10^9. As previous research has shown that the Realisable k-ε model generates the best performance of all existing versions of the k-ε model when dealing with problems linked to natural convection in enclosures [143, 146], this study considered the use of the latter model for resolving the turbulence field.

The fluid modelled in the simulation was assumed to be an incompressible ideal gas and to have the physical properties of humid air (see Appendix A). Since the temperature range in solar stills is relatively small, the Boussinesq approximation was used to estimate the density variation of the fluid within the enclosure. The temperature difference between the hot and cold surfaces was assumed to be constant and equal to 15˚C (T_h =45 ˚C and T_c=30 ˚C). Figure 27 shows the imposed boundary conditions for the steady-state study of convective heat transfer inside the single slope geometry. To simplify the study of natural convection within the SS solar still, the water layer and glass cover were assumed to be hot and cold surfaces respectively, each having a uniform temperature. Since the solar still's side walls are insulated, they were assumed to be adiabatic (a similar assumption of boundary conditions has been made in previous studies [7, 24, 49, 78]).

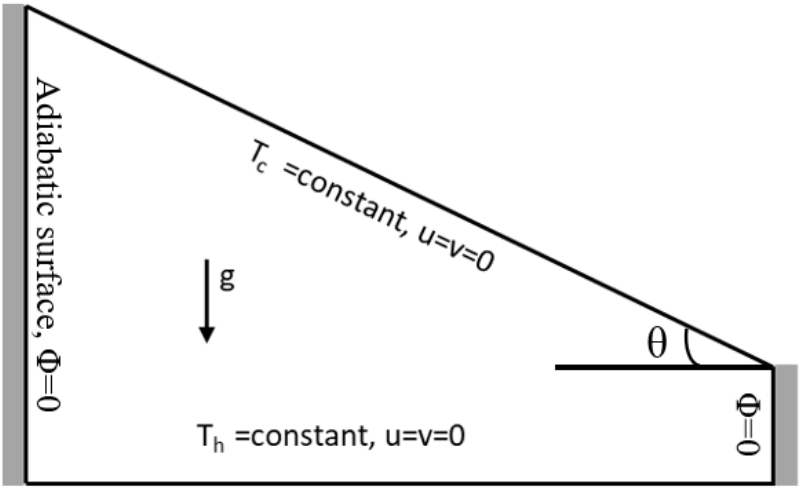

Figure 27: 2D Scheme of SS solar still.

In resolving the discretised form of the continuity equations, the pressure-velocity coupling was handled using a coupled algorithm as it offers a robust and efficient solution for steady state flows. The convection-diffusion terms were solved using a second order upwind approach for higher accuracy (ANSYS Inc, 2015 version, [147]). In solving the continuity equations, the solution was considered to be fully converged when the residuals of all equations were lower than 10^{-5}.

Simulations were performed for a range of aspect ratios (AR: the breadth of the still divided by the mean height) of 1 to 8 and inclination angles (θ) of 0º to 60º, with each parameter varied independently as shown in Figure 28. Although it may seem infeasible to consider SS solar stills with low cover inclination angles $0^o<\theta<10^o$ (due to the possibility of condensed water droplets falling back into the brackish water basin) some studies have considered solar stills with external condensers and lower angles, down to an inclination angle of 0º [148] and so these were included as well.

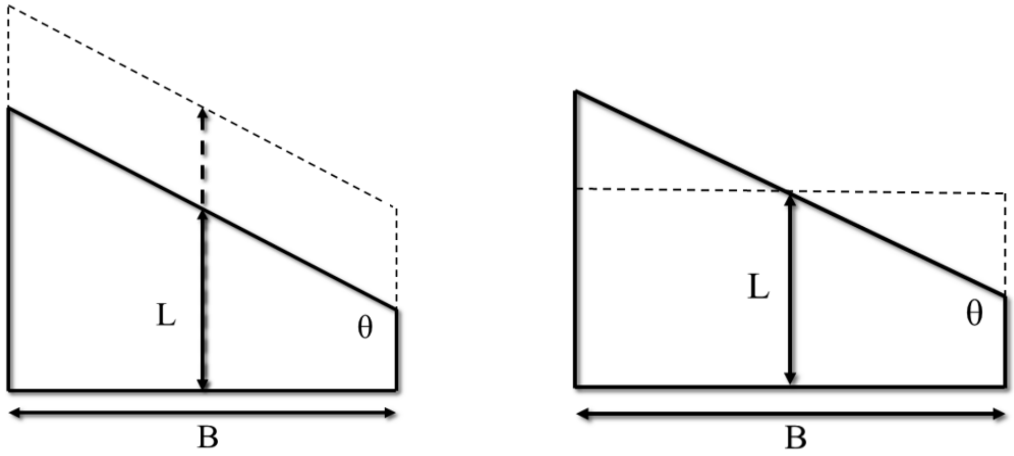

Figure 28: SS solar still geometry variation.

To obtain the optimum mesh configuration for the study, it was crucial to perform a grid sensitivity analysis to optimise the simulation time without decreasing the accuracy level of the CFD results. Heat transfer coefficients from the hot surface calculated from the CFD simulations were compared to determine the best mesh size for the study. Moreover, to control the correct solution of the viscous layer, the distance between the wall and the first node of the grid was varied until the y^+ (Equation 20) value was approximatively equal to 1 [143, 147]. Since the present work deals with variation in SS solar still geometry, three different cover angles 0º, 20º and 50º resulting in aspect ratios of 3.54, 2.57 and 1.93 respectively, were chosen for the analysis. The grid used in this study is structured with dominant quadrilateral elements and a smaller number of triangular elements (because of the angle within the enclosure). Moreover, for more accuracy in near boundary layer calculations, 20 layers of inflation were used with the growth ratio of 1.05. Figure 29 shows the type of mesh used in numerical study.

$$y^{+} = \frac{\rho \delta u_{T}}{\mu} \tag{20}$$

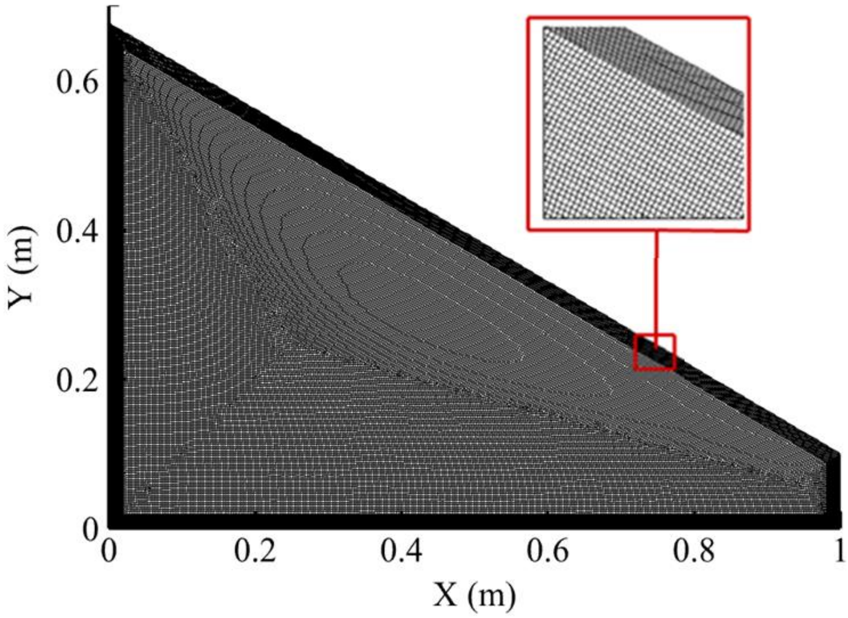

Figure 29: Mesh of SS solar still geometry.

The sensitivity analysis process consisted of selecting different element sizes for the mesh, leading to a different number of nodes. Figure 30 shows the results for the heat transfer coefficient (defined by Equation 21) from the bottom surface for the previously mentioned angles. Comparison of the heat transfer coefficients showed that for all angles there was no significant change by making the element size less than 2 mm. Thus, the problem became independent of the element size, so the same mesh configuration was used for the remainder of the study.

$$h_{cv} = \frac{\varphi_{h}}{T_{h} - T_{c}} \tag{21}$$

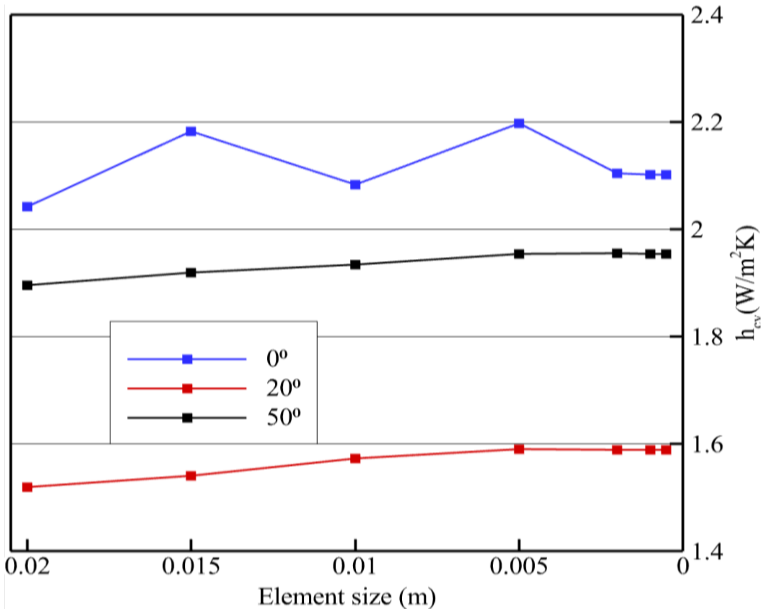

Figure 30: Variation of heat transfer coefficient with the element size at (ΔT=15ºC).

3.3. Experimental setup for flow validation:

3.3.1. Flow visualisation capture

Different techniques have been developed for flow characterisation that are categorised as optical non-intrusive methods and conventional intrusive methods. The intrusive methods such as vane anemometry are used to determine velocity magnitude exactly at the position of the sensor. Alternatively, optical methods for velocity measurements such as Particle Image Velocimetry (PIV) are utilised to acquire flow information by detecting the scattered light of tracer particles. In addition to the advantage of not interfering with the flow, PIV has become prevalent since it offers an accurate qualitative description and precise quantitative information of intricate flows. Moreover, due to the performance of PIV technology, several researchers have tried to develop this technique to suit a wider range of applications. The notable breakthrough for PIV was the use of a double oscillator laser source synchronised with a cross-correlation CCD camera. In fact, PIV technology can be defined as an optical experimental procedure that allows the extraction of flow velocity by capturing the images of moving particles in the fluid of interest [149].

PIV was chosen to capture the flow patterns inside the solar still and validate the selected numerical model. PIV determines the distance travelled by the tracer particles in the selected time frame. Since the velocity of the flow by PIV technique is measured indirectly (quantifying particles' velocity rather than fluid velocity), the interaction between them needs to be considered in order to avoid measurement discrepancies. In addition to the importance of physical properties of the fluid and selected particles, optical properties of the tracer particles are equally important and need to be closely examined [149].

To ease the flow visualisation in the experiment, silicon oil was used instead of humid air [150]. Round Polyamide seeding particles (PSP) from DANTEC were chosen for this as their density matches that of the silicon oil. This prevents the occurrence of measurement errors due to gravitationally induced velocity U_g (Equation 23). The nearly identical density of the particles and silicon oil leads to a high level of confidence in assuming that the particles are neutrally buoyant as demonstrated by equation 24 which describes the time response of the particle (τ_s). Furthermore, according to Markus et al. [149], good light scattering behaviour of tracer particles is dependent of their size, shape and surrounding medium; a detailed description on the relation of the previous parameters and light scattering capability of particles can be found in [149].

$$U_g = d_p^2 \frac{(\rho_p - \rho_{sil})}{18\mu} g \tag{23}$$

$$\tau_s = d_p^2 \frac{(\rho_p - \rho_{sil})}{18\mu} \tag{24}$$

Table 3 summarises the different mechanical properties of the working fluid and tracer particles used in this study and parameters describing their interaction.

Table 3: Fluid and tracer particles properties [151].

Property	Value
Diameter of particles	$50\times 10^{-6}\ m$
Fluid density	$998\ kg/m^3$
Dynamic viscosity of fluid	$0.064\ kg/m.s$
Particle density	$1003\ kg/m^3$
Induced gravitational velocity	$6.4\times 10^{-7}\ m/s$
Time response	$0.065\times 10^{-6}\ s$

Recording the flow using the PIV technique can be categorised into two main classifications: (1) procedures which capture images of illuminated particles' movements with a single frame for different times and (2) procedures which provides information of the particles' distribution for each time in a single image. Knowing that the selection of the procedure depends on the requirements and constraints of the equipment used, it was decided to choose the second procedure with a double frame and single laser exposure (Figure 31). Since the recording of the flow occurs when steady state conditions are achieved, the later procedure would preserve the temporal order of the tracer particle images. Moreover, this choice produces reliable results as the exclusive detection of the correlation peak maximum becomes possible even for small particle image displacements and movements greater than the interrogation window size. This can then be used to accurately determine velocities of the flow from the recorded images by means of a cross-correlation mathematical technique.

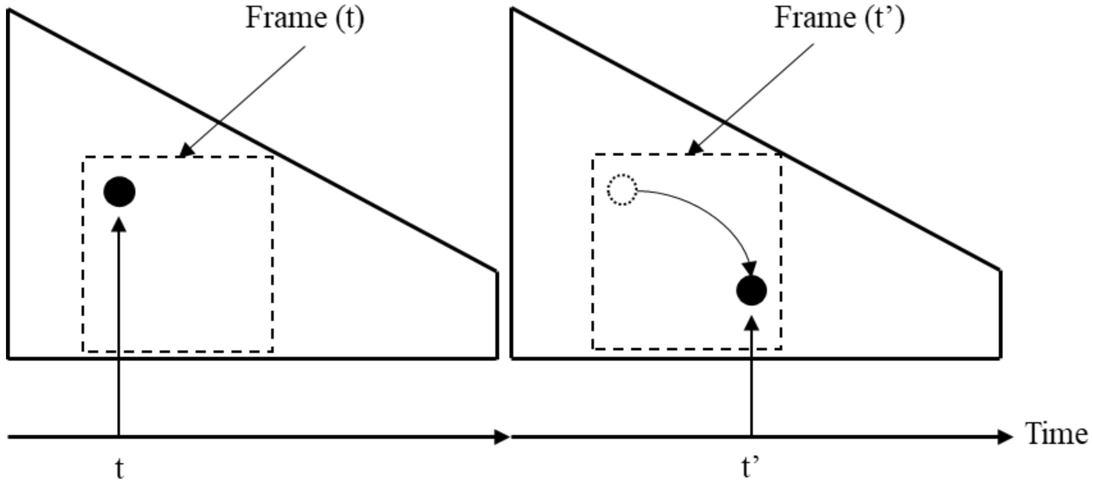

Figure 31: Double frame/Single Exposure.

In this study, the PIV measurement system was composed of a charge-coupled device (CCD) camera and a dual-pulse PIV laser, synchronised by using a MicroPulse725 synchroniser, as shown in Figure 32. The camera recorded pairs of images (2456 x 2048 pixels) at a rate of 16 frames per second and a pulse delay of 40 ms. Due to the enclosure's size being larger than the camera, it was not possible to take images of the whole cross-sectional area instantaneously, thus, the enclosure was divided into 9 sub-areas. In every sub-area, sets of 800 pairs of images were acquired, at steady state conditions, for analysis using the PIVLab package integrated in MATLAB (each pair of images being taken at intervals of Δt=15 ms).

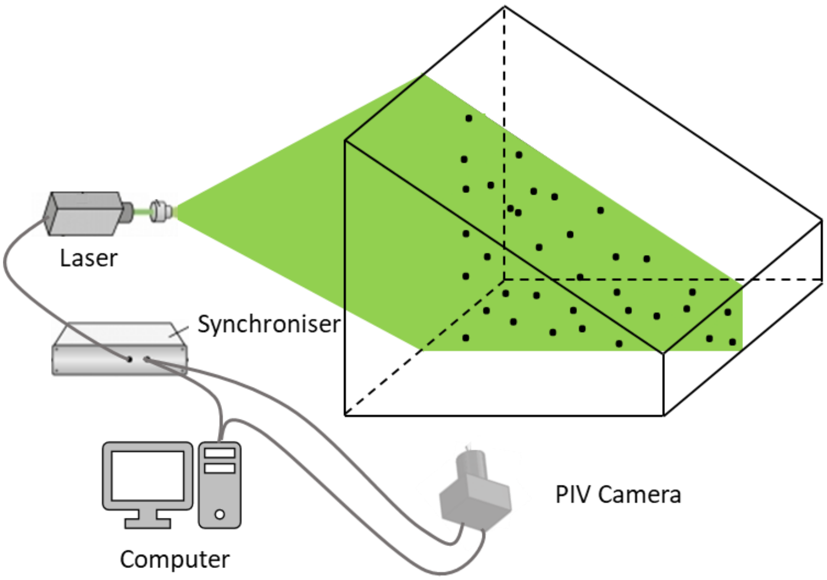

Figure 32: Schematic of the PIV technique.

To perform the PIV measurements and characterise the flow, a SS geometry was fabricated with a 0.4 m × 0.4 m base (B×W), and back and front wall heights of 0.331 m and 0.1m respectively, giving a cover inclination of 30º. The experimental enclosure is shown in Figure 33.

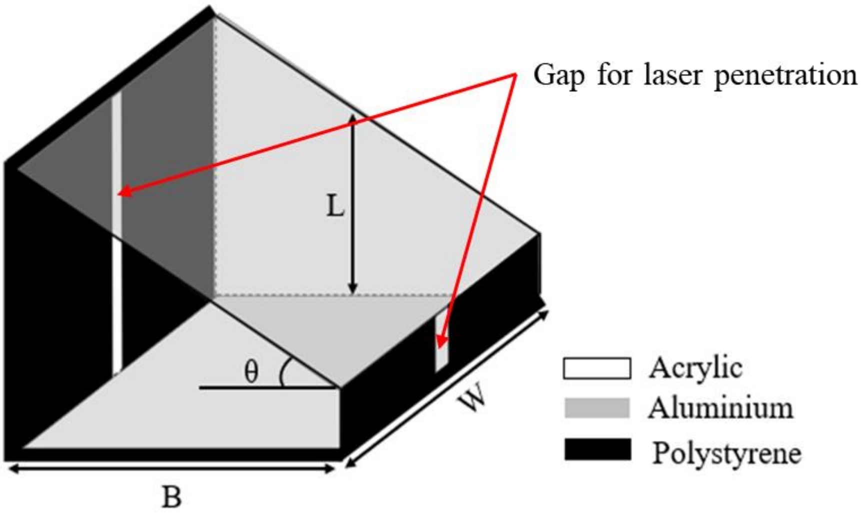

Figure 33: Experimental enclosure.

The previous geometry dimensions and fluid were selected so that the Rayleigh number fell within the same range of Rayleigh numbers likely to be encountered in normal SS solar still operating conditions. The back, front and side walls of the still enclosure were made of transparent acrylic sheets to allow optical access. The front and back walls were insulated by a polystyrene sheet of 4 cm thickness, and a small gap was left to allow the laser sheet penetration in the cavity. However, this meant that the side walls could not be insulated as optical access for the camera was required. The acrylic side walls were fixed to the cover and bottom surfaces with bolts and acrylic adhesive to avoid leakage of the silicon oil.

An adhesive aluminium foil electrical heating element rated at 120W was affixed to the bottom surface of the enclosure to act as the high temperature source in the still, to replicate the absorption of solar radiation. Both the bottom and cover surfaces were made from aluminium sheets of 3 mm thickness to ensure a uniform temperature distribution and were coated with black paint to avoid laser reflection. The heating element was connected to a Variac to control the power supplied, and thus the temperature. A polystyrene sheet of 4 cm thickness was used to avoid heat losses from the heating element through the bottom. Figure 34 shows the fabricated SS enclosure and the PIV setup.

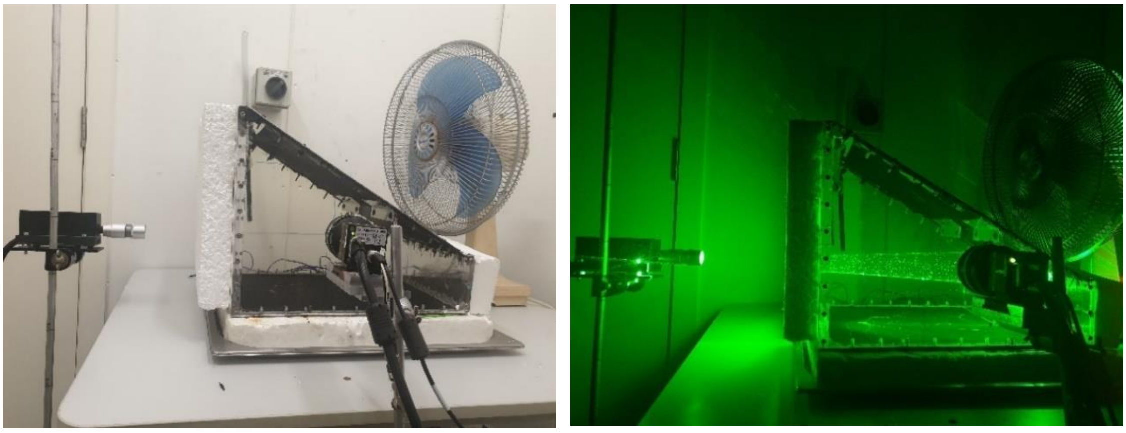

Figure 34: PIV experimental set up.

To maintain a constant temperature difference between the bottom hot surface and the cover, an electric fan was used to cool the cover surface and ensure a consistent temperature condition. Copper-Constantan (T-type) thermocouple wires were used to measure the temperatures of the bottom surface and the top cover. Sixteen equally spaced along X and Y axes thermocouples were used in the experiment; 7 of them located at the bottom (heated) surface, 7 on the cover surface, and 2 in the ambient air. A multi-channel data logger was used to record measurements, and PIV measurements were undertaken once the system reached steady state (typically 15 hours after start-up) as shown in Figure 35. Average temperature of the surfaces (absorber and cover) is shown in Figure 35 as marginal difference between the thermocouples was noticed, confirming the assumption of uniform temperature distribution.

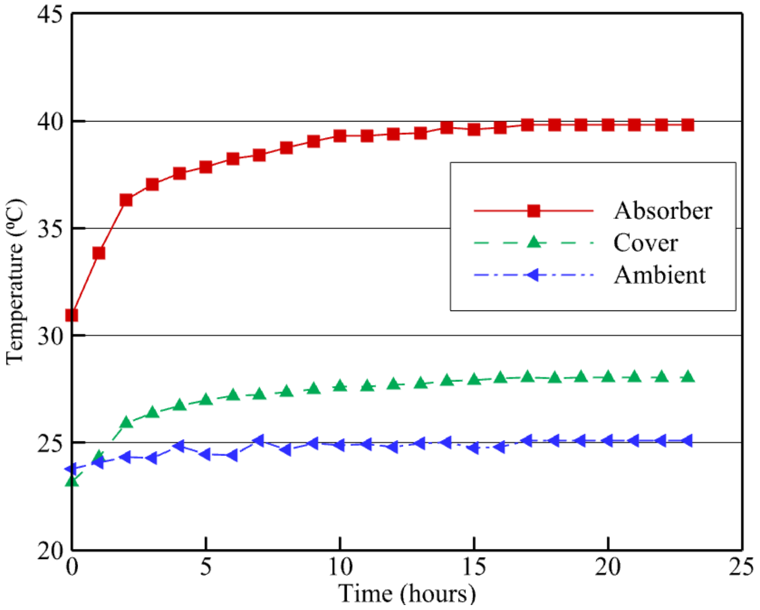

Figure 35: Experimental steady-state temperature measurement.

3.4. Results and discussion

3.4.1. Validation

By applying the experimental boundary conditions in the CFD simulations, analysis of the images obtained during the PIV experiment showed the development of similar flow features when steady-state conditions were reached. Figure 36 shows the velocity contours for both the PIV experiment and the CFD simulation at a plane 0.2 m along the still’s length (i.e. in the z-direction). In both cases there is a plume rising from the hot surface that splits the flow in the enclosure into two cells at approximately the same location (between 0.1 m and 0.2 m), similar flow behaviour was reported by Keshktar et al. [24]. However, it is worth to mention that the plume rises before reaching the left wall, this is because of the cooling due to heat losses creating a descending flow leading to the creation of a second cell near the wall.

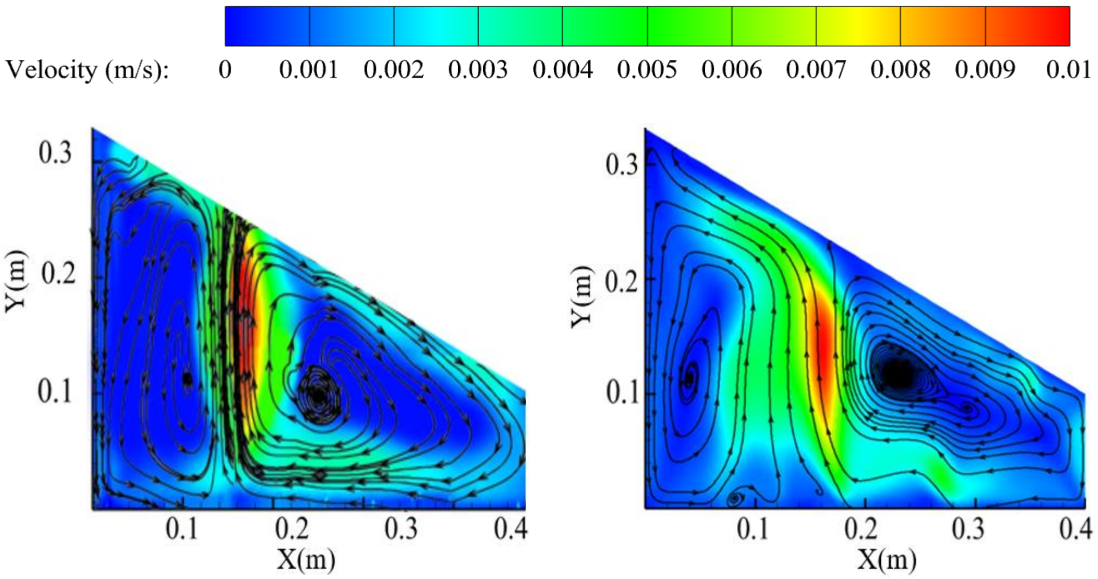

a b

Figure 36: Cross-sectional velocity contour in the middle of the geometry (0.2m, AR=2.6, θ=30º, Ra=1.38×108), a: Experiment (PIV), b: CFD

As further validation, Figure 37 shows a comparison of the velocity profiles across both the CFD simulation and the PIV experiment at the mid-height of the enclosure (y = 0.16 m). Near the walls, both the simulation and measurements show that the velocity is very low compared to the velocity of the rising plume. The predicted maximum velocity using the numerical model is $9.3 \times 10^{-3}\ m/s$, 4% lower than the measured peak velocity of $9.7 \times 10^{-3}\ m/s$. Although the predicted velocities agree, Figure 37 shows that the simulated plume is slightly wider; this is due to the limited number of particles in the experimental study. However, in general, the results from the simulations agree very well with the PIV measurements, which give confidence in the use of the CFD model.

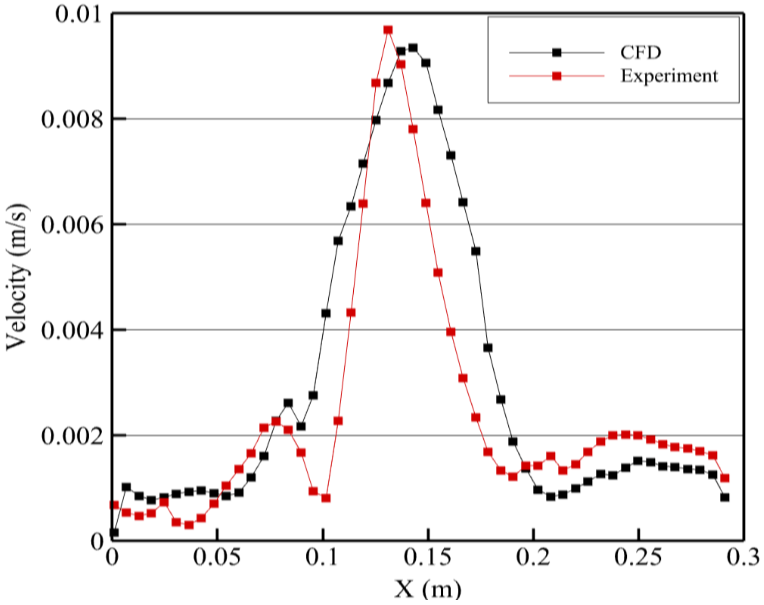

Figure 37: Velocity profile at Y=0.16 m.

3.5. Effect of SS solar still geometric parameters on convective heat transfer

3.5.1. Effect of aspect ratio

Having experimentally validated the use of CFD in predicting the flow in a solar still type enclosure, the effect of variations in the geometry on the behaviour of an ideal still were examined. Figure 38 shows the effect of the aspect ratio on the average heat transfer coefficient on the bottom surface for different cover angles (θ = 0º, 10º, 20º,30º and 40º). The results show that, for a given cover angle, high heat transfer coefficients occur at lower aspect ratios, however they gradually decrease to some minimum value before increasing again, this can be attributed to the local velocity in the enclosure. As shown in Figure 39, for θ = 30º, the local velocity through the characteristic length (enclosure height) varies with the aspect ratio. The increase in velocity with the decrease in aspect ratio is due to the increased distance between the bottom and cover surface changing the balance between the buoyancy and viscous forces.

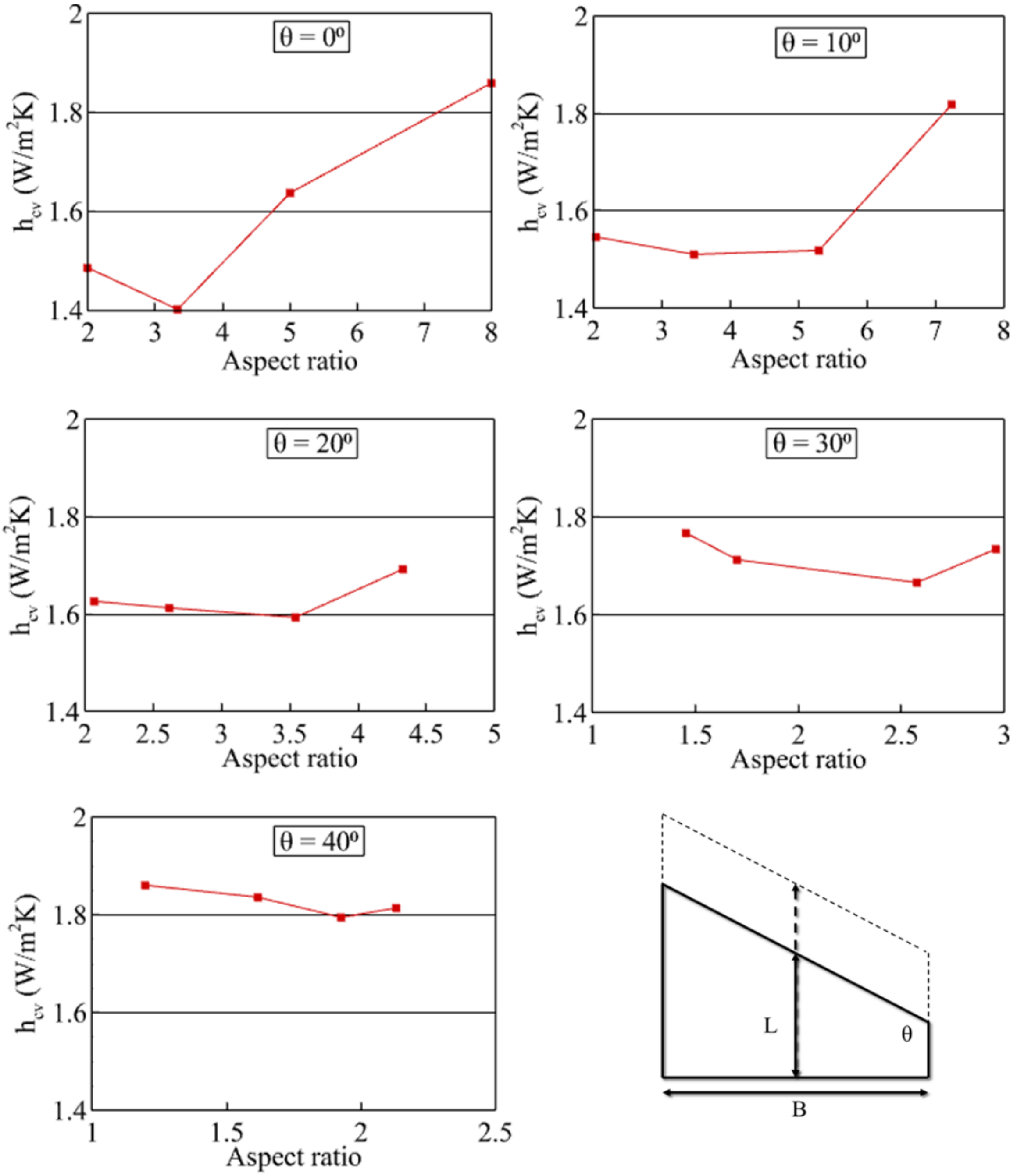

Figure 38: Effect of aspect ratio on absorber heat transfer coefficient.

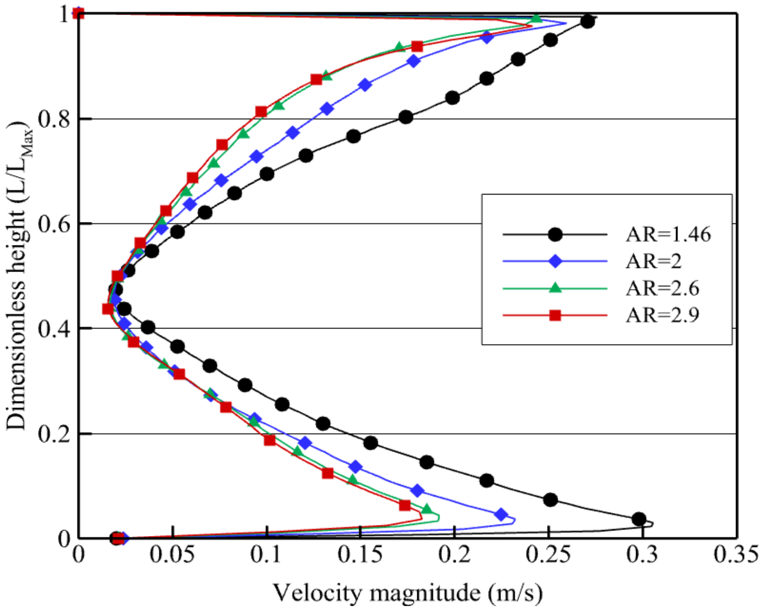

Figure 39: Local velocity at θ=30˚ for different aspect ratios.

To explain this, it is worth noting that at high aspect ratios the cover surface is situated closer to the bottom surface. As shown in Figure 40, this leads to the formation of a cell, with a relatively high velocity, forming near the right side-wall. This relatively high velocity flow results in an increased local heat transfer coefficient from the bottom hot surface as seen in Figure 41. For a low aspect ratio (AR = 2.6), the heat transfer coefficient reaches its peak close to the right wall, where cold fluid impinges on the bottom surface. However, at a higher aspect ratio (AR = 2.9), the heat transfer coefficient reaches its peak just before the right wall (x = 0.9m) because of the formation of a high velocity cell that aids the transfer process.

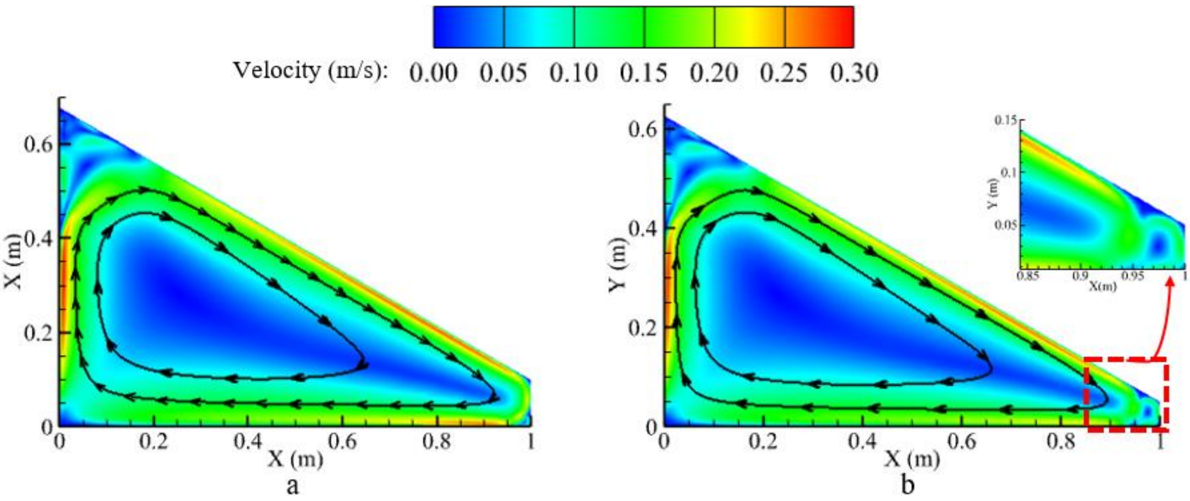

Figure 40: Velocity contours at θ=30º, a: AR = 2.6, b: AR = 2.9.

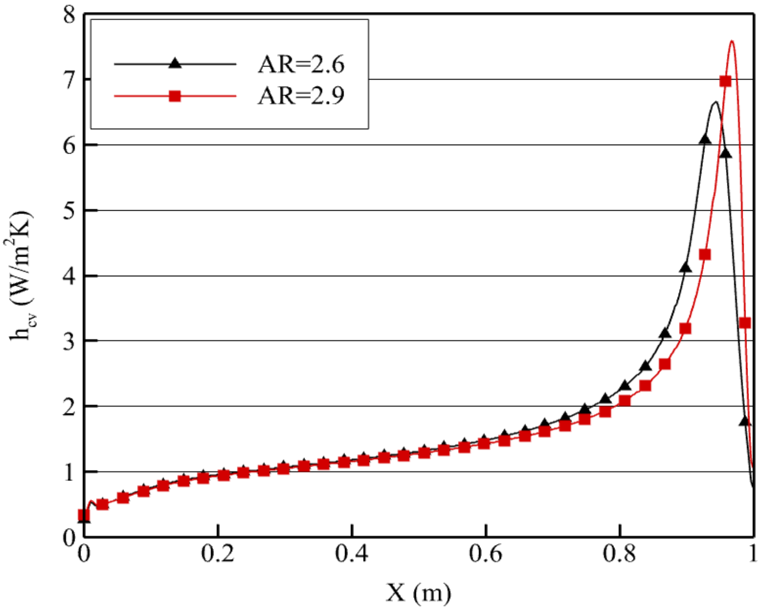

Figure 41: Local convective heat transfer coefficient at θ=30º, AR = 2.6, AR = 2.9.

3.5.2. Effect of cover angle

Having seen that aspect ratio plays a role in determining the heat transfer in a SS solar still, it is important to investigate the effect that the cover slope plays on this too. Figure 42 shows the effect of the cover angle on the heat transfer coefficient from the bottom surface for five different aspect ratios (5.52, 3.55, 2.58, 1.93, 1.44). The results show that for a given aspect ratio, the heat transfer coefficient from the hot surface increases with an increase in the cover angle, with the exception of very wide and shallow stills (AR = 5.52).

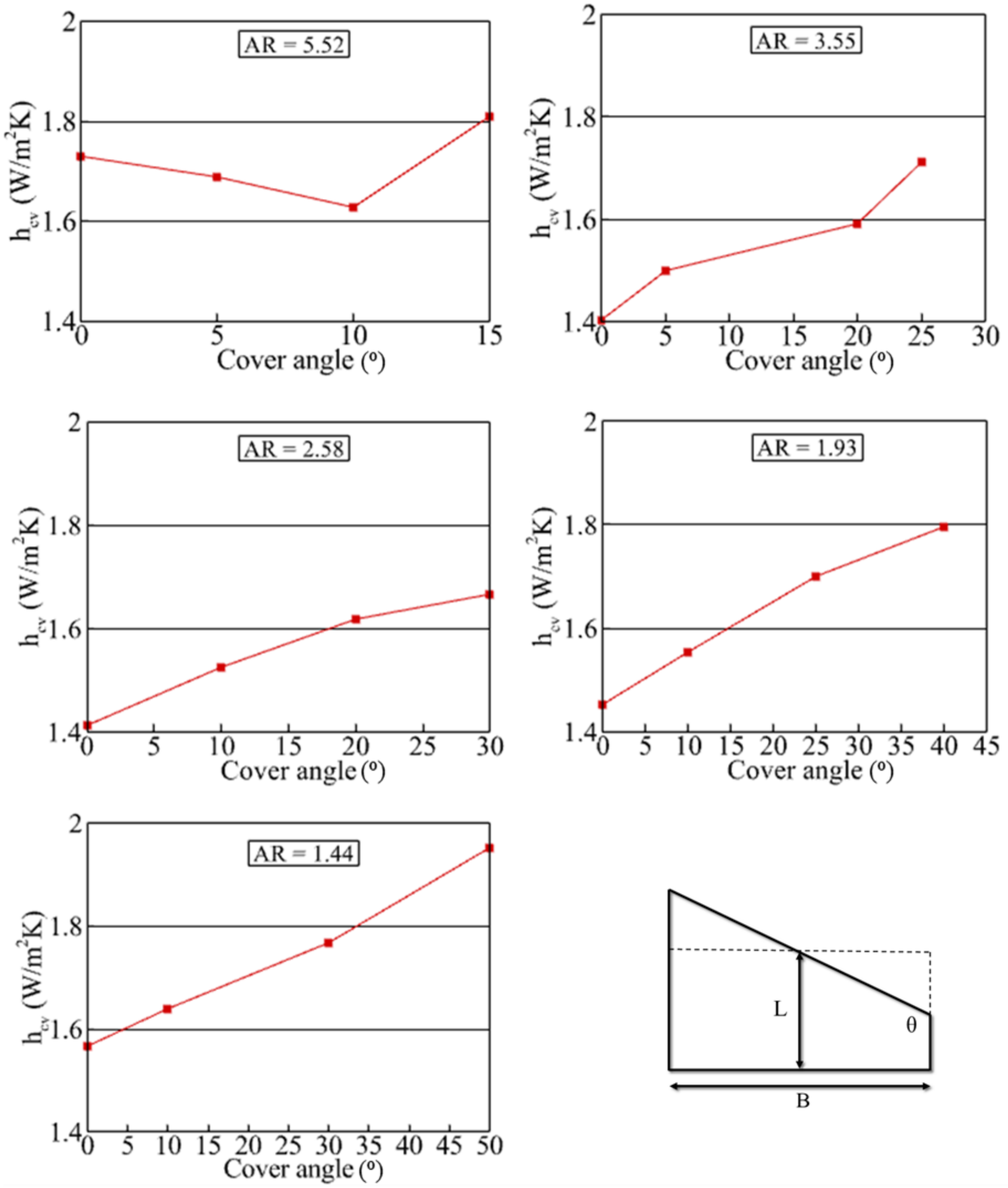

Figure 42: Effect of cover angle on absorber heat transfer coefficient.

To explain the variation to the heat transfer coefficient at AR = 5.52 (Figure 42, a), it is necessary to examine Figure 43 which shows velocity streamlines at AR = 5.52 for two different angles (θ = 0º, b: θ = 10º). From this it is apparent that, at lower angles (θ = 0º), there are multiple convection cells (Bénard cells), whereas at θ = 10º natural convection occurs with only one cell. The presence of multiple cells allows more heat to be carried away from the bottom surface. Further illustrating this point, Figure 44 shows the effect of the cover angle on the local heat transfer coefficient from the bottom hot surface. At a low aspect angle (θ = 10º), the heat transfer coefficient reaches a peak twice (x = 0.05 m and x = 0.8 m) because of the formation of three cells. However, at a higher cover angle (θ = 10º) the heat transfer coefficient reaches its peak at the right wall where cold fluid begins transporting heat from the bottom wall, in a single cell pattern. Even though the peak for θ = 10º is higher than the two peaks for θ = 0º, the overall heat transfer coefficient is higher in the latter case with 17.9%. This is because the multi-cellular flow, is more efficient at transferring heat away from the hot surface.

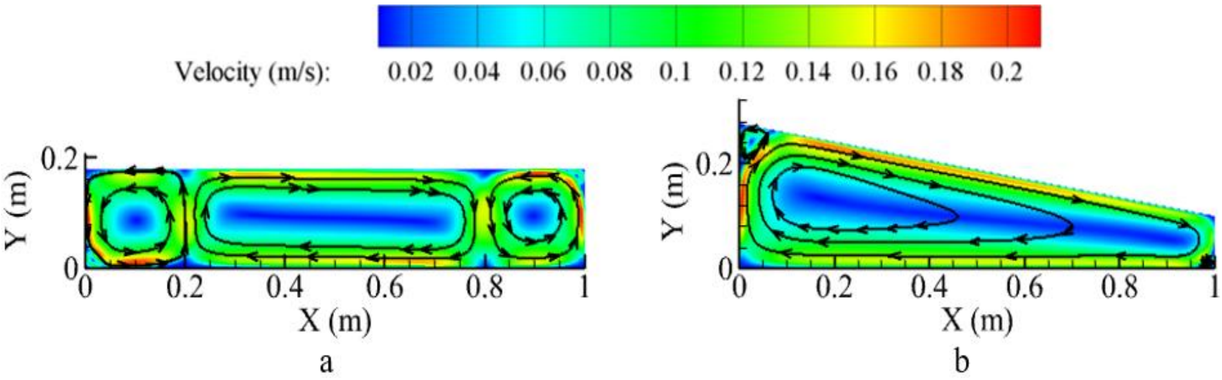

Figure 43: Velocity contours at AR = 5.3; a: θ=0º, b: θ=10º.

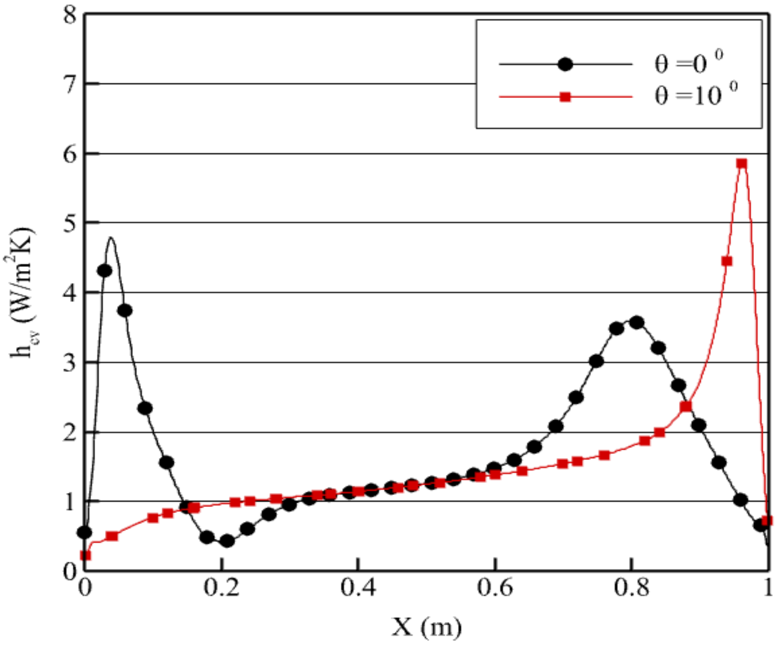

Figure 44: Convective heat transfer coefficient at AR = 5.3; a: θ=0º, b: θ=10º.

Despite the decrease in heat transfer coefficient with an increase of cover angle at AR=5.52, a significant increase in the heat transfer coefficient with the increase of angle is noticed for all other aspect ratios. To explain this, Figure 45 shows the velocity contours for a still with an aspect ratio of 3.55. It can be seen that at θ = 30º a large convection cell exists in the top corner, however this starts decreasing in size as the cover angle decreases. This leads to a reduction in the efficiency of the heat transfer from the bottom wall (a reduced heat transfer coefficient) as shown in Figure 46.

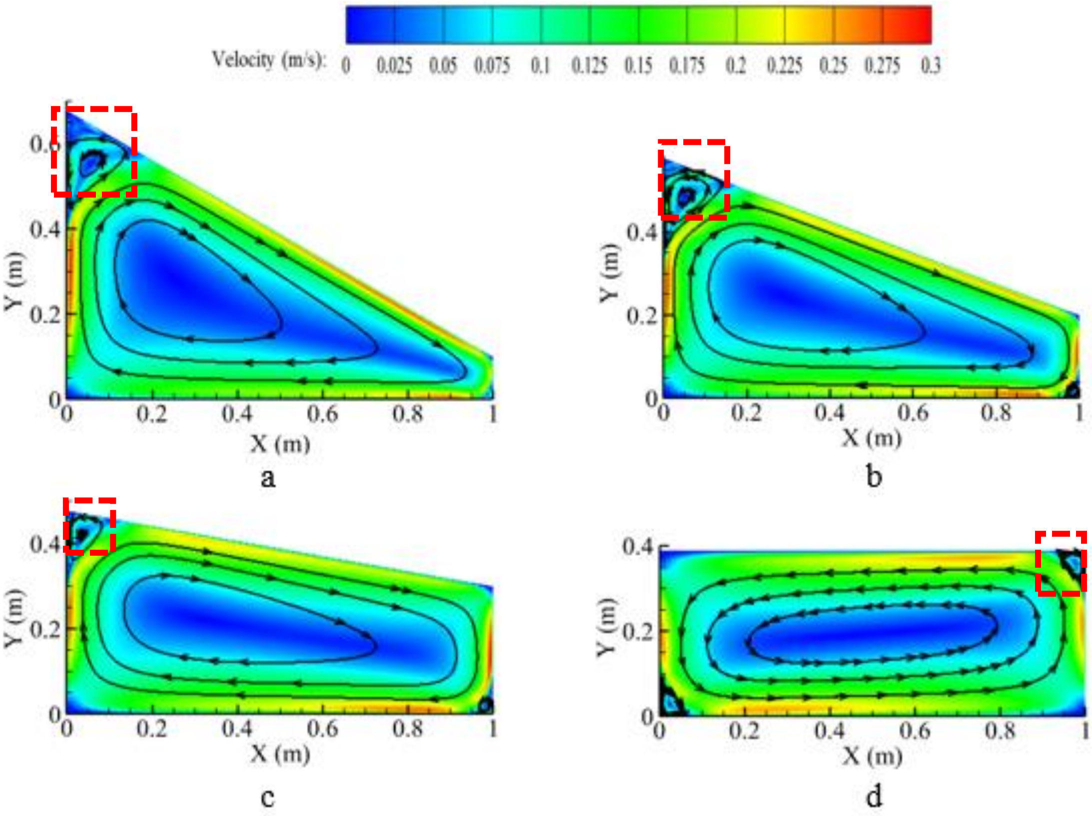

Figure 45: Velocity contours at AR = 3.55; a: θ=30º, b: θ=20º, c: θ=10º, d: θ=0º.

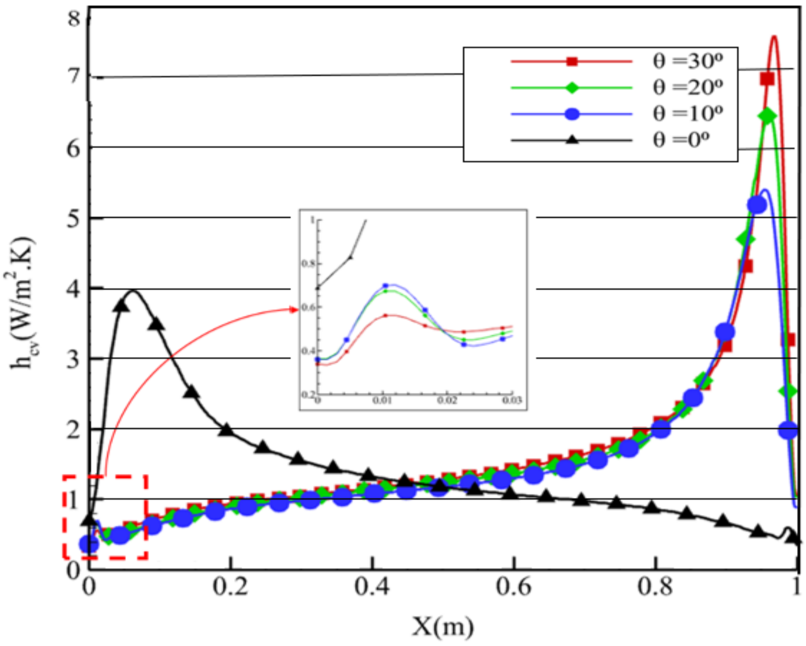

Figure 46: Local heat transfer coefficient for different angles at AR=3.55.

3.6. Correlating geometry to heat and mass transfer

The results have shown that aspect ratio and the cover surface angle have a significant effect on the convective heat transfer coefficient in a solar still, and that this is related to the nature of the flow field. However, in order to facilitate improved parametric modelling of SS solar stills, a relationship to describe the heat transfer would be invaluable. By generalising the results from the CFD modelling and using non-linear regression technique the relationship between the Nusselt number and the previous parameters can be represented by a dimensionless multi-parameter correlation, as shown in equation 25 (where $3.37\times10^{6} < Ra < 3.03\times10^{9}$; $0^{o} < \theta < 60$; $1<AR<8$).

$$Nu = Ra^{0.187}\,(AR)^{-0.488}\cos(\theta)^{-0.416} \qquad (25)$$

Figure 47 shows that within the range of Rayleigh numbers, there is a good relationship between the CFD results and the predicted values from the proposed correlation. This suggests that equation 25 is well suited for use in predicting the heat transfer coefficient over a wide range of geometries.

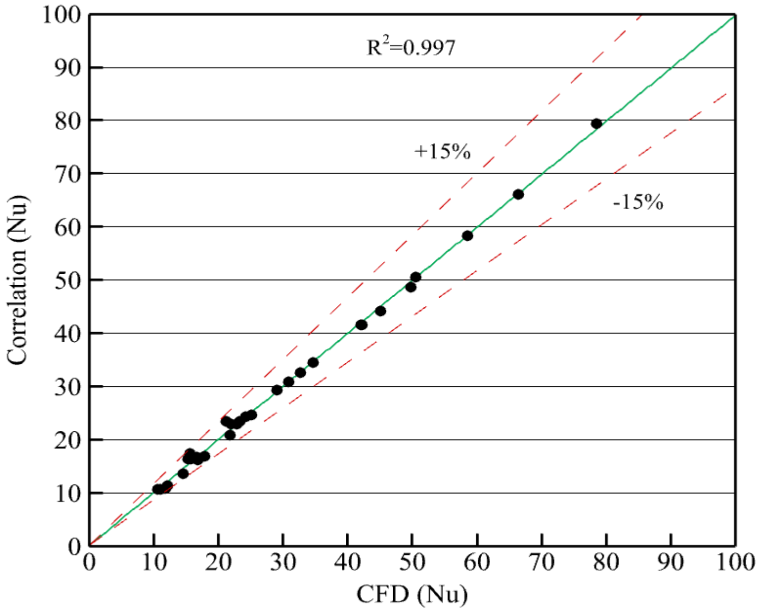

Figure 47: Correlated data of the study.

However, equation 25 only accounts for the heat transfer process of the SS solar still. For a fixed geometry, Boelter and Sharpley [152] noted that for heat transfer alone, the Rayleigh number varies directly with the temperature difference $(T_h - T_c)$. However, in the case of solar stills, mass transfer occurs simultaneously with heat transfer, therefore, the Rayleigh number varies directly with $\Delta T' = (\frac{M_c T_c}{M_h T_h} - 1)$. For this reason, the authors suggest modifying equation 25 to consider the mass transfer process by using a modified Rayleigh number. Thus, the proposed correlation can be represented by equation 26 using the modified form of the Rayleigh number shown in equation 27.

$$Nu' = Ra'^{0.187}\,(AR)^{-0.488}\cos(\theta)^{-0.416} \tag{26}$$

Where:

$$Ra' = \frac{\rho_{hair}^{2}\,g\,\beta\,\Delta T'\,Cp_{hair}\,L^{3}}{\lambda_{hair}\mu_{hair}} \tag{27}$$

A comparison between Nusselt values of previously examined correlations and the developed model is shown Figure 48. It can be observed from both graphs a and b that the previously examined correlation predicts higher Nusselt number for both cases different aspect ratios (constant cover angle 30˚) and cover angles (constant aspect ratio 2.57) compared to the developed model. Moreover, graph (a) shows that, for all correlations, the Nusselt number decreases with the increase in aspect ratio; this is due to the decrease of flow velocity inside the cavity as result of the decrease in height between the bottom and top surface. On the other hand, it can be seen from graph (b) that all selected models are independent of the cover angle, therefore, as the angle increases, no effect on Nusselt number (heat transfer) is observed for a constant aspect ratio (constant Rayleigh number). Further, an increase in Nusselt number for the developed model is obtained as the cover angle increases, and it is also observed that greater angles have higher effect compared to lower angles. This demonstrates that the latter model provides comprehensive behaviour of complex heat transfer inside the solar still cavity.

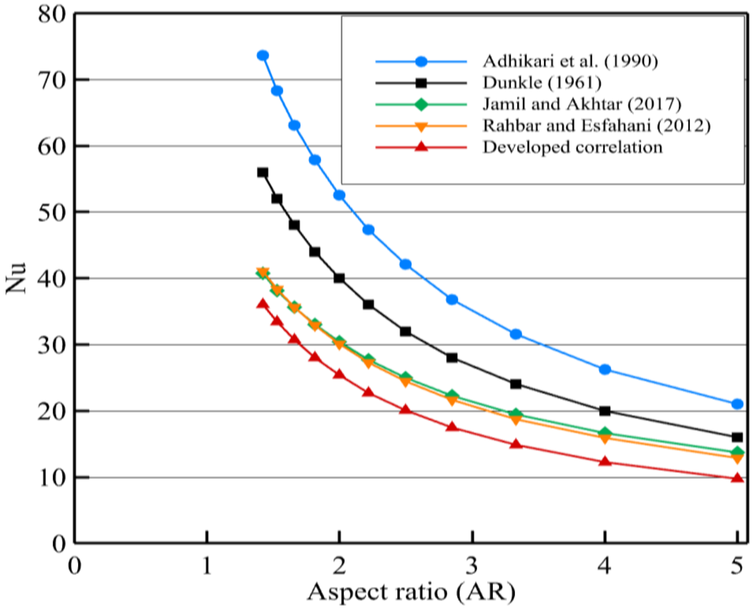

a

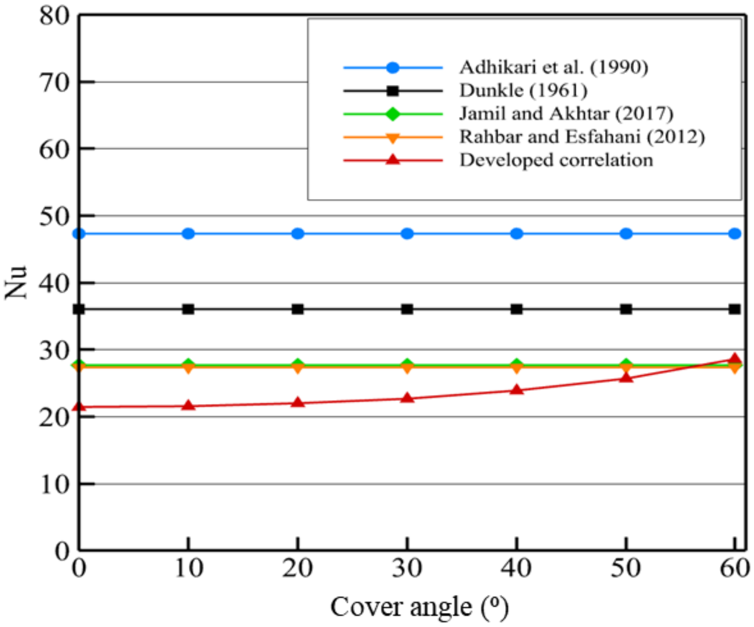

b

Figure 48: Nusselt number variation for different aspect ratios (a) and cover angles (b).

For further verification of the new developed correlation with an outdoor experiment, it was decided to examine the validity of this correlation by predicting performance of a SS solar still reported by Manoj Kumar et al., Attia et al., Rabhi et al. and Shawaqfeh and Farid [52, 153-155]. Taking into account that various materials can be used in solar stills and the lack of data used during the experimental studies, the common practice to evaluate the correlation accuracy is to use the temperature difference between the water surface and the glass cover temperature and calculate the yield using equation 18 [52, 79]. Even though the selected studies (Table 4) are of different SS solar stills with differing cover angles (θ) and aspect ratios (AR) ranging from 9˚ to 35˚ and 1.8 to 3.7, respectively, Figure 49 and Figure 50 show close agreement between measured hourly and cumulative water yield and predicted yield attained by using the new developed correlation model. With less than 5% of error in the cumulative yield between the new correlation and experimental measurements, it is proven that the correlation provides an inclusive prediction of complex heat transfer behaviour inside the cavity. Moreover, this constitutes solid evidence that the developed correlation is more accurate in the prediction of SS solar still performance than the existing correlations.

Table 4: Validation of the correlation with different studies.

Study	Cover angle	Aspect ratio
Rabhi et al. [153]	35˚	1.1
Manoj Kumar et al. [154]	11˚	1.9
Attia et al. [155]	9˚	2.6
Shawaqfeh and Farid [52]	20˚	3

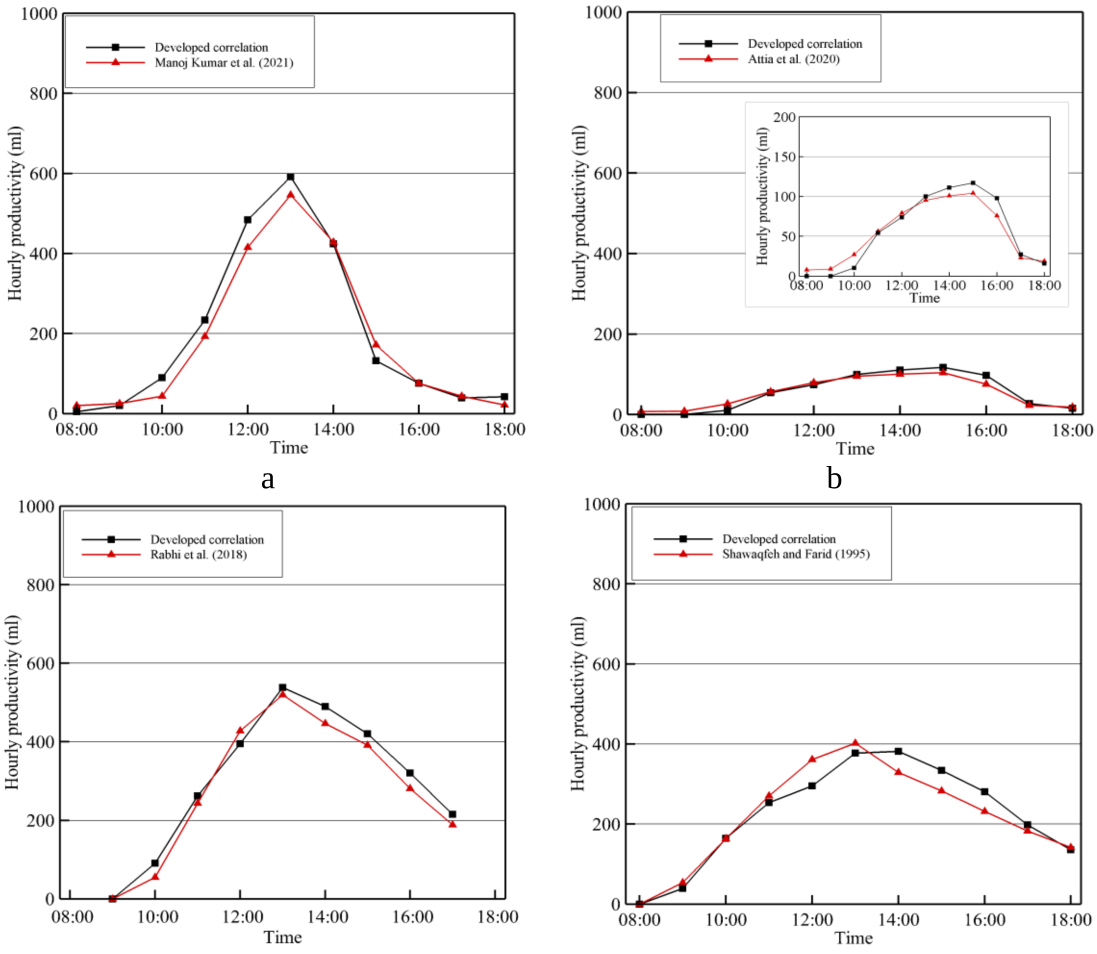

a b

c d

Figure 49: Predicted hourly yield against measured data, a: Manoj Kumar et al. [154], b: Attia et al. [155], c: Rabhi et al. [153], d: Shawaqfeh and Farid [52].

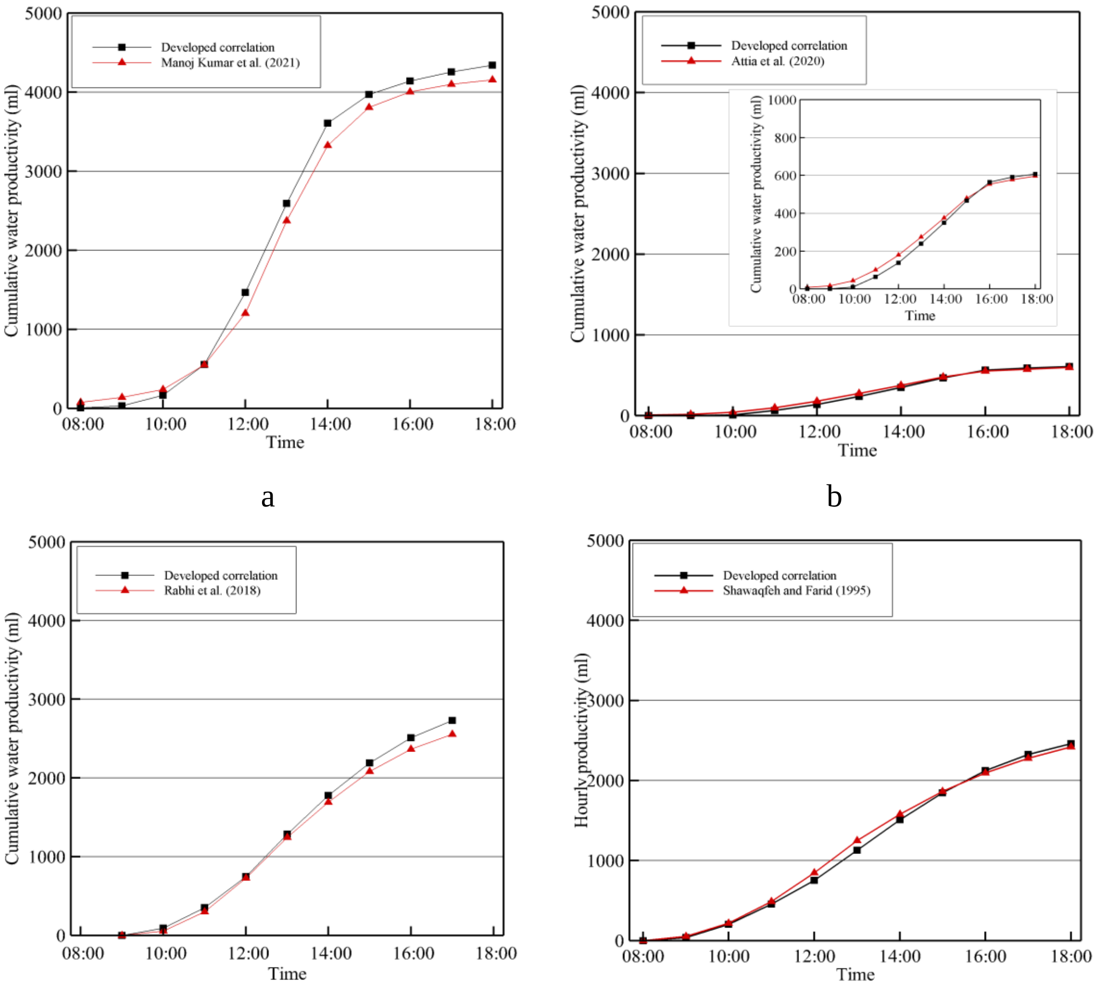

a b

c d

Figure 50: Predicted cumulative yield against measured data, a: Manoj Kumar et al. [154], b: Attia et al. [155], c: Rabhi et al. [153], d: Shawaqfeh and Farid [52].

3.7. Conclusion

An investigation of the convective heat transfer inside a SS solar still using CFD validated with PIV was conducted. Using this method, the heat transfer coefficient from the hot surface was determined in a single slope enclosure with aspect ratios and cover angles in the range 1 – 8 and 0º - 60º, respectively. Although previous studies developed correlations to predict natural convection based on the enclosure aspect ratio, this work showed that the heat transfer in such geometries also depends on the cover angle.

This work showed that the heat transfer coefficient from the bottom hot surface was closely linked to both the aspect ratio and the cover angle in considered separately. When the aspect ratio was high, the heat transfer coefficient was high due to the proximity of the absorber and cover surface and the creation of cells, starting from the right wall side. Moreover, for mono-cellular flow, when the aspect ratio decreased, the heat transfer coefficient increased due to the increase in velocity. Regarding the effect of cover angle on the heat transfer coefficient, it was established that at lower cover angles, when multi-vortex flow was generated, the heat transfer increased. However, for mono-cellular flow cases, the increase in velocity associated with increased angles also led to an increase in the heat transfer coefficient.

A subsequent linear regression analysis provided a correlation of the Nusselt number that depends on the Rayleigh number, the aspect ratio and the cover angle. The developed relation describes more accurately the effect of the geometrical parameters on natural convection inside the enclosure compared to the equations suggested in former studies. Moreover, in conjunction with heat and mass transfer analogy, one can easily predict the performance of solar stills in terms of distilled water production. The correlation was then used to verify its consistency with other published work in the literature. To do this verification, different experimental results with various aspect ratios and cover angles were selected from the literature and these results showed that the developed correlation predicted the experimental yields very accurately which means the developed correlation can be used as a prediction tool with confidence.

In summary, it was demonstrated that natural convection is directly affected by the variation in the geometry of SS solar still. Moreover, it was shown that the aspect ratio and cover angle alter the flow inside the enclosure and therefore the heat transfer coefficient between the water and the glass cover. This has led to the development of a correlation that describes accurately the natural convection in SS solar stills.

Given the nature of multicellular flow inside the enclosure which leads to an increase in convective heat transfer coefficient, it is important to find out ways of creating multicellular flow pattern in geometries where monocellular flow is dominant. Therefore, Chapter 4 is a study of the effects of including a baffle on the cover in order to force the flow to become multicellular, hence enhancing natural convection within the enclosure.

CHAPTER 4: INVESTIGATING THE INFLUENCE OF MOUNTED BAFFLE LENGTH AND POSITION ON THE NATURAL CONVECTION INSIDE SINGLE SLOPE SOLAR STILL GEOMETRY

4.1. Introduction

Based on the findings of the previous chapter, it was shown that the flow patterns inside SS solar still geometry significantly affect the convective heat transfer coefficient inside the enclosure. Moreover, it was found that, for a given temperature difference, a multicellular flow results in more heat being transferred from the water surface, that is to say it has a higher heat transfer coefficient. Knowing that the dominant flow encountered in SS solar still geometries is monocellular, there are possible ways to alter the flow inside the enclosure. Hence, the use of passive baffles to force the convection from a monocellular to a multicellular flow presents an opportunity to increase the heat transfer coefficient inside the enclosure, and ultimately the yield of a SS solar still.

For the use of baffles to alter the air flow between water surface and glass cover inside SS solar still geometry, Moukalled and Darwish [156] studied natural convection in trapezoidal enclosures with baffle mounted on the top inclined surfaces. A geometry with a cover angle of 15° was considered. Two different cases of boundary conditions were investigated: summer-like and winter-like conditions. During the winter season (where the boundary conditions are similar to SS solar stills), it was found that, for a given baffle length, heat transfer increases with the increasing distance from the lower side wall. Varol et al. [157] numerically investigated the effect of a thin fin on the natural convection inside triangular enclosure. Results showed that including fins on the bottom wall modifies the rotational direction of vortices. The Nusselt number was found to increase with the increase of Rayleigh number but remained relatively constant at low Rayleigh numbers due to the dominance of conductive heat transfer. Furthermore, it was concluded that increasing the dimension of the fin inside the cavity blocks the flow and reduces heat transfer coefficient (passive control of fluid flow and heat transfer). Rashidi et al. [158] investigated numerically and experimentally the effect of vertical baffle attached to the absorber on SS solar still performance. In the study, a still with a cover angle of 12.5º was considered and the baffle position was the midpoint of the absorber. Results showed that the use of the baffle increased the performance of the solar still by almost 8% compared to the conventional configuration. Furthermore, the increase in performance was due to the creation of additional cells in the geometry. A cost analysis of both cases was performed and revealed that baffle configuration reduces the cost of fresh water produced. In another study, Rashidi et al. [159] performed an optimisation study to determine the best baffle configuration for the highest SS solar still performance. The investigation was conducted on a solar still with an angle of 14.5º and temperature difference of 15º C. Results of the study showed that the length of the baffle and position directly affect heat transfer within the cavity by creating additional vortices, thereby increasing solar still performance. The selected optimisation technique revealed the existence of an optimum location and length of the baffle that provided the highest solar still performance. Furthermore, the location and length of the baffle depends on whether the baffle is mounted on the absorber or cover surface. In a recent attempt, Subhani and Kumar [39] investigated numerically the effect of baffles on the performance of SS solar still with a fixed cover angle. Three different distances of the baffle from the side wall were considered: 1/3, 1/2 and 2/3. In some cases, mounting a baffle suppressed natural convection inside the geometry which led to a deterioration of the fluid flow and resulted in a lower heat transfer coefficient. Moreover, the author concluded that the best location was 1/2 of the absorber distance which differs from the findings reported by Rashidi et al. [39].

With reference to the aforementioned literature, several researchers have shown great interest on the use of baffles to passively enhance or reduce the magnitude of natural convection inside enclosures. However, only a few have investigated the effect of baffles on natural convection inside a SS solar still. Moreover, despite very few attempts found in literature that used baffles to increase the productivity of these devices, they did not investigate in great detail the interaction between the baffle length, position, solar still geometry and natural convection. Furthermore, the effect of baffles has not been studied in a generalisable way. Therefore, the purpose of this study is to fill the gap by investigating the influence of adiabatic baffles on natural convection inside SS solar still geometry.

4.2. Numerical setup

For this study, a numerical investigation of natural convection inside the selected geometry was performed using numerical model similar to that described in Chapter 3. This was appropriate since the Rayleigh number falls in the range of 3.37×10^{6} and 3.03×10^{9} similar to SS solar still studied in the previous chapter.

4.2.1. Boundary conditions

As shown in Figure 51, the enclosure investigated in the present paper is a trapezoidal enclosure similar to the SS solar still geometry with a thin baffle attached to the top surface. The bottom horizontal (water surface) and top inclined surfaces (glass cover) are differentially heated, whereas the horizontal side walls are assumed to be adiabatic since in solar still side walls are insulated.

The baffle inside the enclosure was assumed to be adiabatic since the main objective of it is to alter the fluid flow inside the enclosure. The considered cavity is filled with saturated humid air in order to reproduce the same physical phenomena between water surface and glass cover in solar stills. Computational fluid dynamics simulations were undertaken for a single slope solar still with cover angles between 10º and 60º, aspect ratios ranging from 5.4 to 1 and Rayleigh number between 8.37×10^6 and 3.03×10^9.

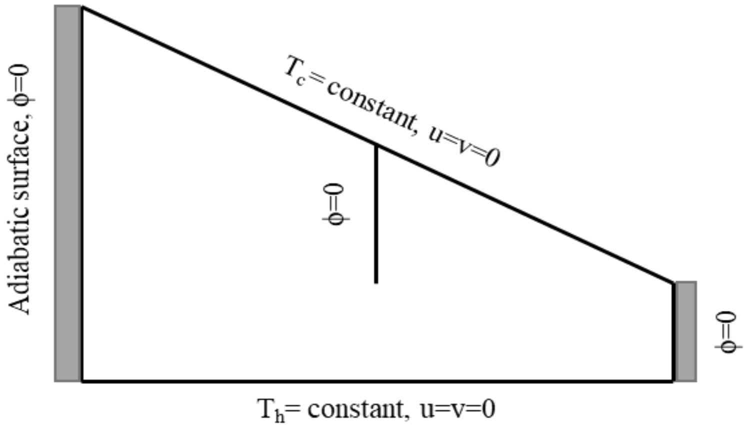

Figure 51: Imposed boundary conditions.

To examine the effect of the baffle on the flow and natural convection inside SS solar still, it was decided to study three different positions and lengths of the baffle. Figure 52 shows the different positions of baffles and their lengths for a given SS solar still geometry.

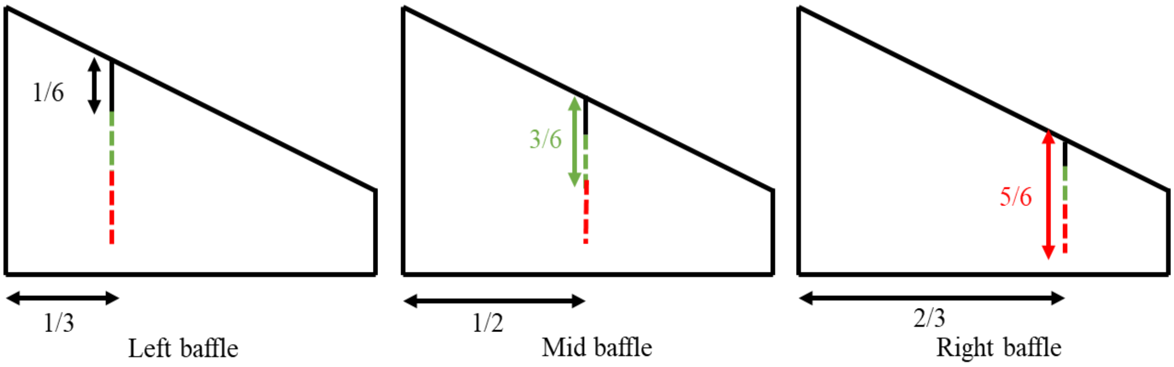

Figure 52: Baffle position and length.

4.2.2. Grid sensitivity

To perform a grid sensitivity analysis, the same mesh configuration described in Chapter 3 was used for evaluating a baffled enclosure. Figure 53 shows a schematic of the generated mesh used in the present modelling. However, since different geometrical parameters were used, it was decided to perform the mesh sensitivity for two arbitrary shapes with different cover angles (10º, 40º) and baffle lengths. Figure 54 depicts the variation of heat transfer coefficient (defined by Equation 21) from the bottom surface for different angles and element sizes. Based on the results, a 10^{-3} m element size is selected because of the insignificant variation in the heat transfer coefficient below the 1 x 10^{-3} m element size.

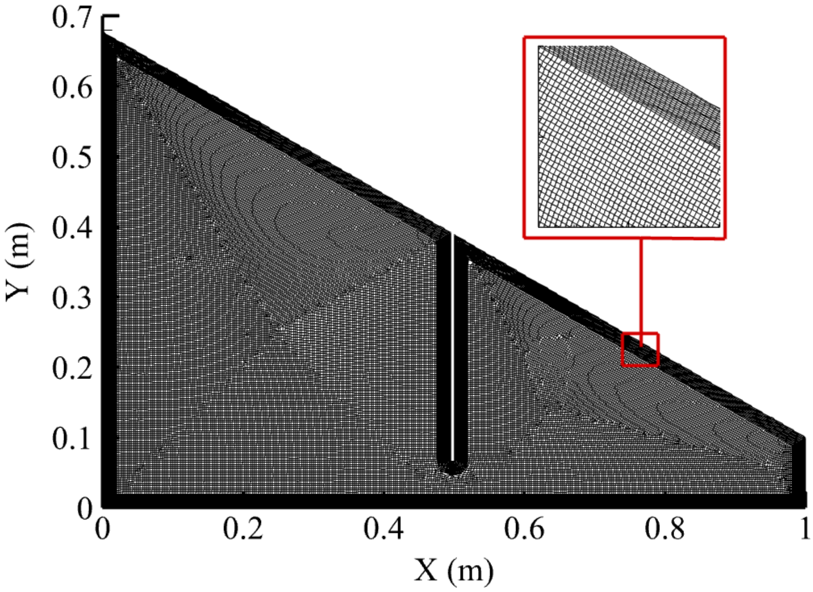

Figure 53: Mesh for modified SS solar still geometry.

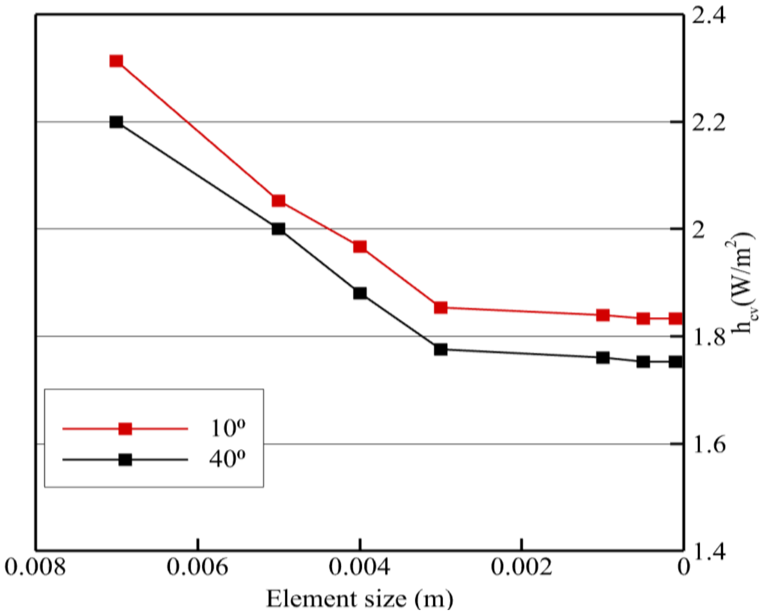

Figure 54: Variation of heat transfer coefficient with the element size at (ΔT=15ºC).

4.3. Experimental setup

Before proceeding to a full CFD analysis, it was necessary to validate the selected numerical model for a modified SS solar still with a baffle. Moreover, it was decided to modify the existing enclosure described in Chapter 3 and attach a baffle to the top surface. In this vein a baffle with a length (d) of 0.16 m was fixed 0.13 m (~1/3 of the base) from the front wall (b =0.13 m), as shown (Figure 55). The baffle was made of 5 mm acrylic sheet and attached to the top cover using strong bonding glue and bolts. The latter material was used in order to allow the laser penetration throughout the enclosure.

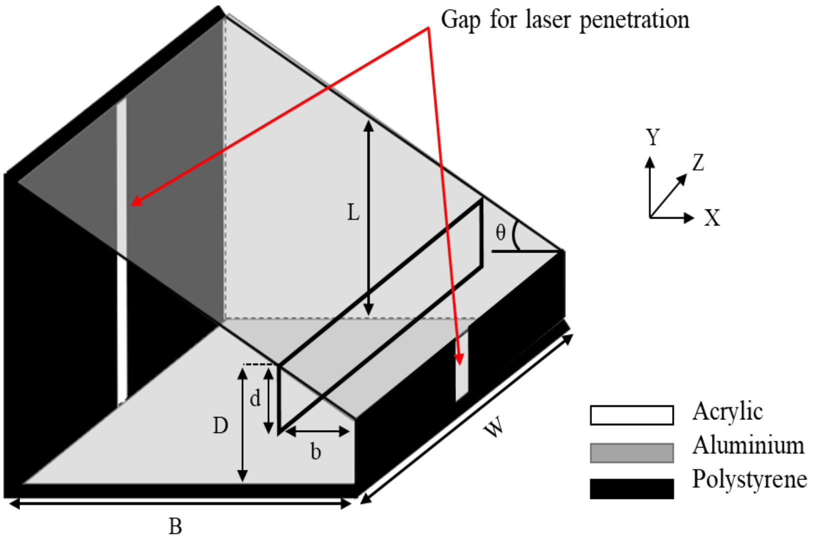

Figure 55: Experimental enclosure.

Similar to Chapter 3, the PIV technique was selected to elucidate the flow behaviour inside the proposed configuration. The same working fluid, tracer particles and equipment parameters mentioned in Chapter 3 were used to investigate the effect of the baffle. Figure 56 shows the PIV setup used in the experimental validation of the numerical model.

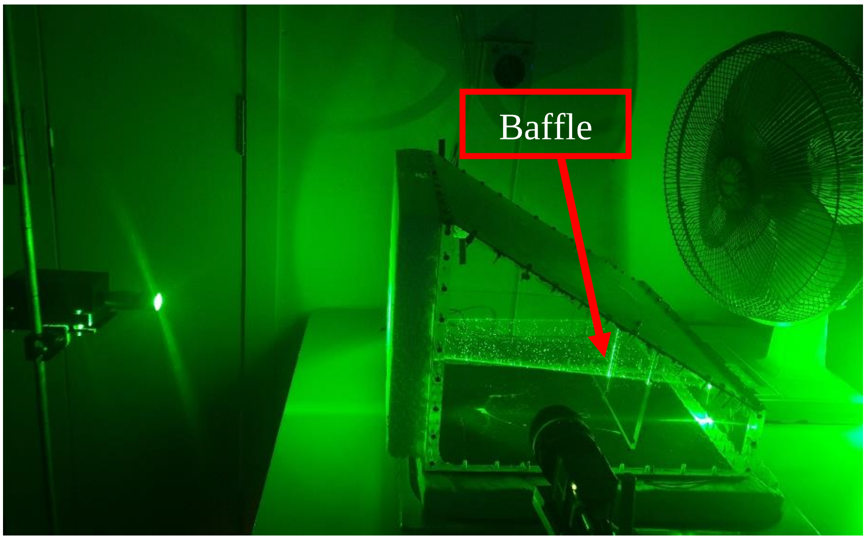

Figure 56: PIV experimental set up.

To maintain temperature uniformity, the bottom and top surfaces were made of 3 mm aluminium sheet. Both walls were coated with matt black paint to minimise laser reflection. In total, 16 equally spaced along X and Y axes Copper-Constantan (T-type) thermocouples were used to monitor the temperature difference and achieve steady state conditions. Each surface (bottom and top) had 7 thermocouples, and the other 2 measured room temperature. Recording of temperature measurements was by a Picolog multi-channel data logger. Typically, after 8 hours from start-up, steady state conditions were achieved as shown in Figure 57.

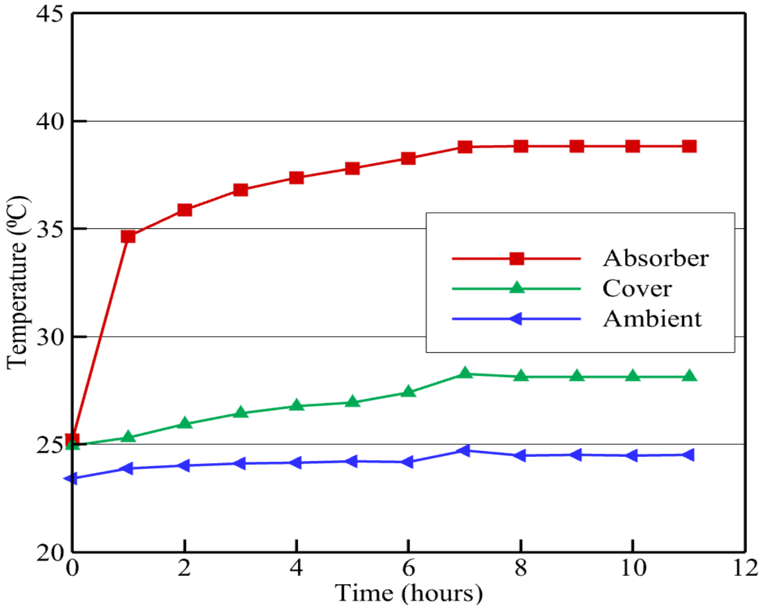

Figure 57: Experimental steady-state temperature measurement.

4.4. Results and discussion

4.4.1. Validation

To verify the selected numerical model, steady state boundary conditions acquired from the PIV experiment were applied to the CFD simulation with the same geometry and fluid properties. Figure 58 shows velocity contour at a plane 0.2 m along the geometry length (i.e. in the z-direction). For both cases (PIV and CFD) same flow features can be seen from velocity contours and streamlines, two-cell flow is achieved with a significant plume rising at approximatively X=0.08 m. At X=0.27 m, the flow from the left side is forced to slope toward the hot surface because of the attached baffle, allowing the formation of a secondary cell on the right side of the baffle. A small vortex due to the counter-rotation of the two cells can be seen under the baffle.

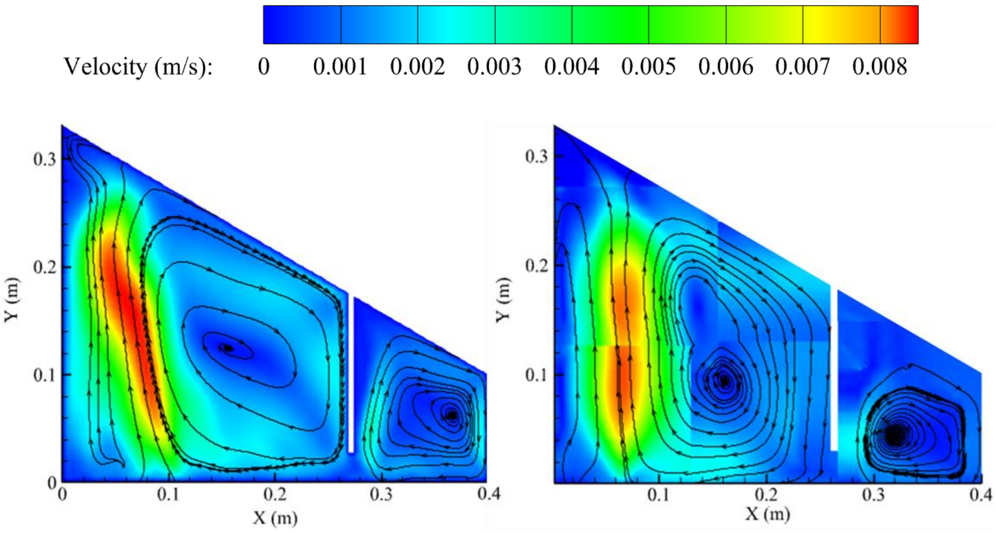

a: CFD

b: Experiment

Figure 58:Cross-sectional velocity contour in the middle of the geometry (0.2m, AR=2.6, θ=30º, Ra=1.38×108), a: CFD simulation, b: Experiment.

As additional validation, Figure 59 shows the velocity profile at Y=0.05 m for both the PIV experiment and the CFD simulation. In both cases, the velocity magnitude is very low near the left wall. Further from the wall however, the plumes in the contours are translated into velocity peaks reaching $6.9 \times 10^{-3}\, m/s$ in the experiment and $7.5 \times 10^{-3}\, m/s$ in CFD results – an error of 8.5%. Moreover, because of the flow approaching the baffle, a drastic drop in velocity can be seen at X=0.27. Again, another rising plume translated to high velocity peaks can be noticed at approximatively 0.28 m due to the second recirculation. Furthermore, the velocity drops through the centre of the cell and again increases near the front wall confirming the existence of secondary flow cell as shown in Figure 59.

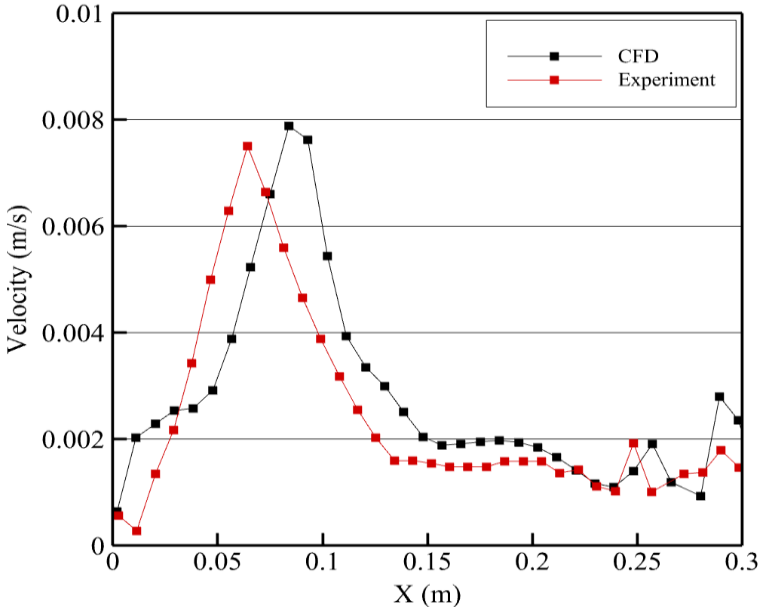

Figure 59: Velocity profile at Y=0.05 m.

4.4.2. Effect of the mounted baffle on heat transfer coefficient

Having validated the numerical model, the effects of the baffle length and its location on heat transfer coefficient were investigated. For each angle considered, three positions of the baffle (1/3, 1/2, 2/3 of top surface) and three baffle lengths (1/6, 3/6, 5/6 of total height (H) between the top and bottom surfaces for the selected baffle position) were studied.

4.4.3. Left positioned baffle

As described in section 4.3, six sets of angles were investigated in this study. The effect of the baffle on the selected angles was then compared to the cases without the baffle. Figure 60 shows the effect of baffle's length on heat transfer coefficient when positioned on the left side (1/3).

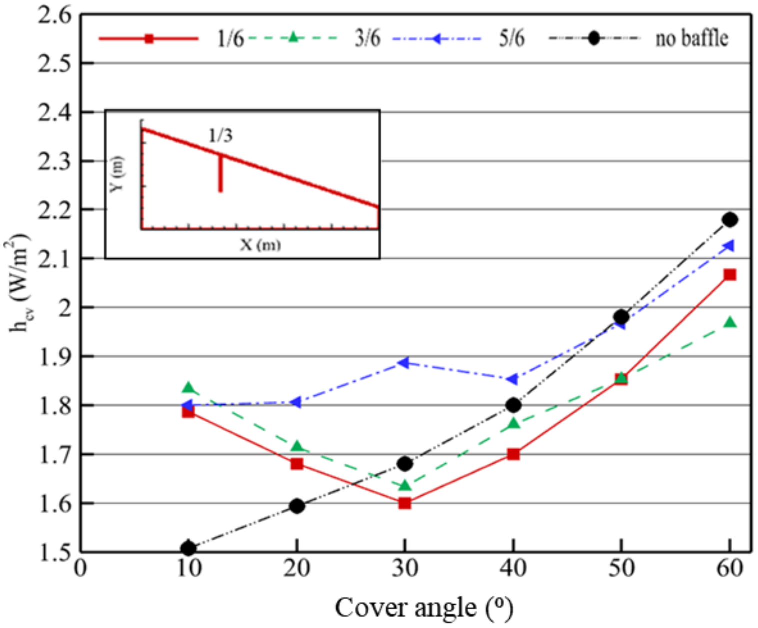

Figure 60: Near high wall positioned baffle effect on heat transfer coefficient.

In cases without the baffle, the heat transfer coefficient is proportional to the angle, due to the increase in distance between the bottom and top surfaces; the velocity increases leading to a higher heat transfer coefficient as reported in Asan and Namli [160]. At 10˚ cover angle, it can be noticed that the baffle increases the heat transfer coefficient by approximatively 20%. However, a difference can be observed between the three lengths of the baffle, with higher heat transfer coefficient for the (3/6) baffle due to the multiple cellular flow with higher velocity than baffle with (1/6) height. Moreover, the (5/6) baffle shows a marginally higher heat transfer coefficient compared to (1/6). This is because of the higher velocity magnitude for 5/6 relative to 1/6 baffle. Figure 61 depicts the transitions from monocellular flow in case of geometry without the baffles to multicellular flow for geometries with different baffle lengths. The latter figure (Figure 61) shows as well the close relation between the flow velocity and the geometry configuration.

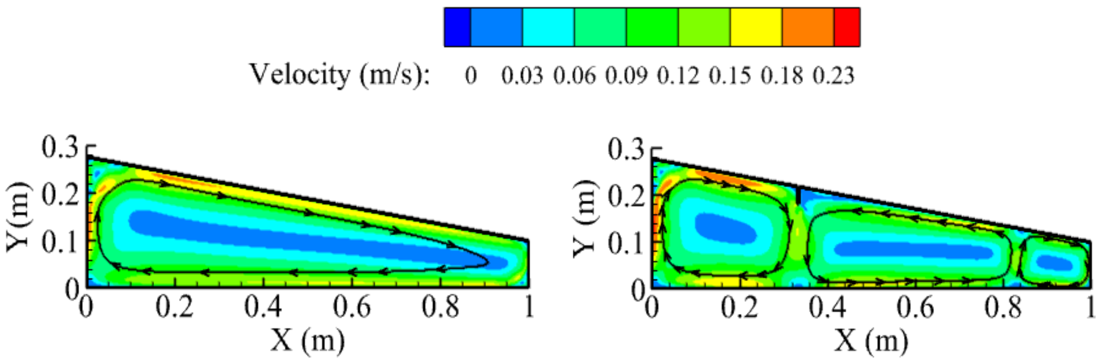

a: no baffle

b: 1/6 baffle

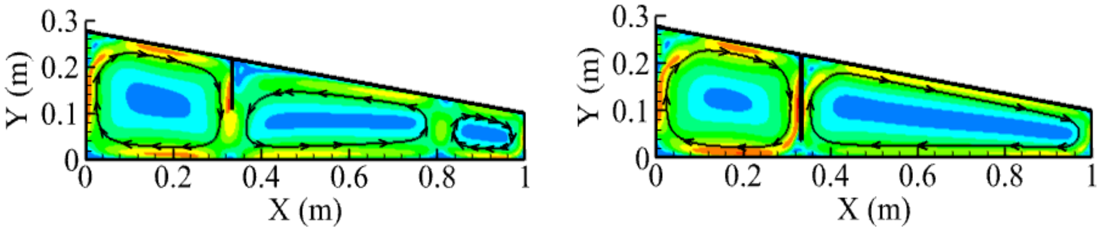

c: 3/6 baffle

d: 5/6 baffle

Figure 61: Velocity contour for cover angle 10 a: No baffle b: 1/6 c: 3/6 d: 5/6.

It is seen from Figure 60 that, despite the decrease in heat transfer coefficient for baffle lengths (1/3, 3/6), both geometries performed better than enclosure without a baffle for a 20˚ cover angle. This is due to the transition from monocellular to multicellular flow when adding the baffle within the geometry. For both baffle lengths, the heat transfer coefficient continues decreasing until it reaches its lowest value at 30˚ cover angle having a lower performance than the geometry without baffle. This is a result of the blockage caused by the baffle to the flow from the cover surface and by preventing the development of an independent multicellular flow structure. Moreover, the blockage of the flow by the baffle causes the formation of a low velocity recirculation on the right side of the baffle as shown in Figure 62 (a-d). Beyond a 30˚ cover angle, the heat transfer coefficient increases with the angle, however the value of heat transfer coefficient for enclosure without baffle is still higher than the geometries with baffles length of 1/6 and 3/6. As mentioned above, this is due to the destruction of the flow from the left side of the baffle. At 50˚ cover angle however, 1/6 baffle heat transfer coefficient becomes equal to the 3/6 baffle length to become higher at 60° angle. This is because the shorter baffle allows easier reconstitution of the monocellular flow than the longer baffle (3/6) (Figure 62, a and d).

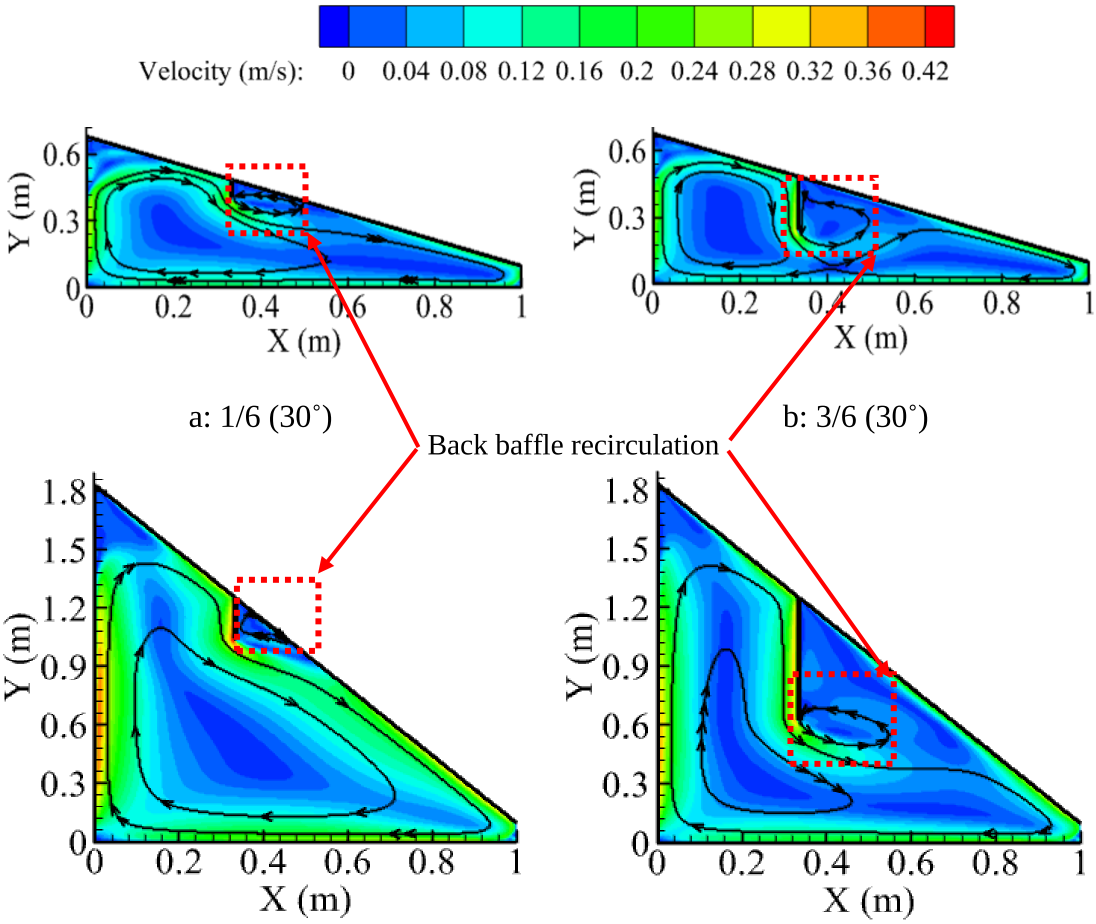

a: 1/6 (30°)

b: 3/6 (30°)

Back baffle recirculation

c: 1/6 (60°)

d: 3/6 (60°)

Figure 62:Velocity contour for 30° and 60°.

Contrary to the effects of both previously mentioned baffles, 5/6 baffle first increases the heat transfer coefficient with the increase of cover angle between 10° and 30°. This indicates that the longer baffle (5/6) is more efficient for partitioning the flow inside 20° and 30° geometries than for other cases. At a 40° cover angle, the heat transfer coefficient decreases; this is due to the increasing strength of the cell located on the right side of the baffle which supresses the flow on left side of the baffle. This phenomenon is observed when the two cells rotate in opposite directions (Figure 63). The same flow pattern is observed at 50˚ and 60˚, however the heat transfer coefficient obtained is lower than the case without the baffle.

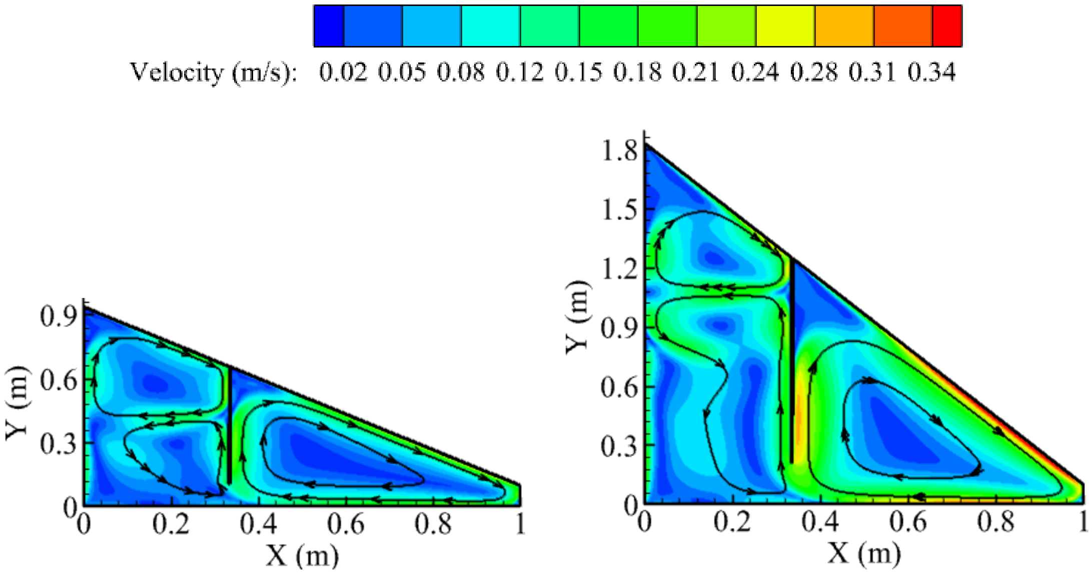

a: 5/6 (40˚)

b: 5/6 (60˚)

Figure 63: Velocity contour for 40˚ and 60˚.

Evidently, the results show that left baffle attachment does not increase the heat transfer coefficient in all cases. It appears that it is more effective to use left baffle at lower angles since it easier to obtain multicellular flow than at higher angles.

4.4.4. Middle positioned baffle

Figure 64 shows the variation of heat transfer coefficient from the bottom surface for different angles and lengths of the baffle situated at the middle of the top surface

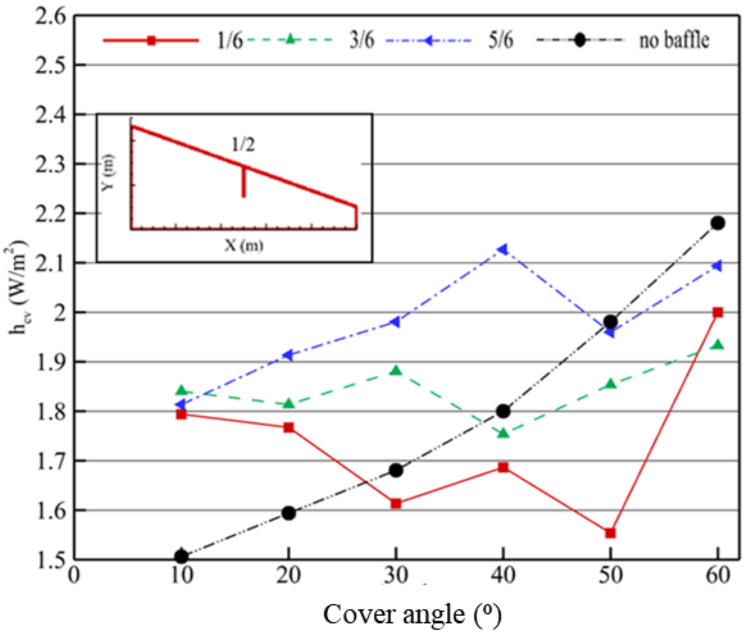

Figure 64: Effect of middle baffle on heat transfer coefficient

At 10° cover angle, it can be observed that the middle baffle has similar effect (increase) on the heat transfer coefficient magnitude to left positioned baffle. This is due to the formation of the same number of cells and velocity magnitude difference between 3/6 and 5/6 baffle. It worth noting that the cells in this case are slightly moved toward the right side, this transition is caused by the location of the baffle. For both baffles 1/6 and 3/6, the heat transfer coefficient decreases at 20° angle, this is due to the increasing height between the top and bottom surfaces forcing the flow to start losing its multicellular characteristic (Figure 65).

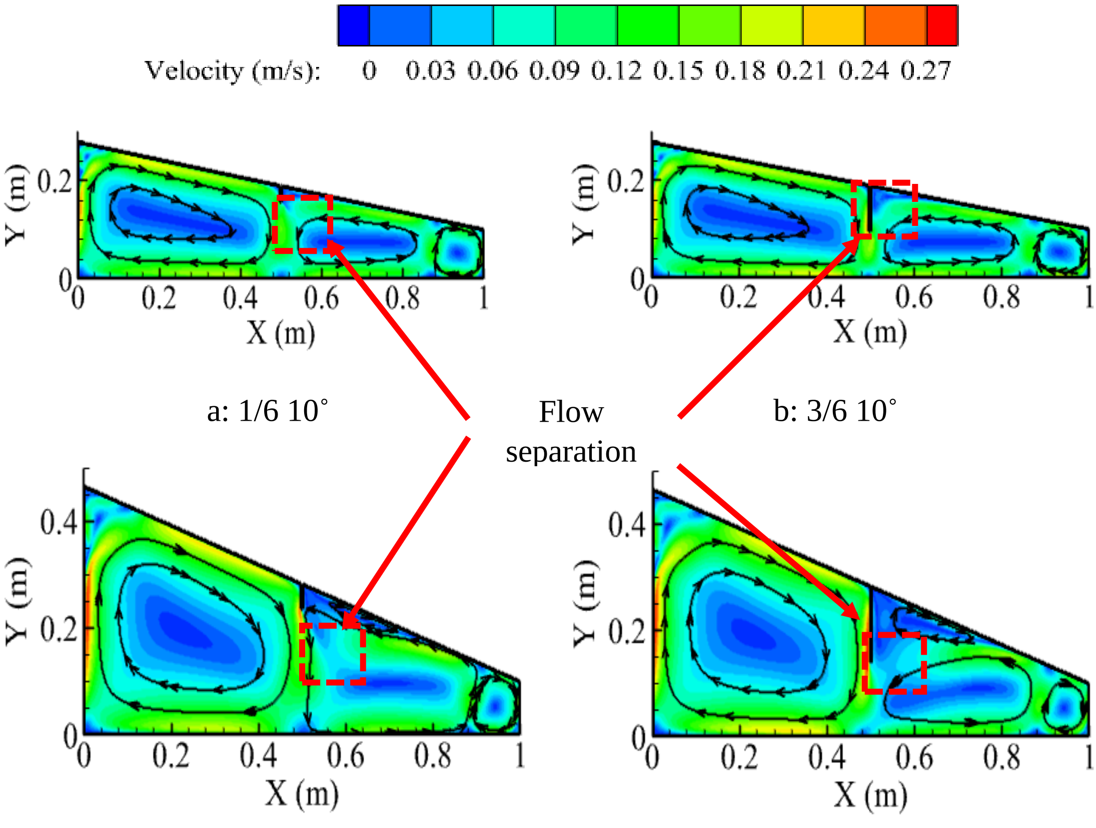

a: 1/6 10°

b: 3/6 10°

c: 1/6 20°

d: 3/6 20°

Figure 65: Velocity contour at 10° and 20° cover angle.

At a cover angle of 30°, a noticeable drop in the heat transfer coefficient can be see for baffle with 1/6 length, this is due to the increasing distance between the bottom and top surface forcing the flow to be monocellular same observed in Figure 62 (a). However, for 3/6 and 5/6 baffle length, the heat transfer coefficient increases due to the multicellular flow pattern. At 40° cover angle, despite 1/6 baffle performance being lower than no baffle geometry, the heat transfer coefficient increases due to the relatively faster flow compared to cover angle equal to 30°. A drastic decrease can be seen at 50° because of a strong interaction between the right and left cell, consequently the left cell is partially positioned above the right cell as shown in Figure 66. The heat transfer coefficient increases at 60° due to the flow becoming monocellular similar to Figure 62 (c), in this case the baffle decreases the flow velocity causing a lower performance than no baffle geometry.

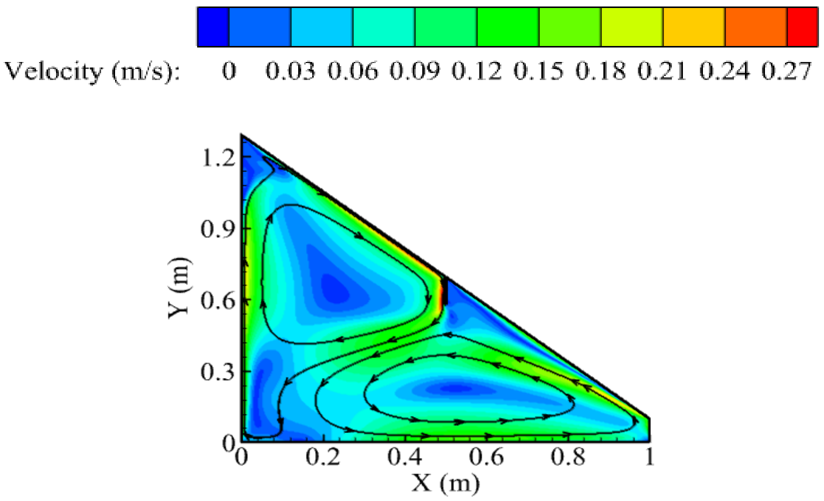

Figure 66: Velocity contour at 50º cover angle (1/6 baffle).

It is seen in Figure 67 that for 3/6 baffle case the heat transfer coefficient decreases to reach its lowest value at a 40˚ cover angle. Even though multicellular flow occurs at 40˚, the left cell supresses the upward flow of the right cell making its rotation weaker compared to the left cell (Figure 67, a). On the other hand, the heat transfer coefficient increases at 50˚ and 60˚ because of the increasing velocity due to the distance between the top and bottom surfaces (Figure 67, b).

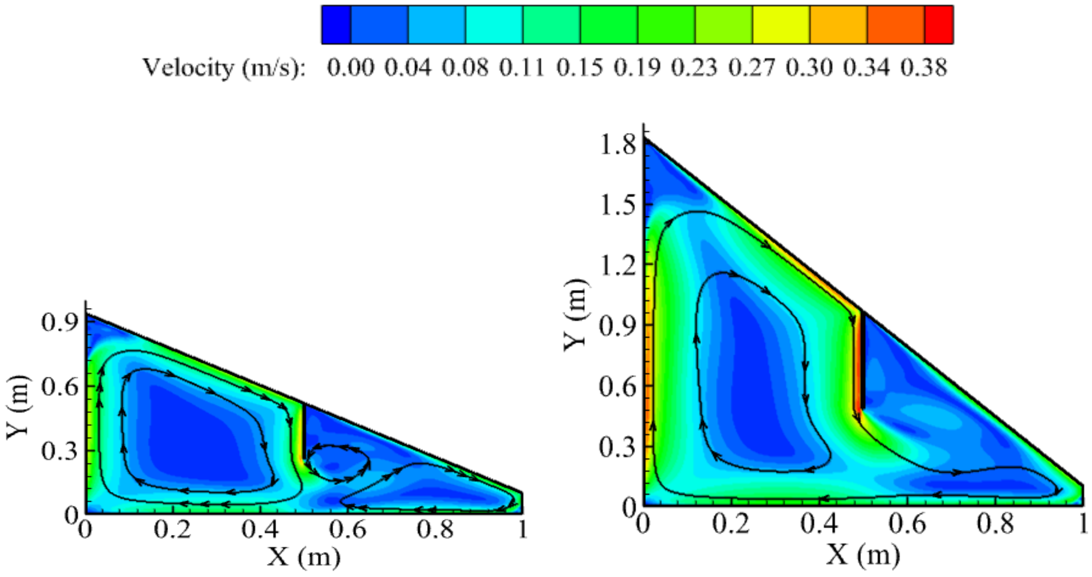

a: 40 ˚

b: 60˚

Figure 67: Velocity contour a: 40˚, b: 60˚ (3/6 baffle).

Contrary to baffles with 1/6 and 3/6 length, the 5/6 baffle increases the heat transfer coefficient which reaches its highest value at cover angle 40˚. This is due to the strong multicellular flow achieved with the help of the baffle length. At 50˚ cover angle, the heat transfer coefficient diminishes to fall under the performance of a cavity with no baffle. This is due to the right cell overcoming the downward flow of the left cell, same observed in Figure 63 (b). As mentioned before in 4.2.2, this happens because of the opposite rotational direction of the two cells on each side of the baffle.

For the 1/6 baffle length, the use of a baffle has a positive impact on heat transfer coefficient only at 10˚ and 20˚. For 3/6 baffle, in addition to higher heat transfer coefficient at 10˚ and 20˚, it reached its highest value of heat transfer at 30˚. However, performance of the 3/6 baffle diminishes at 40˚, 50˚ and 60˚ due to the flow characteristics. Finally, 5/6 baffle increases heat transfer coefficient compared to no baffle geometry in wider range of angles (10˚-40˚). At 50˚ and more, the baffle makes blockage effects on the flow, thus decreasing heat transfer.

4.4.5. Right positioned baffle

Figure 68 depicts the effect of the baffle attached at the 2/3 position on the heat transfer coefficient for various angles and baffle lengths.

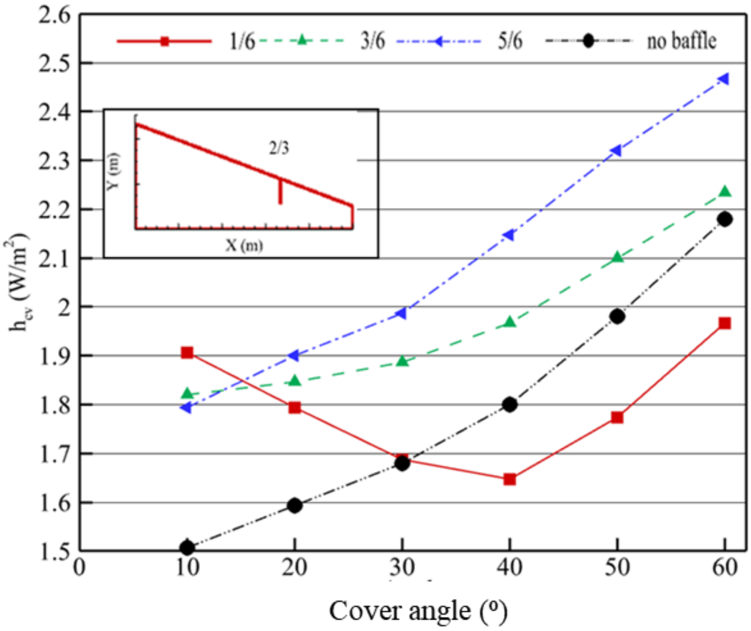

Figure 68: Near short wall positioned baffle effect on heat transfer coefficient.

Contrary to left and middle positioned baffle, the 1/6 baffle outperforms the 3/6 and 5/6 on the magnitude of heat transfer coefficient at 10˚ cover angle. Moreover, 3/6 baffle heat transfer coefficient is slightly higher than for the 5/6 baffle. As shown in Figure 69, the reason for the difference in heat transfer coefficient is due to the number of cells generated by the inclusion of the baffle. For instance, at 1/6 baffle length multiple (4) recirculations are observed and a lower velocity magnitude compared to 3/6 with three cells and 5/6 with two cells and relatively higher velocity. Consequently, the vertical flow in the upward flow carries heat more efficiently at higher number of recirculation cells than high velocity flow with lower number of recirculation cells.

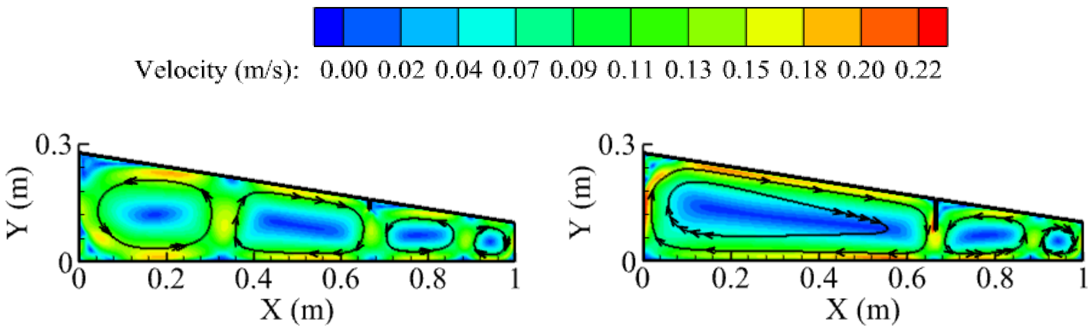

a: 10˚ 1/6

b: 10˚ 3/6

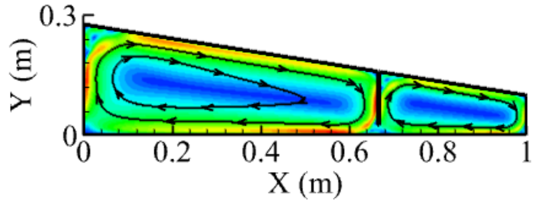

c: 10˚ 5/6

Figure 69: Velocity contour for right baffle at 10˚.

The efficiency of the 1/6 baffle gradually decreases to reach its lowest value at 40˚ lower than for the no baffle geometry (Figure 70). This is due to the length of the baffle not permitting the creation of the multicellular flow and acting as a barrier destroying the downward flow adjacent to the top surface. The heat transfer again increases at 50˚ and 60˚ due to higher velocity caused by the increase in distance between bottom and top surface.

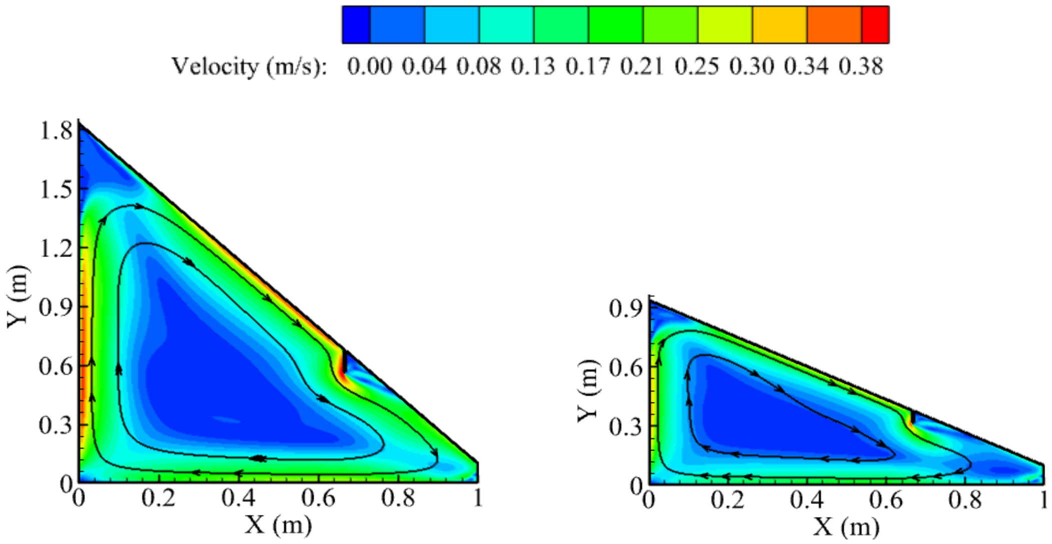

a: 60˚

b: 40˚

Figure 70: Velocity contour at 60º and 40º for 1/6 baffle length.

For both the 3/6 and 5/6 baffles, the heat transfer coefficient increases with the increase of cover angle. This is because the flow for both geometries at this stage is from two cells. This was not possible at baffle positioned in the left or the middle for both 5/6 and 3/6 baffle is due to the left cell recirculation suppressing that of the right cell. However, for right located baffle and due to the shorter distance between the top and bottom surfaces, two cells can be observed. Furthermore, 5/6 outperforms the 3/6 baffle because in the first case lower resistance is found by the upward flow of the right cell compared to the case of 3/6 baffle. Consequently, the flow at 3/6 baffle is characterised by a more pronounced low velocity recirculation as shown in Figure 71.

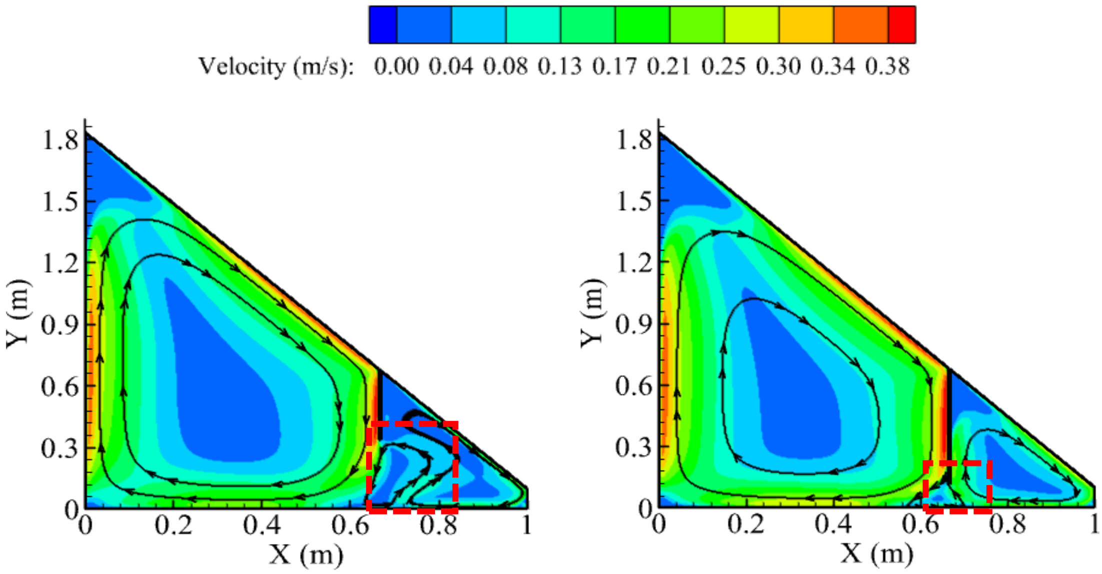

a= 3/6

b= 5/6

Figure 71: Velocity contour at 60˚ for 3/6 and 5/6 baffle length.

For the case of right positioned baffle it can be observed that 1/6 baffle only outperforms 3/6 and 5/6 baffle at the 10˚ cover angle. For the remaining selected angles, 3/6 and 5/6 baffles augment the heat transfer coefficient significantly compared to no baffle geometry.

4.5. Correlating geometry to heat and mass transfer

As discussed in the above section, the position of the baffle, length and SS geometry affect directly the magnitude of heat transfer coefficient from the bottom surface, and this is associated to the interaction of the flow profile and the baffle length and position. To enhance the parametric modelling of modified SS solar stills, a correlation describing the heat transfer coefficient integration with the geometry was established. By generalising the findings acquired from the CFD modelling, a relation between the Nusselt number and parameters affecting heat transfer inside the cavity can be characterised by Equation (28):

$$Nu = Ra^{0.188} * AR^{-0.29} * (\cos\theta)^{-0.5} * \left(\frac{b}{B}\right)^{0.08} * \left(\frac{d}{D}\right)^{0.09} \qquad (28)$$

Where: $2.24\times10^{7} < Ra < 3.03\times10^{9}$; $10^{o} < \theta < 60$; $1.04<AR<5.3$; $0.33<d<0.66$; $0.2<b>1.05$).

As shown in Figure 72, the Nusselt number correlation is in good agreement with the numerical data lying between +15% and -10% of the simulated data. This implies that the previous correlation is suitable to predict heat transfer coefficient in a wider range of angles, aspect ratios, position and length of the baffle.

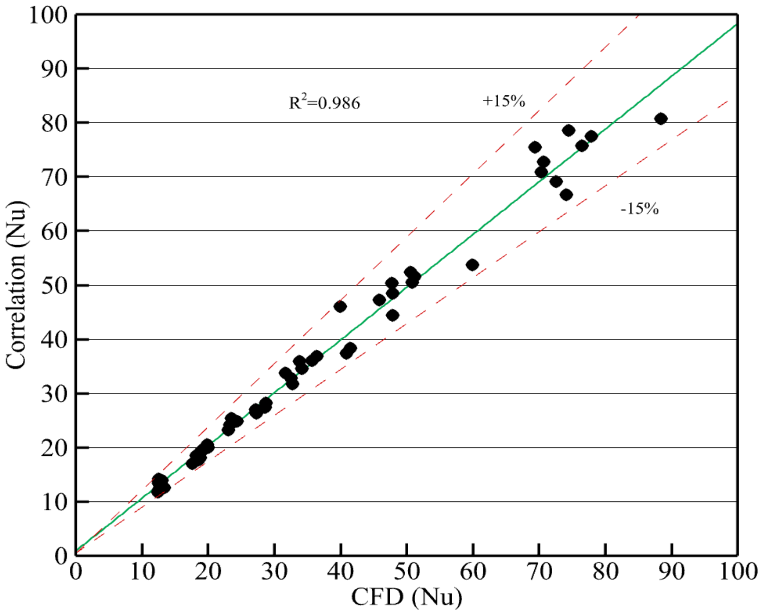

Figure 72: Correlated data of the study.

As mentioned earlier in Chapter 3, Boelter and Sharpley [161] demonstrated that, for convection alone, *Ra* varies with $(T_h - T_c)$, and for isothermal evaporation *Ra* varies with $(\frac{M_c T_c}{M_h T_h} - 1)$. Therefore, to adapt equation 28 to solar still working condition, the authors recommend modifying the previous correlation by utilising a modified Rayleigh number (Equation 27) as shown in Equation 29.

$$Nu' = Ra'^{0.188} * AR^{-0.29} * (\cos\theta)^{-0.5} * \left(\frac{b}{B}\right)^{0.08} * \left(\frac{d}{D}\right)^{0.09} \tag{29}$$

A comparison between the values of the Nusselt number obtained from the new baffle correlation and the previously developed correlation for a conventional SS solar still (Figure 73). Since right positioned baffle (2/3) with a length of 5/6 has superior performance compared to other configuration, it was used in the present comparison. It can be observed from that the baffle correlation estimates a higher Nusselt number than non-baffle geometry correlation, this is to be expected as the heat transfer coefficient is higher in the selected baffle geometry compared to the conventional configuration. However, it is observed that the difference in the Nusselt numbers decreases with the increase in cover angle; this is believed to be due to the errors of the linear regression method used to fit the acquired data from the CFD simulations. In spite of the above, the correlation describes the higher performance of baffle correlation compared to conventional geometry.

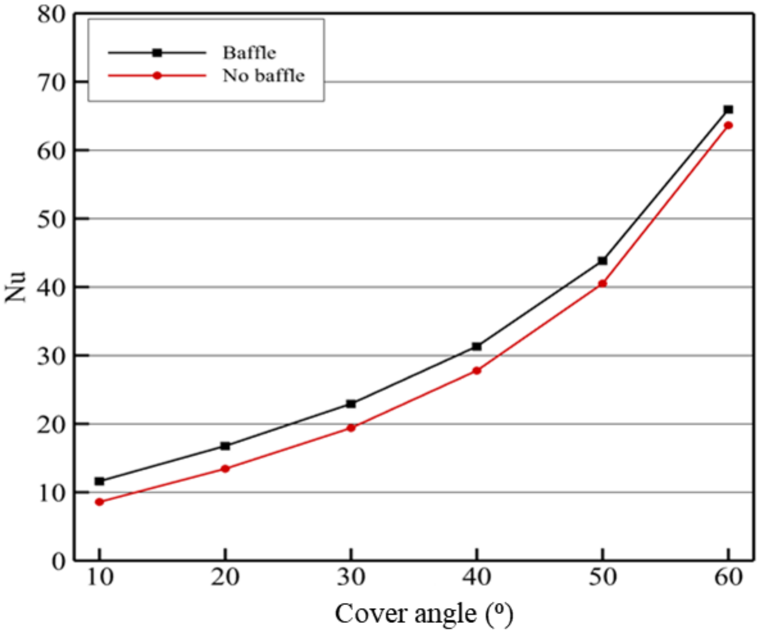

Figure 73: Comparison between conventional and baffle solar still Nusselt number (constant ΔT).

4.6. Conclusion

A comprehensive numerical study has been performed to examine the effect of baffle position and length on natural convection inside the SS solar still geometry for a wide range of cover angles and aspect ratios. Using the PIV technique for validation, the numerical setup was found to be in good agreement with experimental results.

Findings indicate the existence of a very pronounced effect on natural convection magnitude when adding a baffle to alter the fluid flow inside the cavity, and in some cases the baffle increases heat transfer by almost 20%. However, in some cases considered, due to the position and length of the baffle, the latter blocked the flow and decreased the heat transfer coefficient making it lower than for the geometry with no baffle. Moreover, a distinctive effect was found for each baffle position and length effect on heat transfer coefficient. It was found that for the left mounted baffle, the increase in heat transfer coefficient by creating multicellular flow was more pronounced at lower angles than at higher angles, where the baffle blocked the flow and decreased heat transfer coefficient. A similar effect was found for the right positioned baffle, however, the increase in heat transfer coefficient compared to the no-baffle geometry was observed over a wider range of angles. Furthermore, the right positioned baffle was found to be more efficient in separating the flow cells through all the range of selected angles. Further results show that a close relation exists between the length of the baffle and the strength and rotational direction of vortices.

A correlation was developed based on data acquired from CFD results, and good agreement was found between both the numerical and correlation equation results. Moreover, it was demonstrated for several configurations, that predicted Nusselt number from baffle solar still is higher than the developed correlation of conventional solar still. In summary, the study has shown in detail the effect of baffle inclusion on the fluid flow inside SS solar still geometry and the natural convection magnitude between water surface and glass cover.

CHAPTER 5: PERFORMANCE INVESTIGATION OF SINGLE SLOPE SOLAR STILL

5.1. Introduction

In the previous chapters, numerical investigations of natural convection within SS solar stills have been carried out. It was determined that geometrical factors directly impact the natural convection inside conventional SS solar stills. Moreover, it was demonstrated that the introduction of a baffle attached to the cover surface leads to the creation of a multicellular flow and a consequent increase in natural convection heat transfer coefficient inside the enclosure. The results of CFD simulations were used to develop appropriate correlations for conventional and modified SS solar still. In this chapter, the use of both correlations shall be examined to substantiate the hypothesis that changing the geometry (aspect ratio and cover angle) directly affects the yield from solar still, and that a higher natural convection coefficient engendered by the introduction of the baffle leads to a greater water yield compared to conventional configuration.

Before proceeding to a full parametric analysis, it necessary to verify the validity of the developed correlations in predicting the outdoor performance of both configurations (conventional and baffle solar stills). To do this the previously developed mathematical model was used to predict thermal state conditions and yield.

5.2. Conventional solar still correlation performance against in situ experiment

Starting with the conventional solar still, the developed correlation (Equation 26) in Chapter 3 was used to calculate the convective heat transfer $h_{c\,W-G}$. Predicted results (thermal state conditions and yield) were than compared to the experimental measurements. It is worth mentioning that the input weather data used in the mathematical model are the same reported in Chapter 2 (20th November 2020, weather conditions: Figure 20).

Figure 74 shows the predicted temperature of the water layer and cover surface against experimental variations. It can be observed that the mathematical model accurately predicts water temperature. However, glass temperature predictions show some discrepancies between 13:00 and 16:00 which are believed to be due to the uncertainties of the thermocouple used to measure the glass cover and fluctuation in the variation caused by the use of only two thermocouples (to avoid the shading of solar irradiation). It is worth mentioning that a contrary observation was noticed in the water temperature due to the average of multiple thermocouples readings and the high specific heat capacity of water damping the fluctuation (low fluctuation).

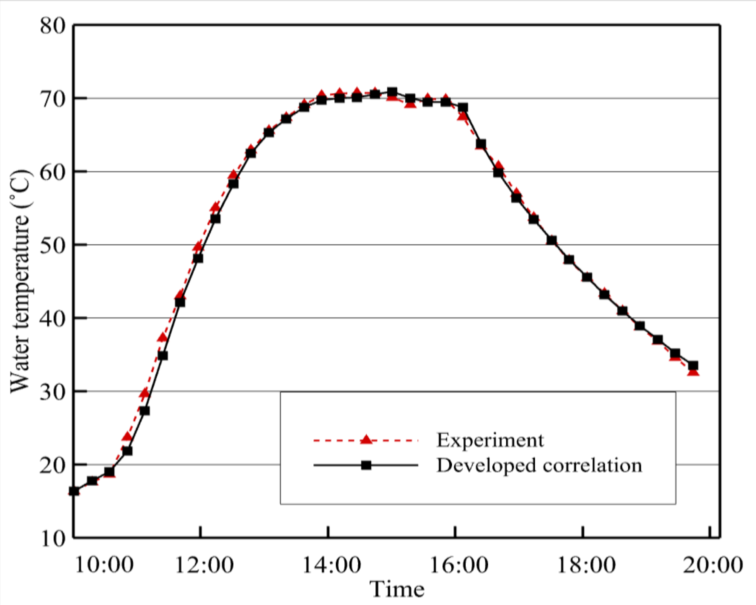

a

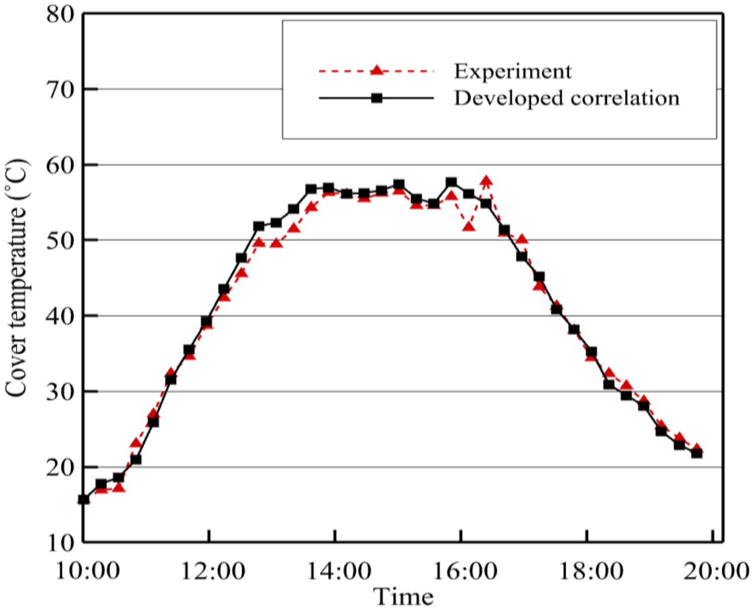

b

Figure 74: Comparison between experimental and predicted water and cover temperature using the developed correlation.

Figure 75 shows the temperature difference between the cover glass and water surface. It is clearly shown that the change in the temperature difference between cover and water is predicted more accurately compared to previous correlations. This because the developed correlation estimates a lower heat transfer coefficient which results in a higher temperature difference compared to the other correlations.

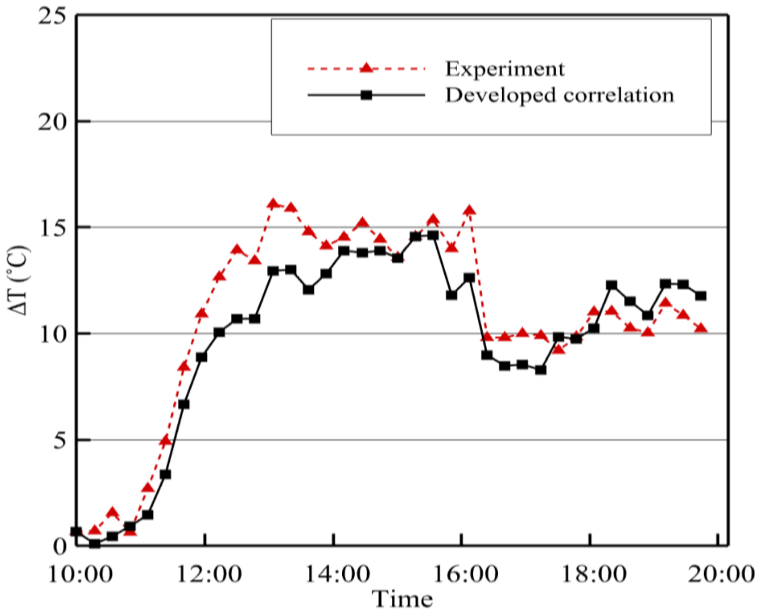

Figure 75: Comparison between experimental and predicted temperature difference (ΔT) using the developed correlation.

Figure 76 demonstrates the predicted hourly and total cumulative daily of distilled water against measured variations. It is clear that for both simulated model and experiment, water production increases with the increase in temperature of the water which is due to the increasing solar irradiation. It is also notable that predicted hourly production is higher than experiment results around 14:00 and after 18:00 which shows that the correlated model predicts the exact trend of water production and temperature. However, a small difference in total cumulative productivity (Figure 76, b) is observed between the experiment and model, this difference is due to the temperature difference between the cover and water being lower in the simulation than in the experiment as seen in Figure 75. This discrepancy is believed to be due to the fluctuating temperature of the cover caused by the small number of thermocouples used to measure the temperature of the glass cover.

As mentioned in Chapter 2, all previously examined correlations predicted lower temperature differences than the experiment while overestimating water production. By contrast, distilled water production predicted by the current developed correlation is lower than in the experiment (2%) due to the slightly lower predicted temperature difference. This shows that the predicted temperature difference magnitude is proportional to water production (high temperature difference leads to high water production), an observation that is consistent compared to existing correlations.

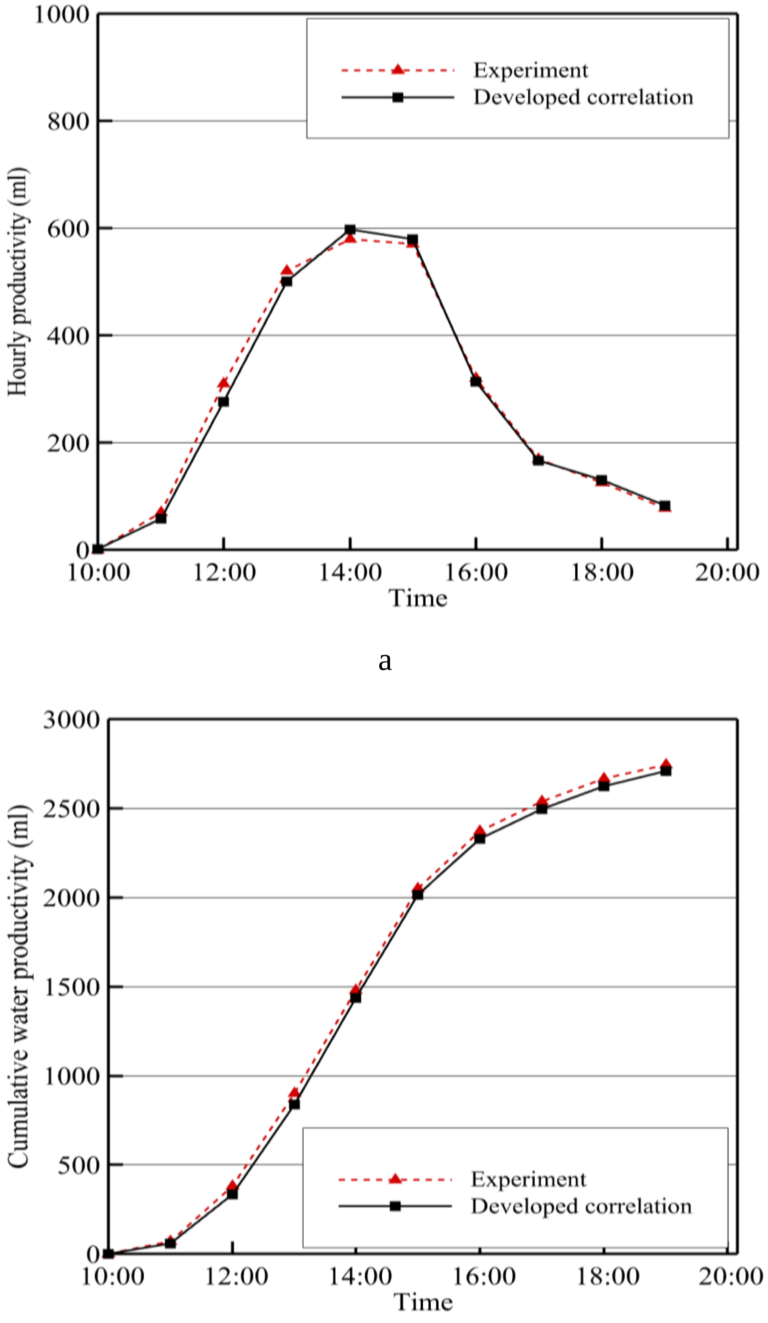

a

b

Figure 76: Predicted performance against measured data, a: hourly yield, b: cumulative yield.

5.3. Baffle solar still correlation performance against in-situ experiment

By utilising the same experimental SS solar still described in Chapter 2, modifications were made to allow the placement of the baffle inside the enclosure. An acrylic baffle with a length of 1m, 0.2m width and 3mm thickness was fixed at 0.33m from the front wall. This configuration was selected as it corresponds to the highest heat transfer coefficient encountered for SS solar still with 30˚ cover angle as shown in Figure 77.

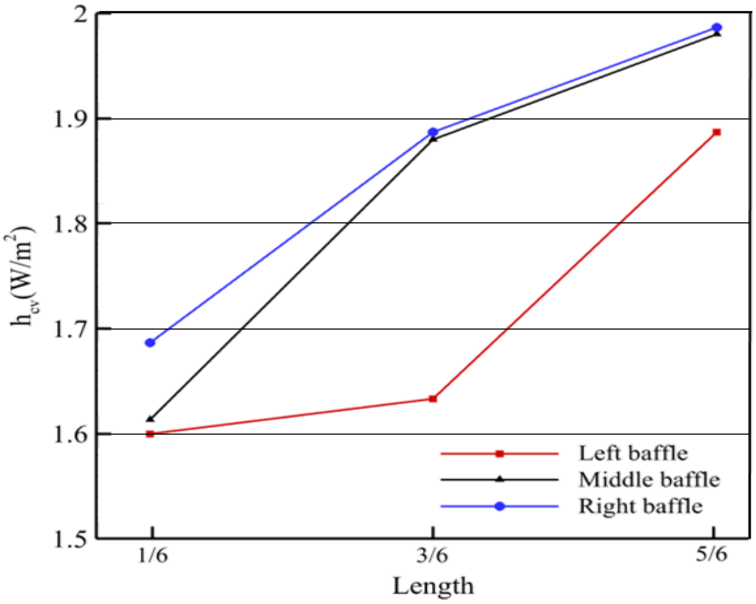

Figure 77: Effect of baffle position and length on convective heat transfer coefficient for 30˚ configuration ΔT=15ºC.

As shown in Figure 78, brackets were attached to the side wall, this allowed placement of the baffle within the enclosure at the desired location. To collect the water condensed along the cover (between the back wall and the baffle), an additional channel was added to the baffle having an inclination of approximately 10˚ to collect water. A gasket was placed in between the glass cover and baffle to efficiently separate both sides of the enclosure (back wall side and front wall side). Finally, an opening was made on left side wall to collect, and measure condensed water accumulated in the channel of the baffle which was made of a transparent tube and fixed with silicon glue to avoid shading that might have affected the solar irradiation received by the absorber.

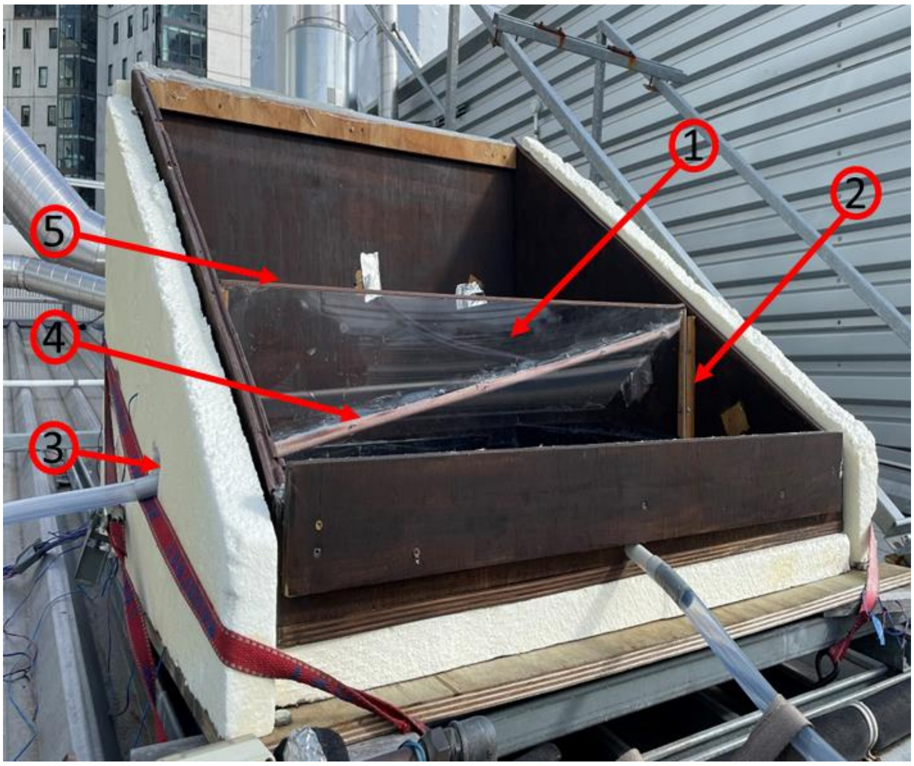

Figure 78: Experimental setup showing the modification made on the previously made solar still, 1: glass (baffle), 2: brackets, 3: distilled water exit, 4: water channel, 5: gasket.

In order to take into account, the effect of the baffle on the SS solar still's performance, the correlation developed in Chapter 4 (Equation 29) was used to calculate the convective heat transfer coefficient between the glass cover and water surface. The baffle was considered to be adiabatic and having no significant effect on solar irradiation received by the absorber. Simulation results were then compared to the experimental measurements. The experimental investigation was conducted 4th December 2020 on the roof of the mechanical engineering department at Auckland University of Technology, and weather data of the selected day are shown in Figure 79.

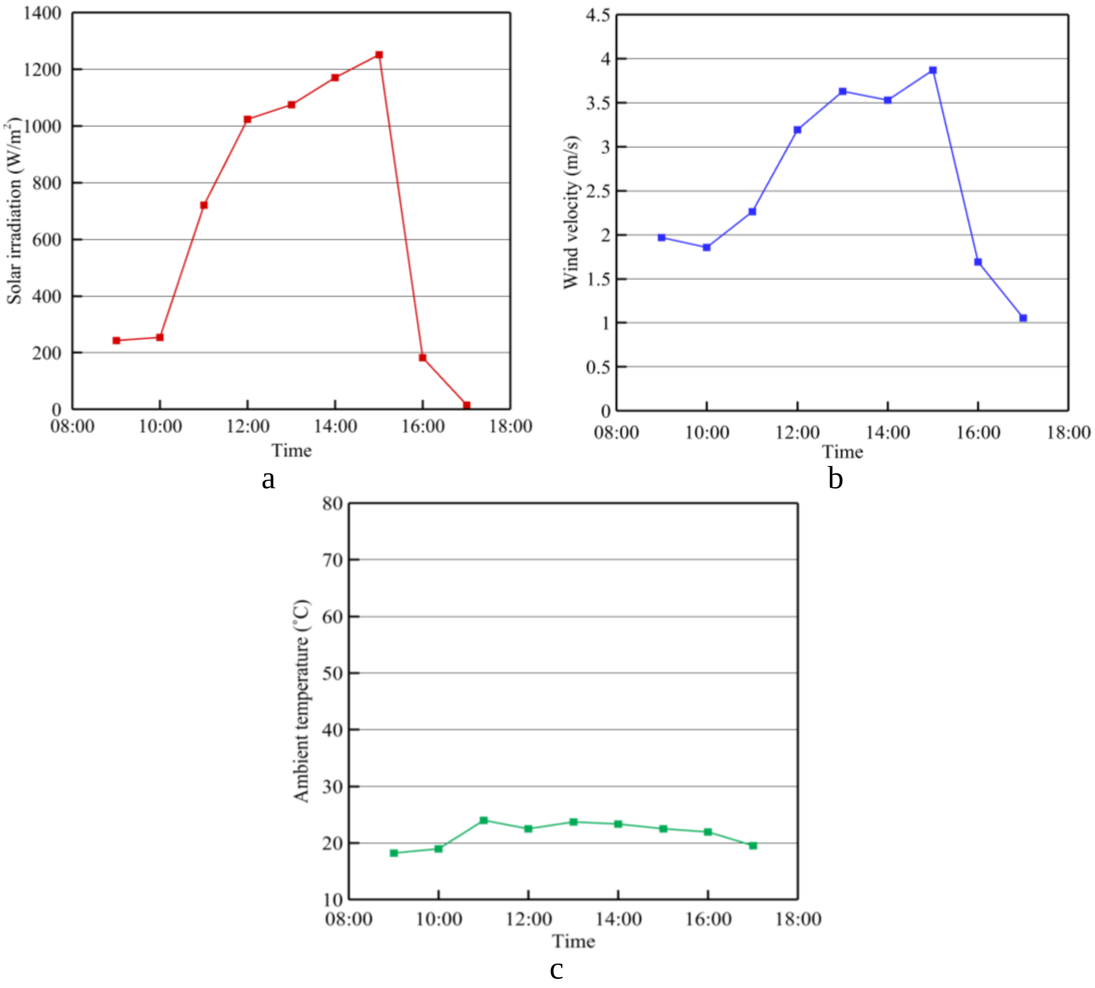

Figure 79: Weather conditions for baffle experiment (4th December 2021), a: solar irradiation, b: wind velocity, c: ambient temperature.

Figure 80 shows the predicted temperatures of the water and cover surface against the in-situ measurements. It can be observed that from Figure 80 (a) that the model predicts the temperature of the water very well but with a slightly higher and lower estimation in the morning and afternoon respectively. However, even though a good agreement between the predicted and measured temperatures of the cover is seen, discrepancies in glass cover temperature estimation are more apparent compared to water temperature prediction – the same as observed in the previous Chapter 3, refer to Figure 80 (b). This discrepancy is believed to be due to the fluctuations caused by the small number of thermocouples used to measure the glass cover temperature.

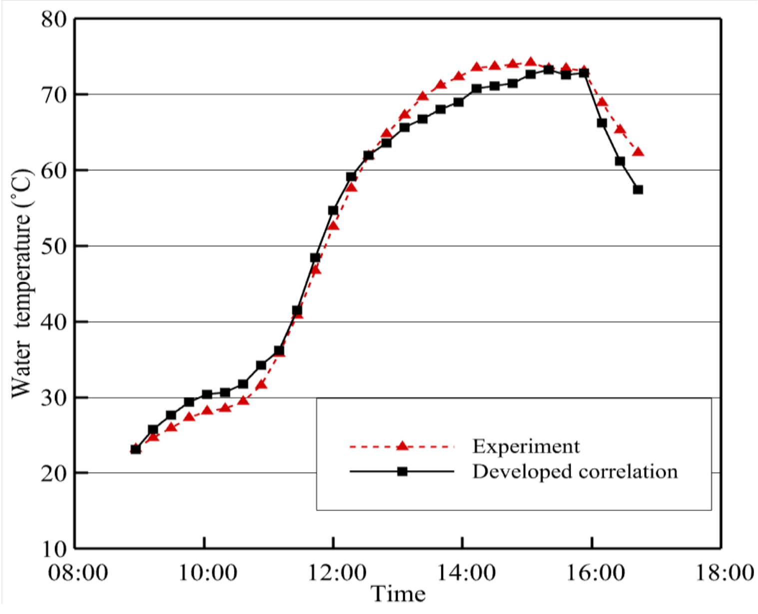

a

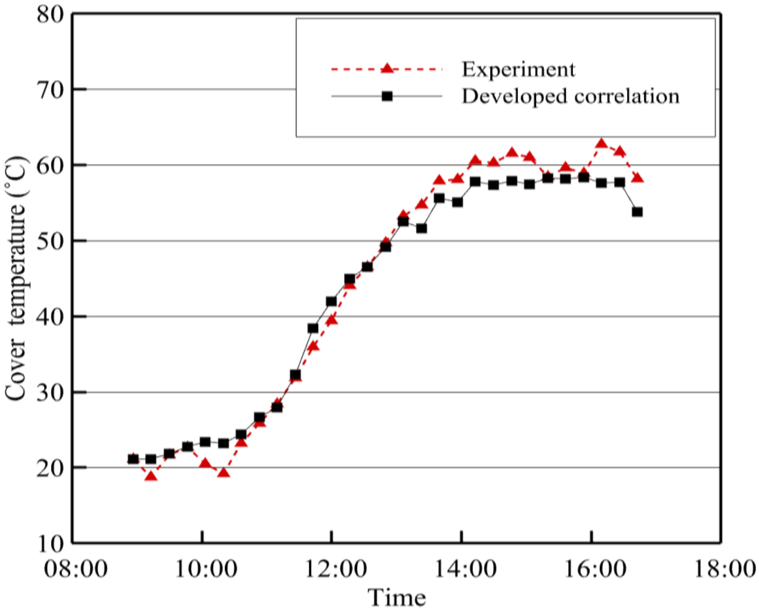

b

Figure 80: Predicted vs simulated results of the water and glass cover.

Figure 81 shows the comparison between predicted and simulated results of the temperature difference between the glass cover and water surface. As is clear from the heat and mass transfer analogy, the water yield is directly linked to the temperature difference between the water and glass cover. Therefore, it is important to carefully compare the temperature difference between the water and glass cover. From Figure 81, it can be seen that the predicted temperature difference behaviour is in good agreement with the experimental measurements. However, a few discrepancies can be noticed in the morning due to the high fluctuation in the glass cover measurements.

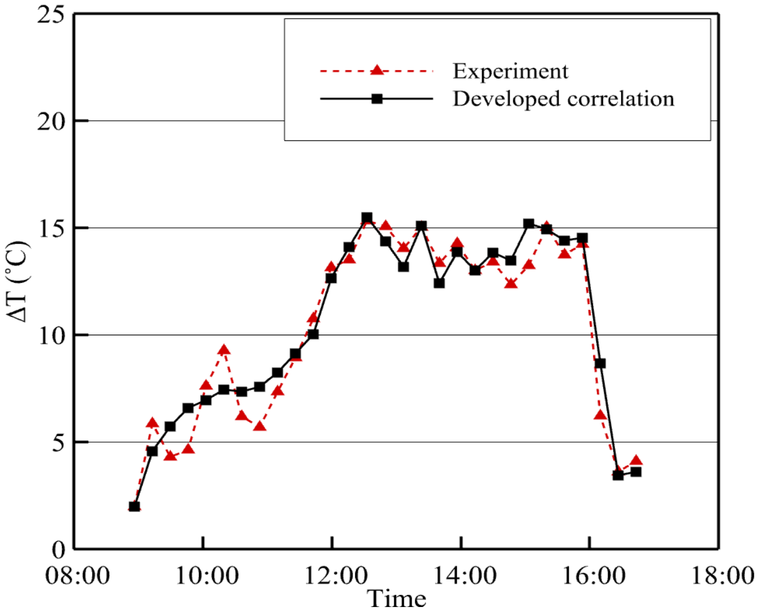

Figure 81: Temperature difference between glass cover and water.

The variation in hourly and daily cumulative water yield of the SS solar still are depicted in Figure 82. Again, it can be seen that, in the morning during the initial hours of the experiment, the mathematical model predicted higher water production compared to the experiment measurements. However, in the afternoon the experimental measurements surpassed the modelled ones. This is because the temperature difference as shown in Figure 81 corresponds to the same change in water yield. Given the above, it can be inferred that the mode agrees with the experimental measurement, thus providing high confidence in the use of the developed the model.

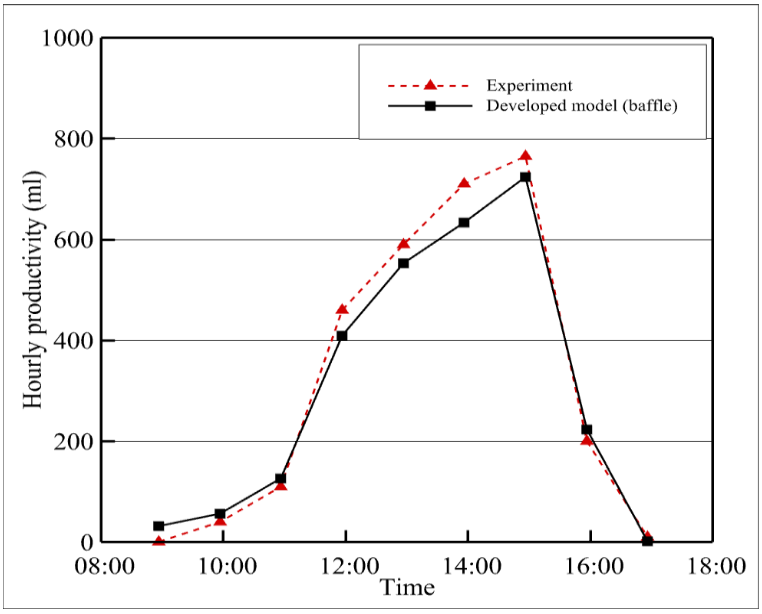

a

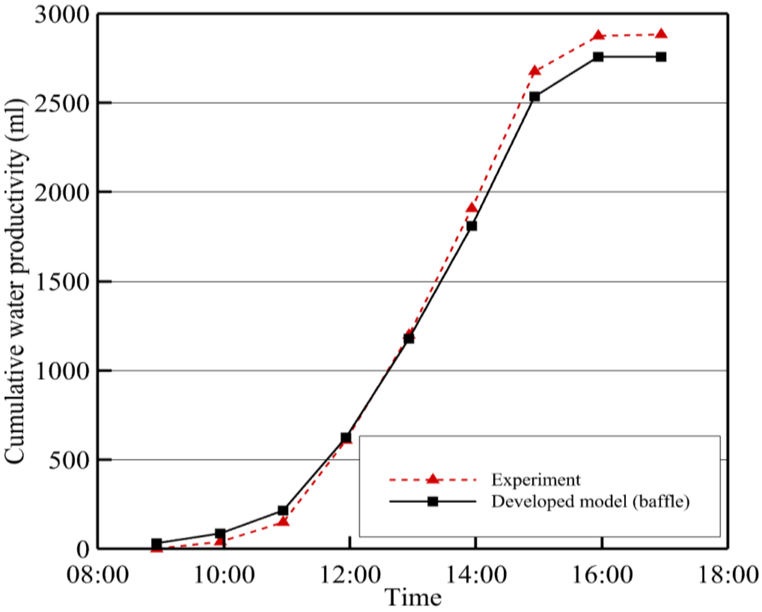

b

Figure 82: Hourly and daily cumulative water yield.

5.4. Parametric study comparison between conventional and baffle solar stills

Having validated both developed correlations, it is imperative to investigate the effect of aspect ratio, cover angle and baffle inclusion on SS solar still yield. As noted in the literature by several researchers [86, 162, 163], the SS solar still performance is directly dependent on the weather conditions, particularly the solar irradiation [24, 25].

Since the previous in-situ experiments (conventional and baffle geometry) were performed on two distinct days. It was decided to perform the parametric for both configurations under the same weather conditions for two days with the highest and lowest solar irradiation in the year. Using Meteonorm software, the hourly global solar irradiation, wind speed and ambient temperature for these days were generated for Auckland, New Zealand. Figure 83 shows the weather conditions used in this parametric study as input to the thermal mathematical model.

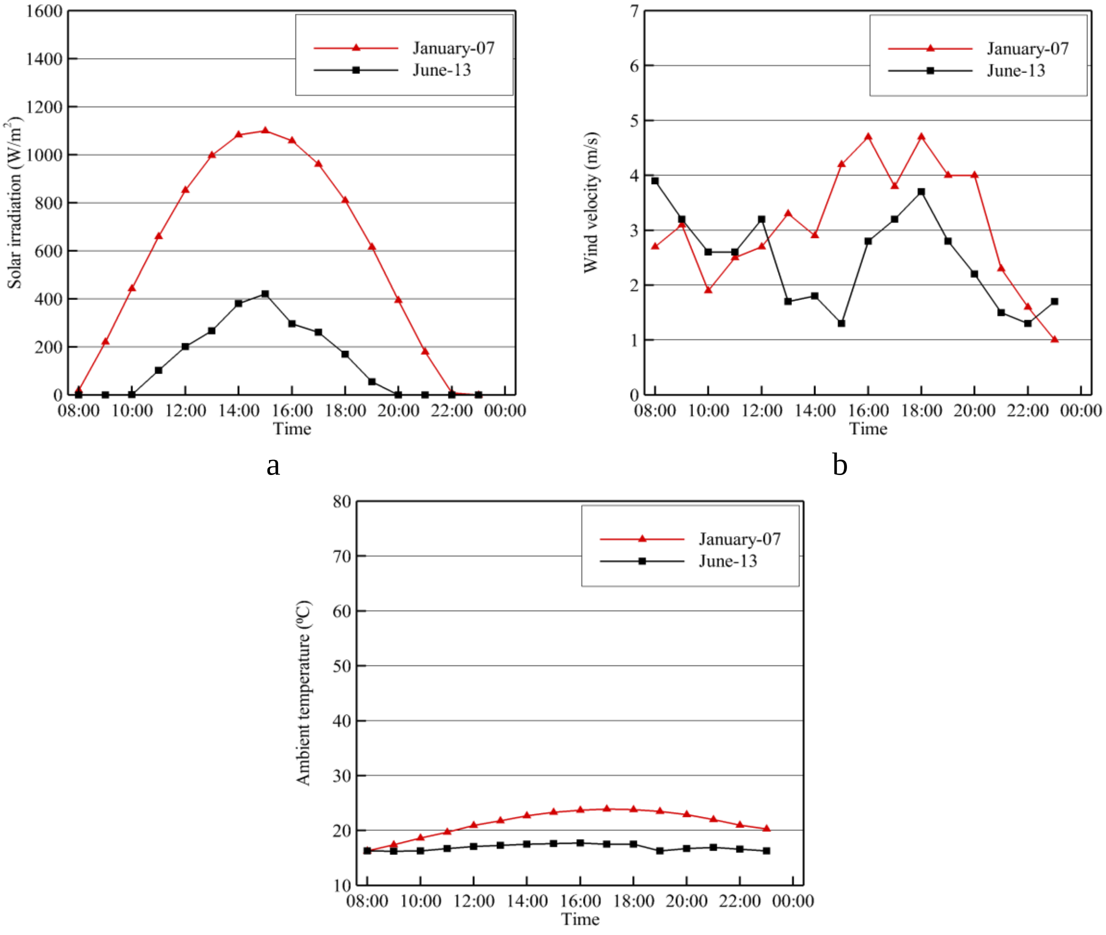

a

b

c

Figure 83: Selected days weather data, a: solar irradiation, b: wind velocity, c: ambient temperature.

Figure 84 shows the flow chart of the simulation steps undertaken to solve the mathematical model proposed for this comparative analysis. A 1 second time step was employed in this iterative scheme since no change in thermal state conditions was observed for any smaller time step. Moreover, the initial temperatures of the cover glass, absorber and water layer were assumed to be equal to the ambient air temperature data from the generated weather file. The properties of the materials used in the solar still were set to be the same to the previously designed solar still (see Chapter 2, Tables 1&2). Finally, a set of simulations of the SS solar stills (conventional and baffle) with different aspect ratios and cover angles have been performed with the only difference being the Nusselt correlation used for the evaluation of the convective heat transfer coefficient between glass cover and water surface.

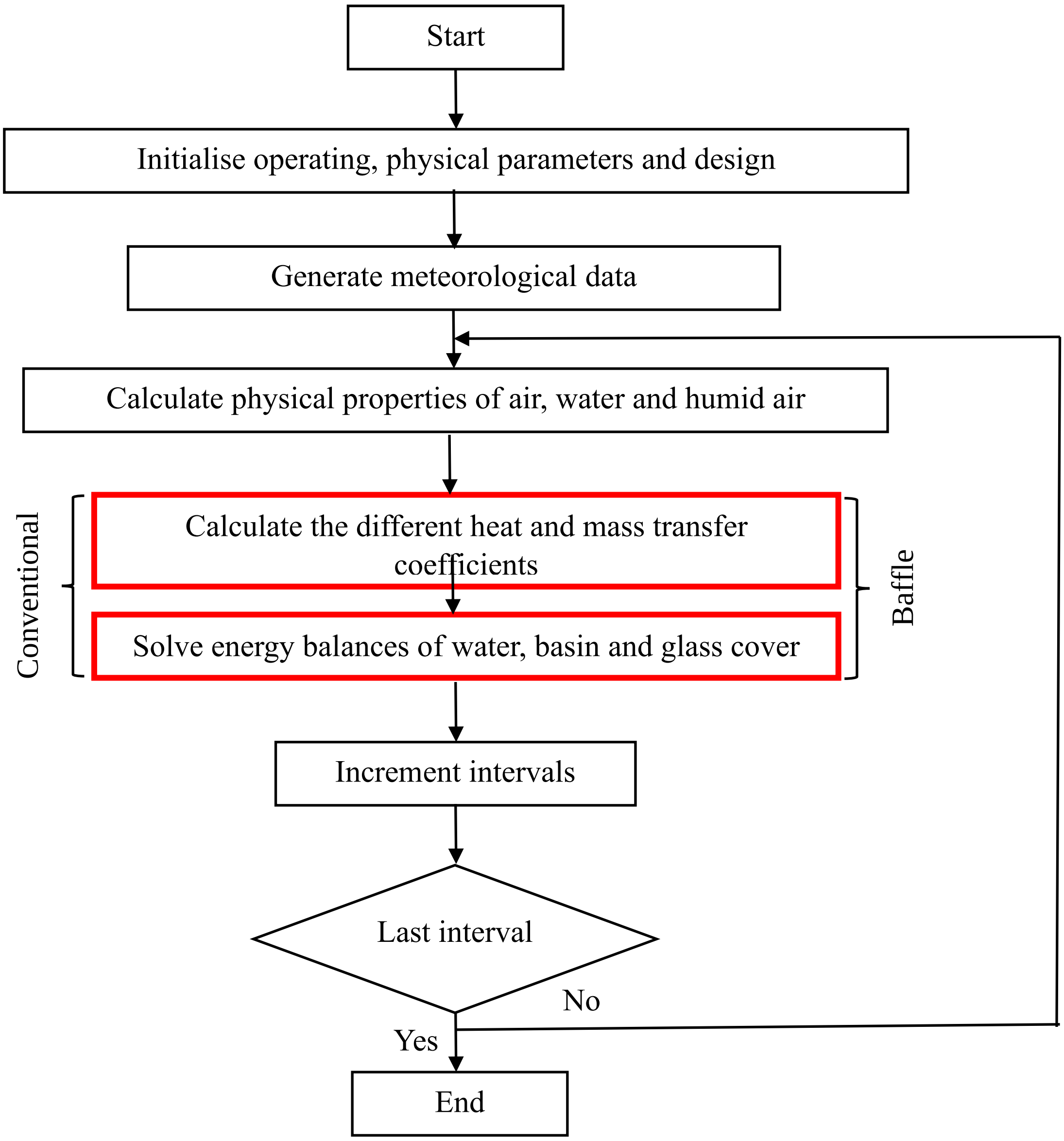

Figure 84: Flow chart for computation of yearly solar still performance.

In order to investigate the effect of varying aspect ratio and cover angle on the annual yield, the previous experimental solar still's aspect ratio (AR=2.2) and cover angle (θ=30˚) were taken as reference. For the case of the effect of cover angle, the aspect ratio was kept constant at AR=2.2 while the cover angle was varied between 10˚ to 60˚. Subsequently, the cover angle was maintained at θ=30˚ while the aspect ratio was varied between 1.5 and 3.4. The near front wall long baffle was selected as the comparison configuration as it has been determined in the previous chapter that it delivers better performance for a wider range of aspect ratios and cover angles.

5.3. Results

Figure 85 shows the daily water production from both solar stills (with and without baffle) for different angles (θ) from 10˚ to 60˚ for a constant aspect ratio (AR=2.2) during the two selected days (January and June). As expected, it can be seen from Figure 85 that water production is directly linked to the magnitude of solar irradiation, where it reaches it maximum during the month of January (high solar irradiation) and lowest during the month of June (low solar irradiation). For instance, during January, the cumulative water production for θ=10˚ cover angle was 3200 ml and 3500 ml for conventional and baffle SS solar stills respectively. However, the yield decreased considerably in June only amounting to 500 ml and 600 ml respectively. Moreover, it can also be seen from Figure 85 that the daily water production increases with increase of cover angle for both solar stills; this is due to flow inside the enclosure becoming stronger and carrying more heat from the absorber particularly near the front wall, which confirms the findings of Chapter 3. Furthermore, it is clear that the baffle improves solar still's yield by increasing the convective heat transfer coefficient, and this is due the change of the flow from monocellular to multicellular when the baffle is present.

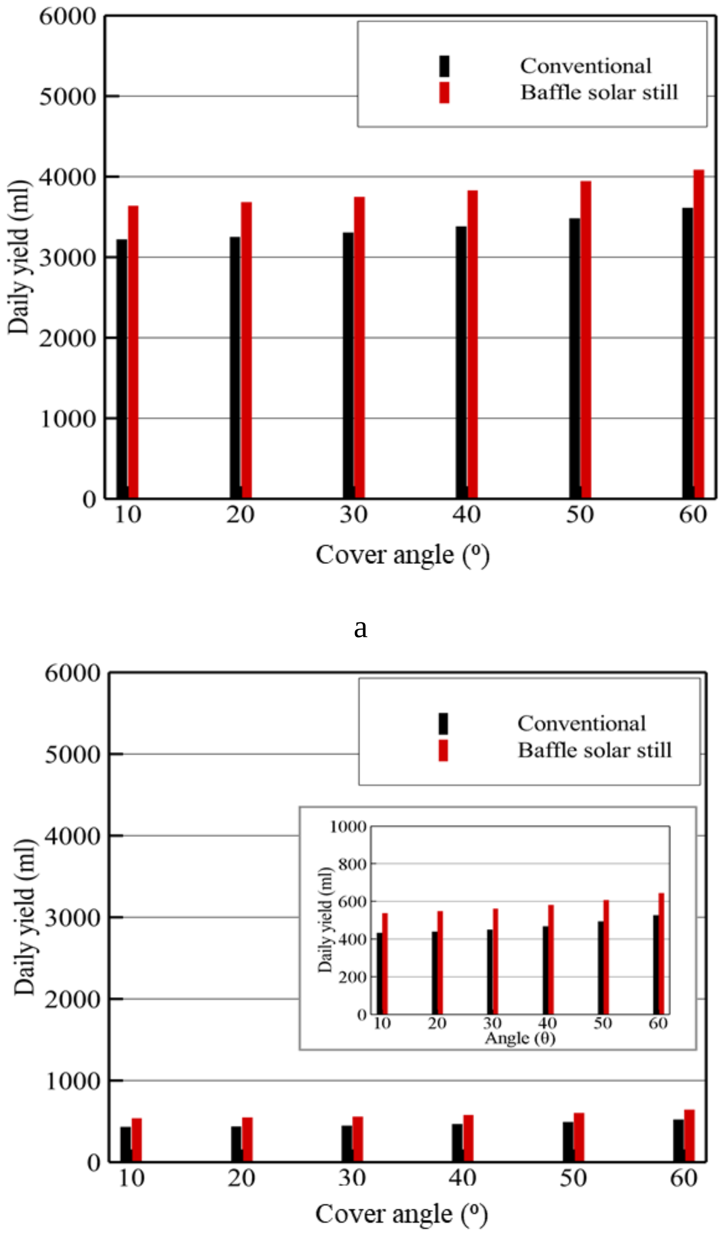

a

b

Figure 85: Effect of cover angle on the water production for constant aspect ratio (2.2), a: January, b: June.

Figure 86 shows the variation of water and glass cover temperature for both solar stills at θ=10° and AR=2.2 and it can be seen that the water temperature of the conventional solar still is higher compared to the modified solar still (baffle). This is expected as the flow in the modified geometry is composed of two cells leading to a higher convective and evaporative heat loss from the water layer compared to the conventional cavity with a monocellular flow characterised by a lower heat transfer rate.

However, the opposite is seen in glass cover temperature as, for the baffle configuration, it has a slightly higher temperature than the conventional solar still. This is due to the higher losses of heat from the water surface to the glass cover in baffle geometry due to the previously mentioned cellular flow behaviour. These observations of higher heat transfer coefficient correlations leading to lower and higher temperatures of the absorber and glass cover temperatures respectively are consistent with the findings of the results examined in Chapter 2.

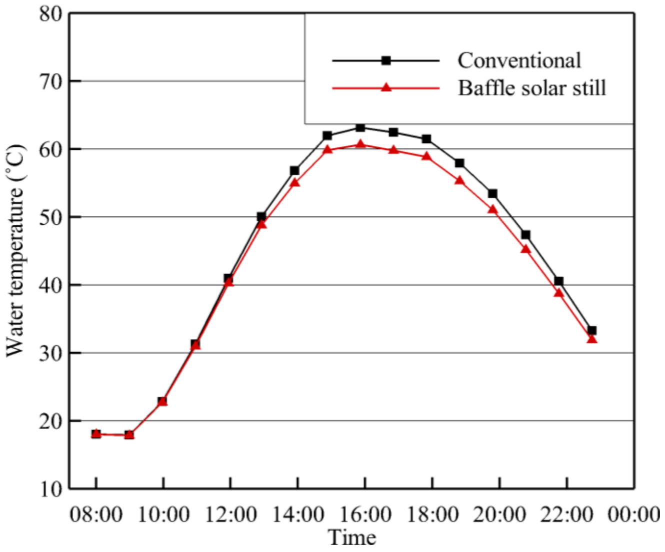

a

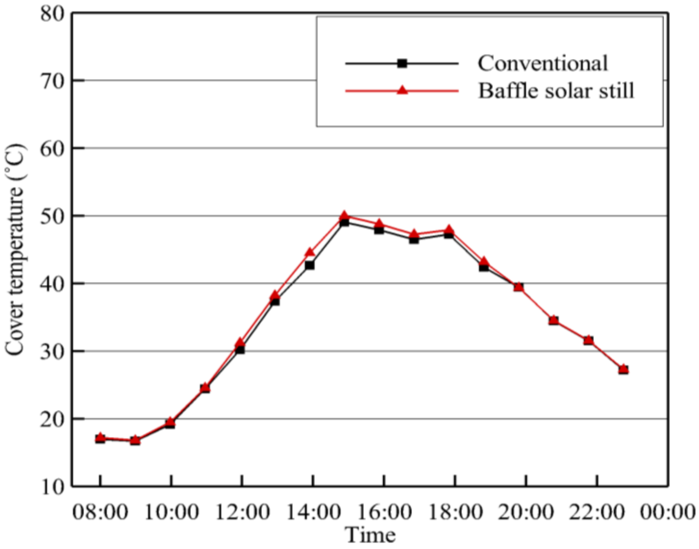

b

Figure 86 Variation of temperature for 10° convectional and baffle solar still, a: water layer, b: glass cover.

Figure 87 presents the variation of the hourly convective (a) and evaporative (b) heat transfer coefficients for both solar stills at θ=10° and AR=2.2 during January. It can be seen that the range of variation in the convective heat transfer coefficient is between 0.75 W/m^{2}K and 1.5 W/m^{2}K for baffle configuration and 1.1 W/m^{2}K to 1.9 W/m^{2}K for conventional geometry. This confirms that even though the temperature difference between the glass cover and water for baffle solar still is lower than for the conventional, the multicellular flow enhances the convective heat transfer coefficient. As a result of this change in heat transfer coefficient, it can be seen from Figure 87 (b) that the evaporative heat transfer coefficient follows the same trend but with higher magnitudes. This shows that the evaporative heat transfer coefficient is proportional to the variation in natural convection magnitude.

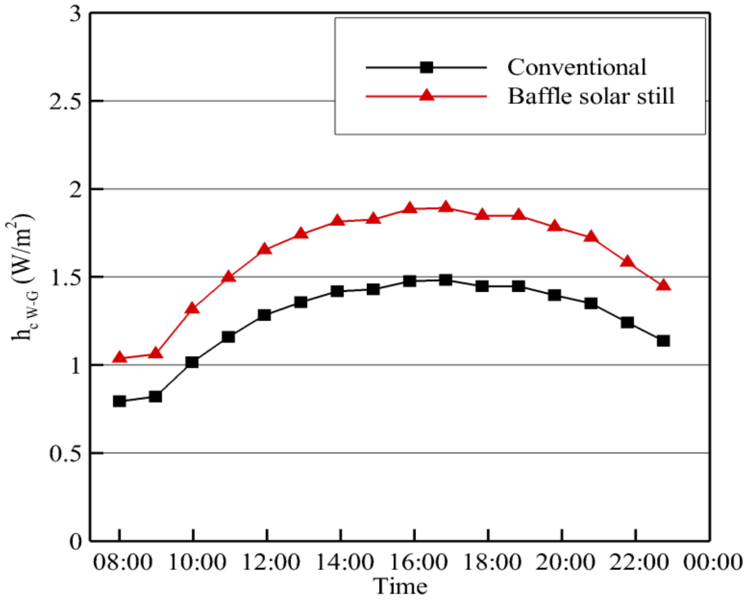

a

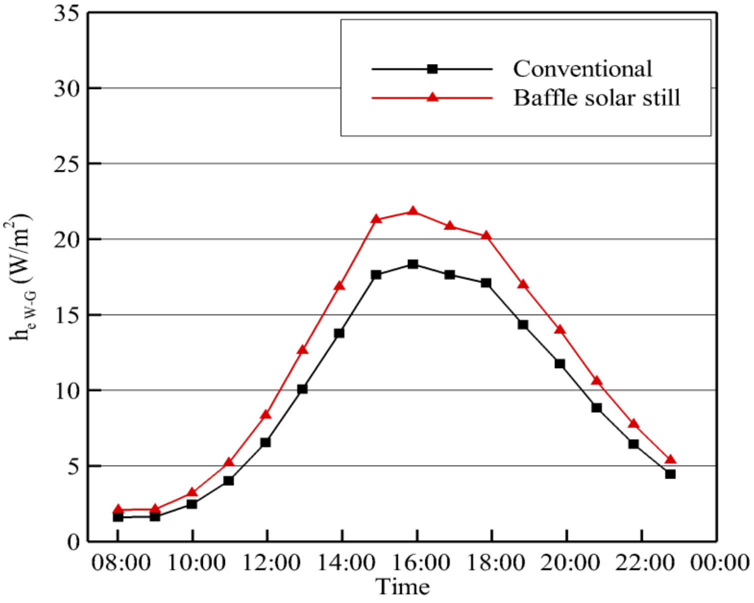

b

Figure 87: Comparison of convective heat transfer coefficient between convectional and baffle solar still with 10˚ cover angle.

Figure 88 shows the daily water production from both solar stills (with and without baffle) for different aspect ratios (AR) from 1.4 to 3.4 for a constant glass cover angle (θ =30˚) during the two selected days (January and June). For both configurations, it is observed that the yield increases with the decrease in aspect ratio, this is due to the increasing distance between the glass cover and water surface which leads to an increase in velocity magnitude of the flow inside the SS solar still resulting in a higher convective heat transfer coefficient. Consequently, this increase in convection augments the evaporative heat transfer coefficient and thus increases water productivity. These observations are commensurate with the finding of the CFD simulations performed in Chapter 3. Moreover, it is also observed from Figure 88 that baffle solar still exhibits a higher yield compared to conventional solar still, this is expected as the baffle helps to carry more heat from the water surface since the flow in latter case is composed of two cells. It is important to note that the same behaviour is encountered for both the selected days but with different magnitudes of yield.

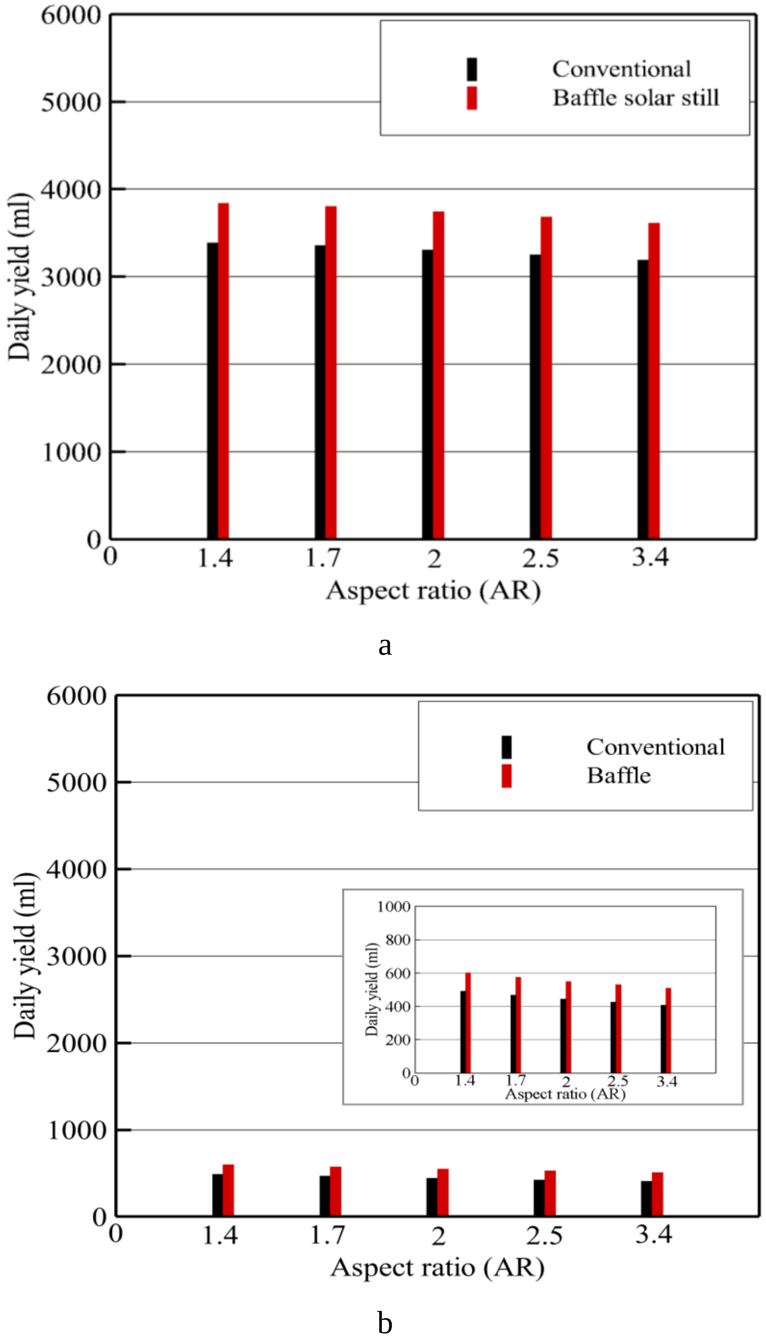

Figure 88: Effect of cover angle on the water production for constant aspect ratio (2.2), a: January, b: June.

In order to examine the effect of SS solar still geometry and configuration on the daily performance, the effect of the aspect ratio, cover angle and mounted baffle on the efficiency of SS solar still were investigated. Equation 30 was used to calculate the overall efficiency of the system:

$$Efficiency = \frac{M_{ew} * L_v}{I * t} * 100 \qquad (30)$$

Figure 89 shows the effect of the aspect ratio, cover angle and solar still configuration on the daily efficiency during a selected day in the month of January and June. It is observed that the efficiency is relatively high during the month of January compared to June; in fact, the lowest efficiency achieved in January was 21% while the highest efficiency reached in June was 19%. This is because the efficiency of solar still is directly impacted by the meteorological conditions of the selected days being greater due to the higher energy received and lower losses during the month of January; the same observation was made by Fath et al. and Madhlopa [137, 164]. Moreover, it can be observed that for both configurations and both meteorological conditions, a low aspect ratio results in higher efficiency compared to a high aspect ratio. This is expected as the convective heat transfer coefficient inside the enclosure increases with the increase in characteristic length (higher flow velocity). On the other hand, the increase in cover angle increases the efficiency of both configurations. Furthermore, baffle solar still’s efficiency is higher than that of the conventional solar still across all aspect ratios and angle for both selected days. This is expected as the baffle alters the flow pattern making it multicellular giving a stronger heat transfer.

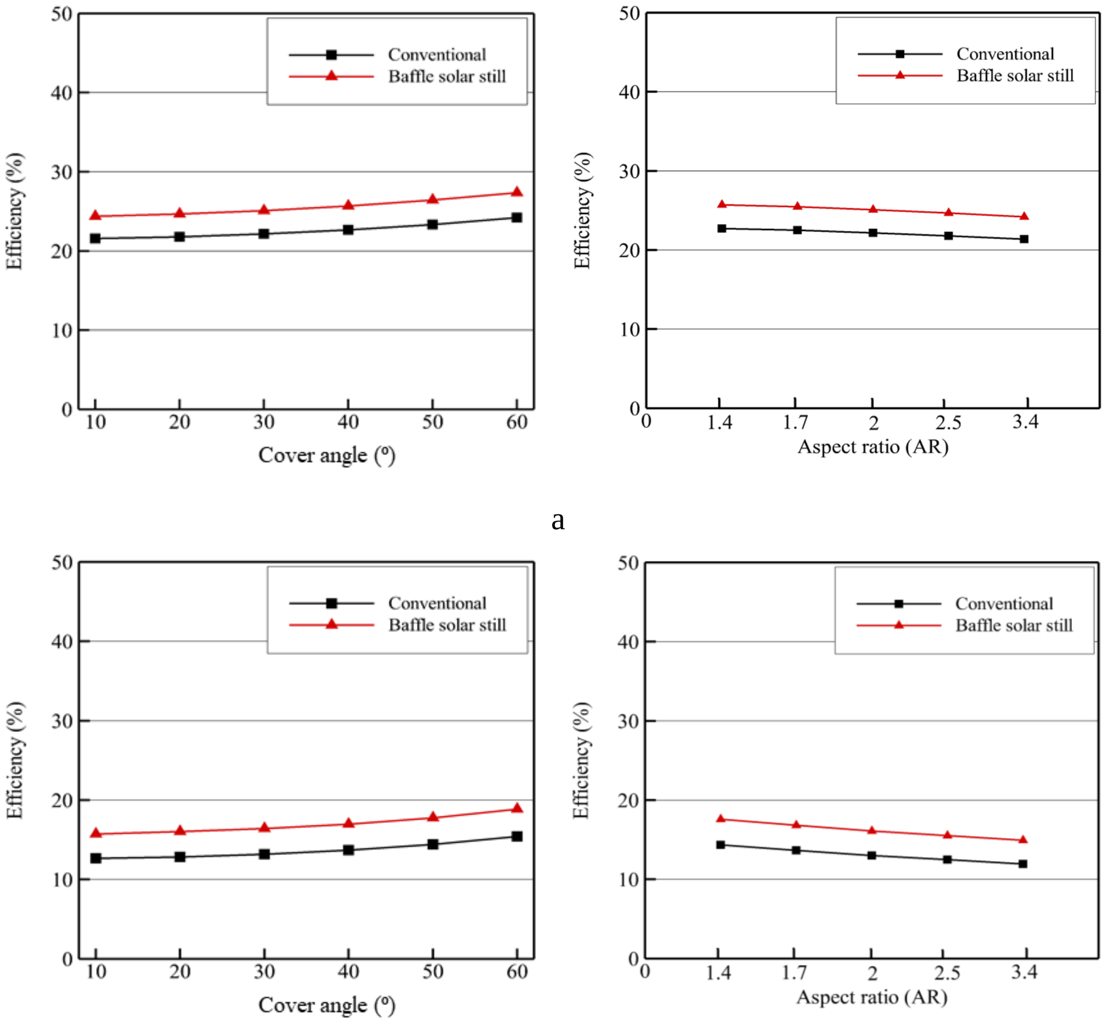

a

b

Figure 89: Daily efficiency for the selected days, a: January, b: June.

5.4. Conclusion

In this chapter, the previously developed correlations in Chapter 3 and 4 were verified against in-situ experiment. To do this, the developed mathematical model in chapter 2 was used, and the convective heat transfer coefficient from water surface was calculated using the developed correlation. For both the conventional and baffle solar still, it was found that the developed correlations predicted very well the thermal state conditions and water yield measurements of the experiment compared to previously developed correlations.

A parametric study was performed to investigate the effect of aspect ratio, cover angle and baffle attachment on the performance of SS solar still. The previously developed correlations have been used in the developed mathematical model to take into account the difference in convective heat transfer coefficient between selected configurations. In addition to the effect of the geometry, the performance of solar still is directly affected by solar irradiation, therefore, selected configurations were compared for two selected days with high and low solar irradiation.

The results of the simulation have shown that higher convective heat transfer coefficient led to higher yield. In fact, for a constant cover angle, it was found that increasing the aspect ratio for both configurations (baffle and conventional) lead to lower productivity. This is due to the decrease in distance between the absorber and glass cover leading to a lower flow velocity. However, for a constant aspect ratio, it was found that increasing the cover angle increases the productivity. This due to the fluid flow becoming stronger at greater cover angles. Moreover, across all aspect ratios and cover angles, it was found that the baffle solar still produced higher yields compared to the conventional solar still and this is due to the flow transition from monocellular in conventional solar still to multicellular in baffle configuration.

Finally, following the same trend, the efficiency of SS solar still was found to be directly impacted by the variation of convective heat transfer coefficient. It was found that the efficiency during the month of January was higher compared to June. This is simply because of the high solar irradiation leading to higher water productivity. Moreover, increasing the aspect ratio and cover angle were found to inversely impact the efficiency of both geometries (conventional and baffle). It was also found that the efficiency of baffle solar still was higher compared conventional solar still by approximatively 5%.

CHAPTER 6: CONCLUSION AND RECOMMENDATIONS

Thermal solar distillation systems driven by solar energy offer a promising solution to mitigate the increasing water demand, decreasing water accessibility and the adverse influences of conventional energy resources used to run conventional desalination systems. Knowing that natural convection in a single slope solar still is mainly driven by the temperature difference between the boundary layers and enclosure geometry, the aim of the study was to investigate the effect on natural convection inside these devices of aspect ratio and cover angle independently thereby, exploring methods to enhance their performance which potentially can significantly increase the availability of potable water in remote areas.

To achieve this, previous existing attempts to understand natural convection in these devices and developed correlations used in the thermal modelling were examined. A comprehensive literature review revealed the conflicting conclusions on the effect of aspect ratio and cover angle on the performance of solar stills. Furthermore, *in situ* experimental work was performed to investigate the validity of previously developed correlation. Results of the comparison between simulation findings and measurements have shown that the existing correlations over-predicted the performance of these devices because of their shortcomings, and this established the necessity to investigate natural convection in this type of geometries in a generalisable way.

Computational fluid dynamics (CFD) was first used to investigate the effect of aspect ratio and cover angle separately on natural convection inside the single slope enclosure. A particle image velocimetry experiment was performed to verify the accuracy of the developed numerical model. A parametric study demonstrated that both cover angle and aspect ratio affect natural convection heat transfer coefficient through the variations in the flow patterns from monocellular to multicellular. The collected data were then used to develop a new correlation that can be used to better describe the effect of both parameters on natural convection inside a single slope solar still. For further verification, the developed correlation was used to predict the yield recorded and published in the literature; results have shown good agreement between experimental work and predicted results making the correlations developed in this thesis suitable for wide range of future studies.

Having concluded that multicellular flow helps to enhance the natural convection inside the enclosure of single slope solar still, the use of a mounting baffle to separate the flow was evaluated by investigating the effect of baffle position and length within different geometries. CFD was used to investigate the effect of the baffle on natural convection magnitude from the hot absorber surface and particle image velocimetry was used to validate the results acquired from the selected numerical model. Results showed that the baffle had a remarkable effect on the flow which directly impacted and improved the convective heat transfer coefficient. However, the correct selection of baffle position and length was found to be paramount as not all cases tested were found to positively affect natural convection inside the cavity. In fact, a long baffle positioned toward the front had a wider positive impact on natural convection compared to a short baffle placed near the back wall. Subsequently a correlation equation was developed using the data acquired from simulation results.

To perform a parametric study, it was imperative to verify the validity of the developed correlations. Simulation results using the developed equations were compared to experimental measurements and better agreement was found.

Having validated the correlations in two distinct days, it was decided to perform a parametric study to evaluate the effect of aspect ratio, cover angle for both configurations (conventional and baffle solar stills) under similar weather conditions. For this Meteonorm software was used to generate weather files for two days corresponding to the highest and lowest solar irradiation in the year.

Results of the study demonstrated that the aspect ratio and cover angle directly affected the yield. Moreover, the baffle geometry outperformed the conventional still across all aspect ratios and cover angles especially during the January day where solar irradiation was high. This is due to the alteration of the flow caused by the inclusion of the baffle inside the enclosure.

In summary, this work has investigated the independent effects of varying SS solar still geometry parameters using CFD and verified by Particle Image Velocimetry. The correlations derived have also been verified by practical experimental work in the field and have also been demonstrated to better align experimental results in the published literature than the various models derived therein. Furthermore, the inclusion of a baffle in the SS solar still has also been investigated and the configuration optimised leading to an increased yield of purified water which has been demonstrated over a wide range of geometries and weather conditions. The work has practical application potential to alleviate water shortages for people in arid and remote areas.

Recommendations

Over and above the knowledge delivered in this research, there is certainly a need for more work to be done in the future. In particular, investigating and comparing the variation in natural convection in other existing solar still designs such as double slope, pyramid and hemispherical against results found in this work. Extensive research is available in the literature regarding water production comparison between the existing solar still designs. However, no research has demonstrated the way in which some geometries’ performance surpass others. Therefore, it is with great importance to numerically investigate the effect of various solar still shapes on natural convection and flow behaviours inside solar stills.

There is also a need to further investigate natural convection inside modified solar still by studying the effect of abrupt heating of the bottom surface (absorber) on flow inside the enclosure. This could be important due to the intermittent nature of solar irradiation that directly affect the temperature of water layer alongside the absorber surface. On this basis, further investigation of natural convection could possibly be important as it will aid in optimising further the placement and the length of baffle that should be used to attain higher performance.

Lastly, although the current study demonstrated that incorporating a baffle attached to the cover glass can increase the productivity of SS solar still. It is important to investigate the effect of baffle material properties (transmittance, thermal conductivity, heat capacity etc.) on the performance of modified solar still. This is important as it will give a clear understanding on the material selection in order to get the best of the baffle effect on flow separation. Furthermore, it would be beneficial to investigate and compare in a generalizable way using Artificial Neural Network (ANN) optimization techniques the cost of water produced from both modified and conventional solar still. Finally, coupled with the findings of this research, studying the effect of material properties and cost will have the potential to provide a better understanding of the economic feasibility of modified SS solar still to tackle water scarcity in remote areas.

References

1. Dunkle, R. Solar water distillation: the roof type still and a multiple effect diffusion still. in Proc. International Heat Transfer Conference, University of Colorado, USA. 1961.

2. Dormido, H. These countries are the most at risk from a water crisis. 2019; Available from: https://www.bloomberg.com/graphics/2019-countries-facing-water-crisis/.

3. Alkaisi, A., R. Mossad, and A. Sharifian-Barforoush, A Review of the water desalination systems integrated with renewable energy. Energy Procedia, 2017. 110: p. 268-274.

4. Gude, V.G., Desalination and water reuse to address global water scarcity. Reviews in Environmental Science and Bio/Technology, 2017. 16(4): p. 591-609.

5. Connor, R., The United Nations world water development report 2015: water for a sustainable world. Vol. 1. 2015: UNESCO publishing.

6. Van Rensburg, P., Overcoming global water reuse barriers: the Windhoek experience. International Journal of Water Resources Development, 2016. 32(4): p. 622-636.

7. Zheng, H., Solar Energy Desalination Technology. 2017: Elsevier.

8. Belessiotis, V., S. Kalogirou, and E. Delyannis, Thermal solar desalination: methods and systems. 2016: Elsevier.

9. Qasim, M., M. Bdrelzaman, N. Darwish, N. Darwish and N. Hilal, Reverse osmosis desalination: A state-of-the-art review. Desalination, 2019. 459: p. 59-104.

10. Hansima, M., M. Makehelwala, K. Jinadasa, Y. Wei and k. Nanayakkara, A. Herath, R. Weerasooriya, Fouling of ion exchange membranes used in the electrodialysis reversal advanced water treatment: A review. Chemosphere, 2020: p. 127951.

11. Park, K., Y. H. Jang, M. Kim, D. Yang and S. Hong, Comprehensive analysis of a hybrid FO/crystallization/RO process for improving its economic feasibility to seawater desalination. Water research, 2020. 171: p. 115426.

12. Georgiou, M.C., A.M. Bonanos, and J.G. Georgiadis. Evaluation of a multiple-effect distillation unit under partial load operating conditions. in Conference Papers in Science. 2013. 1-11.

13. Zhao, J., M. Wang, H. Lababidi, H. Al-Adwani and K. Gleason, A review of heterogeneous nucleation of calcium carbonate and control strategies for scale formation in multi-stage flash (MSF) desalination plants. Desalination, 2018. 442: p. 75-88.

14. Kasaeian, A., S. Babaei, M. Jahanpanah, H. Sarrafha, A. Alsagri, S. Ghaffarian and W Yan, Solar humidification-dehumidification desalination systems: a critical review. Energy Conversion and Management, 2019. 201: p. 112129.

15. Muftah, A.F., M. A. Alghoul, A. Fudholi, M. M. Abdul-Majeed and K. Sopian, Factors affecting basin type solar still productivity: A detailed review. Renewable and Sustainable Energy Reviews, 2014. 32: p. 430-447.

16. Dumka, P. and D.R. Mishra, Influence of salt concentration on the performance characteristics of passive solar still. International Journal of Ambient Energy, 2019: p. 1-11.

17. Shirsath, G.B., R. Ganesh, S. Pala and K. Muralidhar, Effect of salinity and water depth on the performance of doubly inclined solar still. Desalination and Water Treatment, 2018. 124: p. 72-87.

18. Muftah, A.F., M. A. Alghoul, A. Fudholi, M. M. Abdul-Majeed and K. Sopian, Factors affecting basin type solar still productivity: A detailed review. Renewable and Sustainable Energy Reviews, 2014. 32: p. 430-447.

19. Sarkar, M.N.I., A. Sifat, S.M. Reza and M. Sadique, A review of optimum parameter values of a passive solar still and a design for southern Bangladesh. Renewables: Wind, Water, and Solar, 2017. 4(1): p. 1-13.

20. Thakur, A.K., M.P. Vikrama, and S. Christopher, Augmented yield productivity of solar still using energy storage materials: Experimental investigation under the climatic conditions of Rajasthan, in Advances in Greener Energy Technologies. 2020, Springer. p. 817-831.

21. Rajvanshi, A.K., Effect of various dyes on solar distillation. Solar energy, 1981. 27(1): p. 51-65.

22. Faridani, Z.H. and A. Ameri, Performance enhancement of a basin solar still using γ-Al 2 O 3 nanoparticles and a mixer: an experimental approach. Journal of Thermal Analysis and Calorimetry, 2021: p. 1-13.

23. Omara, A.A., A. Abuelnuor, H. A. Mohammed and M. Khiadani, Phase change materials (PCMs) for improving solar still productivity: a review. Journal of Thermal Analysis and Calorimetry, 2020. 139(3): p. 1585-1617.

24. Keshtkar, M., M. Eslami, and K. Jafarpur, Effect of design parameters on performance of passive basin solar stills considering instantaneous ambient conditions: A transient CFD modeling. Solar Energy, 2020. 201: p. 884-907.

25. Tiwari, A.K. and G.N. Tiwari, Effect of water depths on heat and mass transfer in a passive solar still: in summer climatic condition. Desalination, 2006. 195(1): p. 78-94.

26. Nafey, A.S., M. Abdelkader, A. Abdelmotalip and A.A. Mabrouk, Parameters affecting solar still productivity. Energy conversion and management, 2000. 41(16): p. 1797-1809.

27. Al-Hinai, H., M.S. Al-Nassri, and B.A. Jubran, Effect of climatic, design and operational parameters on the yield of a simple solar still. Energy Conversion and Management, 2002. 43(13): p. 1639-1650.

28. Dsilva Winfred Rufuss, D., S. Iniyan, L. Suganthi and P. Davies, Solar stills: A comprehensive review of designs, performance and material advances. Vol. 63. 2016. 464-496.

29. Naveen Kumar, P., D. G. Harris Samuel, P. K. Nagarajan and R. Sathyamurthy, Theoretical analysis of a triangular pyramid solar still integrated to an inclined solar still with baffles. International Journal of Ambient Energy, 2017. 38(7): p. 694-700.

30. Mahian, O., A. Kianifar, S. Heris, D. Wen, A. Z. Sahin and S. Wongwises, Nanofluids effects on the evaporation rate in a solar still equipped with a heat exchanger. Nano Energy, 2017. 36: p. 134-155.

31. Arunkumar, T., A.E. Kabeel, K. Raj, D. Denkenberger, R. Sathyamurthy, P. Ragupathy and R. Velraj, Productivity enhancement of solar still by using porous absorber with bubble-wrap insulation. Journal of Cleaner Production, 2018. 195: p. 1149-1161.

32. Panchal, H., P. Prathik, P. Nikunj and T. Hemin, Performance analysis of solar still with different energy-absorbing materials. International Journal of Ambient Energy, 2017. 38(3): p. 224-228.

33. Yousef, M.S. and H. Hassan, An experimental work on the performance of single slope solar still incorporated with latent heat storage system in hot climate conditions. Journal of cleaner production, 2019. 209: p. 1396-1410.

34. Sakthivel, T. and T. Arjunan, Thermodynamic performance comparison of single slope solar stills with and without cotton cloth energy storage medium. Journal of Thermal Analysis and Calorimetry, 2019. 137(1): p. 351-360.

35. Hassan, H., M.S. Yousef, M. Fathy and M. Ahmed, Impact of condenser heat transfer on energy and exergy performance of active single slope solar still under hot climate conditions. Solar Energy, 2020. 204: p. 79-89.

36. Al-Hamadani, A.A. and S. Shukla, Performance of single slope solar still with solar protected condenser. Distributed Generation & Alternative Energy Journal, 2013. 28(2): p. 6-28.

37. El-Sebaii, A.A. and M. El-Naggar, Year round performance and cost analysis of a finned single basin solar still. Applied Thermal Engineering, 2017. 110: p. 787-794.

38. El-Sebaii, A.A., M. R. I. Ramadan, S. Aboul-Enein and M. El-Naggar, Effect of fin configuration parameters on single basin solar still performance. Desalination, 2015. 365: p. 15-24.

39. Subhani, S. and R.S. Kumar. Numerical investigation on influence of mounting baffles in solar stills. in AIP Conference Proceedings. 2019. AIP Publishing LLC.

40. El-Sebaii, A.A., S. Aboul-Enein, and E. El-Bialy, Single basin solar still with baffle suspended absorber. Energy Conversion and Management, 2000. 41(7): p. 661-675.

41. Karimi Estahbanati, M.R., A. Ahsan, M. Feilizadeh, K. Jafarpur, S. Ashrafmansouri and M. Feilizadeh, Theoretical and experimental investigation on internal reflectors in a single-slope solar still. Applied Energy, 2016. 165: p. 537-547.

42. Tanaka, H., Experimental study of a basin type solar still with internal and external reflectors in winter. Desalination, 2009. 249(1): p. 130-134.

43. Cherraye, R., B. Bouchekima, D. Bekhchi, H. Bouguetaya and A. Khechekhouche, The effect of tilt angle on solar still productivity at different seasons in arid conditions (south Algeria). International Journal of Ambient Energy, 2020: p. 1-7.

44. Azooz, A. and G. Younis, Effect of glass inclination angle on solar still performance. Journal of Renewable and Sustainable Energy, 2016. 8(3): p. 033702.

45. Dev, R. and G.N. Tiwari, Characteristic equation of a passive solar still. Desalination, 2009. 245(1): p. 246-265.

46. Panchal, H.N. and S. Patel, An extensive review on different design and climatic parameters to increase distillate output of solar still. Renewable and Sustainable Energy Reviews, 2017. 69: p. 750-758.

47. Sharshir, S. W., N. Yang, G. Peng, and A. E. Kabeel, Factors affecting solar stills productivity and improvement techniques: A detailed review. Applied Thermal Engineering, 2016. 100: p. 267-284.

48. Jamil, B. and N. Akhtar, Effect of specific height on the performance of a single slope solar still: An experimental study. Desalination, 2017. 414: p. 73-88.

49. Rahbar, N. and J.A. Esfahani, Estimation of convective heat transfer coefficient in a single-slope solar still: a numerical study. Desalination and Water Treatment, 2012. 50(1-3): p. 387-396.

50. Tsilingiris, P.T., The influence of binary mixture thermophysical properties in the analysis of heat and mass transfer processes in solar distillation systems. Solar Energy, 2007. 81(12): p. 1482-1491.

51. Omri, A., J. Orfi, and S.B. Nasrallah, Natural convection effects in solar stills. Desalination, 2005. 183(1): p. 173-178.

52. Shawaqfeh, A.T. and M.M. Farid, New development in the theory of heat and mass transfer in solar stills. Solar Energy, 1995. 55(6): p. 527-535.

53. Adhikari, R.S., A. Kumar, and A. Kumar, Estimation of mass-transfer rates in solar stills. International Journal of Energy Research, 1990. 14(7): p. 737-744.

54. Cooper, P.I., The maximum efficiency of single-effect solar stills. Solar Energy, 1973. 15(3): p. 205-217.

55. Jacob, M., Heat transfer. John Wiley & Sons, 1949. 1: p. 655.

56. Mull, W. and H. Reiher, Gesundh.-Ing. 1930, Beihefte.

57. Rubio, E., J.L. Fernández-Zayas, and M.A. Porta-Gándara, Current status of theoretical and practical research of seawater single-effect passive solar distillation in Mexico. Journal of Marine Science and Engineering, 2020. 8(2): p. 94.

58. Porta-Gándara, M., J. Fernández-Zayas, and N. Chargoy-del-Valle, Solar still distillation enhancement through water surface perturbation. Solar Energy, 2020. 196: p. 312-318.

59. Muñoz, F., E. Barrera, A. Ruiz, E.M. Martínez and N. Chargoy, Long-term experimental theoretical study on several single-basin solar stills. Desalination, 2020. 476: p. 114241.

60. Khan, M.Z., E.H. Khan, N. Agarhari, M. A. Wahid and I. Nawaz, Calculation for the output of solar still of an individual hour, in advances in materials engineering and manufacturing processes. 2020, Springer. p. 117-130.

61. Hedayatizadeh, M., F. Sarhaddi, and A. Pugsley, A detailed thermal modeling of a passive single-slope solar still with improved accuracy. Groundwater for Sustainable Development, 2020: p. 100384.

62. El-Sebaii, A. and A.E.M. Khallaf, Mathematical modeling and experimental validation for square pyramid solar still. Environmental Science and Pollution Research, 2020: p. 1-13.

63. Dumka, P. and D.R. Mishra, Performance evaluation of single slope solar still augmented with the ultrasonic fogger. Energy, 2020. 190: p. 116398.

64. Agrawal, A. and R. Rana, Theoretical and experimental performance evaluation of single-slope single-basin solar still with multiple V-shaped floating wicks. Heliyon, 2019. 5(4): p. e01525.

65. Sivakumar, V., E.G. Sundaram, and M. Sakthivel, Investigation on the effects of heat capacity on the theoretical analysis of single slope passive solar still. Desalination and Water Treatment, 2016. 57(20): p. 9190-9202.

66. El-Sebaii, A. and M. Al-Dossari, A mathematical model of single basin solar still with an external reflector. Desalination and water treatment, 2011. 26(1-3): p. 250-259.

67. Feilizadeh, M., M. Soltanieh, K. Jafarpur and M. K. Estahbanati, A new radiation model for a single-slope solar still. Desalination, 2010. 262(1-3): p. 166-173.

68. Shukla, S. and V. Sorayan, Thermal modeling of solar stills: an experimental validation. Renewable Energy, 2005. 30(5): p. 683-699.

69. Fath, H.E. and S.M. Elsherbiny, Effect of adding a passive condenser on solar still performance. International journal of solar energy, 1992. 11(1-2): p. 73-89.

70. Yilmaz, T.P. and H.S. Aybar. Evaluation of the correlations for predicting evaporative loss from water body. 1999. United States: American Society of Heating, Refrigerating and Air-Conditioning Engineers, Inc., Atlanta, GA (US).

71. Hongfei, Z., Z. Xiaoyan, Z. Jing and W. Yuyuan, A group of improved heat and mass transfer correlations in solar stills. Energy Conversion and Management, 2002. 43(18): p. 2469-2478.

72. Rahbar, N. and J.A. Esfahani, Productivity estimation of a single-slope solar still: Theoretical and numerical analysis. Energy, 2013. 49: p. 289-297.

73. Tiwari, G.N., A. Minocha, P. B. Sharma and M. E. Khan, Simulation of convective mass transfer in a solar distillation process. Energy Conversion and Management, 1997. 38(8): p. 761-770.

74. Clark, J.A., The steady-state performance of a solar still. Solar Energy, 1990. 44(1): p. 43-49.

75. Kumar, S. and G.N. Tiwari, Estimation of convective mass transfer in solar distillation systems. Solar Energy, 1996. 57(6): p. 459-464.

76. Singh, R.G. and G. Tiwari, Simulation performance of single slope solar still by using iteration method for convective heat transfer coefficient. Groundwater for Sustainable Development, 2020. 10: p. 100287.

77. Dwivedi, V.K. and G.N. Tiwari, Comparison of internal heat transfer coefficients in passive solar stills by different thermal models: An experimental validation. Desalination, 2009. 246(1): p. 304-318.

78. Tiwari, G.N. and L. Sahota, General introduction, in advanced solar-distillation systems: basic principles, thermal modeling, and its application, G.N. Tiwari and L. Sahota, Editors. 2017, Springer Singapore: Singapore. p. 1-62.

79. Tiwari, A.K. and G.N. Tiwari, Effect of cover inclination and water depth on performance of a solar still for indian climatic conditions. Journal of Solar Energy Engineering, 2008. 130(2): p. 024502-024502-4.

80. Aggarwal, S. and G.N. Tiwari, Convective mass transfer in a double-condensing chamber and a conventional solar still. Desalination, 1998. 115(2): p. 181-188.

81. Eltawil, M.A. and Z.M. Omara, Enhancing the solar still performance using solar photovoltaic, flat plate collector and hot air. Desalination, 2014. 349: p. 1-9.

82. Khechekhouche, A., B. Benhaoua, M. Manokar, R. Sathyamurthy, A. E. Kabeel and Z. Driss, Sand dunes effect on the productivity of a single slope solar distiller. Heat and Mass Transfer, 2020. 56(4): p. 1117-1126.

83. Manoj Kumar, D. Sudarvizhi, K.B. Prakash and A.M. Anupradeepa, Investigating a single slope solar still with a nano-phase change material. Materials Today: Proceedings, 2021.

84. Sandeep, S. Kumar, and V.K. Dwivedi, Experimental study on modified single slope single basin active solar still. Desalination, 2015. 367: p. 69-75.

85. Shanmugan, S., B. Janarthanan, and J. Chandrasekaran, Performance of single-slope single-basin solar still with sensible heat storage materials. Desalination and Water Treatment, 2012. 41(1-3): p. 195-203.

86. Singh, D.B., Improving the performance of single slope solar still by including N identical PVT collectors. Applied Thermal Engineering, 2018. 131: p. 167-179.

87. Nazari, S., H. Safarzadeh, and M. Bahiraei, Experimental and analytical investigations of productivity, energy and exergy efficiency of a single slope solar still enhanced with thermoelectric channel and nanofluid. Renewable energy, 2019. 135: p. 729-744.

88. Bhargva, M. and A. Yadav, Productivity augmentation of single-slope solar still using evacuated tubes, heat exchanger, internal reflectors and external condenser. Energy Sources, Part A: Recovery, Utilization, and Environmental Effects, 2019: p. 1-21.

89. Dev, R. and G. Tiwari, Characteristic equation of a passive solar still. Desalination, 2009. 245(1-3): p. 246-265.

90. Elango, T., A. Kannan, and K.K. Murugavel, Performance study on single basin single slope solar still with different water nanofluids. Desalination, 2015. 360: p. 45-51.

91. Aboul-Enein, S., A. El-Sebaii, and E. El-Bialy, Investigation of a single-basin solar still with deep basins. Renewable Energy, 1998. 14(1-4): p. 299-305.

92. Akash, B.A., M.S. Mohsen, and W. Nayfeh, Experimental study of the basin type solar still under local climate conditions. Energy Conversion and Management, 2000. 41(9): p. 883-890.

93. Sathish, D., M. Veeramanikandan, and R. Tamilselvan, Design and fabrication of single slope solar still using metal matrix structure as energy storage. Materials Today: Proceedings, 2020. 27: p. 1-5.

94. Kalidasa Murugavel, K., K.S. Chockalingam, and K. Srithar, Progresses in improving the effectiveness of the single basin passive solar still. Desalination, 2008. 220(1): p. 677-686.

95. Ali Samee, M., K.M. Umar, M. Tariq, and A. Nasir, Design and performance of a simple single basin solar still. Renewable and Sustainable Energy Reviews, 2007. 11(3): p. 543-549.

96. Sharon, H., K. S. Reddy, D. Krithika and L. Philip, Experimental performance investigation of tilted solar still with basin and wick for distillate quality and enviro-economic aspects. Desalination, 2017. 410: p. 30-54.

97. Agrawal, A., R.S. Rana, and P.K. Srivastava, Heat transfer coefficients and productivity of a single slope single basin solar still in Indian climatic condition: Experimental and theoretical comparison. Resource-Efficient Technologies, 2017. 3(4): p. 466-482.

98. Kumar Nougriaya, S., M. K. Chopra, B. Gupta and P. Baredar, Stepped solar still: A review on designs analysis. Materials Today: Proceedings, 2020.

99. Rehman, N.u., Optical-irradiance ray-tracing model for the performance analysis and optimization of a single slope solar still. Desalination, 2019. 457: p. 22-31.

100. Khalifa, A.J.N., On the effect of cover tilt angle of the simple solar still on its productivity in different seasons and latitudes. Energy Conversion and Management, 2011. 52(1): p. 431-436.

101. Tiwari, G., J. Thomas, and E. Khan, Optimisation of glass cover inclination for maximum yield in a solar still. Heat Recovery Systems and CHP, 1994. 14(4): p. 447-455.

102. Jahanpanah, M., Experimental investigation of the effects of low-temperature phase change material on single-slope solar still. Desalination, 2021. 499: p. 114799.

103. Zanganeh, P., S. G. Ataallah, A. Shahab and F. Mehrzad, Nano-coated condensation surfaces enhanced the productivity of the single-slope solar still by changing the condensation mechanism. Journal of Cleaner Production, 2020. 265: p. 121758.

104. Madiouli, J., A. Lahsin, I. Shigidi, I.A. Badruddin and A. Kessentini, Experimental study and evaluation of single slope solar still combined with flat plate collector, parabolic trough and packed bed. Solar Energy, 2020. 196: p. 358-366.

105. Dhivagar, R., M. Mohanraj, K. Hidouri and Y. Belyayev, Energy, exergy, economic and enviro-economic (4E) analysis of gravel coarse aggregate sensible heat storage-assisted single-slope solar still. Journal of Thermal Analysis and Calorimetry, 2020: p. 1-20.

106. Balachandran, G.B. P. W. David, P. V. Chellam, M. N. A. Ali, V. Radhakrishnan, R. Balamurugan and A. M. Manokar, Rehash of cooked oil for the palatable water production using single slope solar still. Fuel, 2020. 271: p. 117613.

107. Nazari, S., H. Safarzadeh, and M. Bahiraei, Performance improvement of a single slope solar still by employing thermoelectric cooling channel and copper oxide nanofluid: an experimental study. Journal of Cleaner Production, 2019. 208: p. 1041-1052.

108. Mu, L, Enhancing the performance of a single-basin single-slope solar still by using Fresnel lens: Experimental study. Journal of cleaner production, 2019. 239: p. 118094.

109. Singh, D., Energy metrics analysis of N identical evacuated tubular collectors integrated single slope solar still. Energy, 2018. 148: p. 546-560.

110. Kumar, R.A., G. Esakkimuthu, and K.K. Murugavel, Performance enhancement of a single basin single slope solar still using agitation effect and external condenser. Desalination, 2016. 399: p. 198-202.

111. Estahbanati, M.K., A. Ahsan, M. Feilizadeh, K. Jafarpur, S. Ashrafmansouri and M. Feilizadeh, et al., Theoretical and experimental investigation on internal reflectors in a single-slope solar still. Applied energy, 2016. 165: p. 537-547.

112. Rajamanickam, M. and A. Ragupathy, Influence of water depth on internal heat and mass transfer in a double slope solar still. Energy procedia, 2012. 14: p. 1701-1708.

113. Panchal, H.N. and K. Pravin, Experimental investigation on coupling evacuated heat pipe collector on single basin single slope solar still productivity. International Journal of Mechanical Engineering & Technology, 2011. 2(1): p. 1-9.

114. Kumar, S. and G. Tiwari, Life cycle cost analysis of single slope hybrid (PV/T) active solar still. Applied energy, 2009. 86(10): p. 1995-2004.

115. Abdallah, S., O. Badran, and M.M. Abu-Khader, Performance evaluation of a modified design of a single slope solar still. Desalination, 2008. 219(1-3): p. 222-230.

116. Tiwari, A.K. and G. Tiwari, Thermal modeling based on solar fraction and experimental study of the annual and seasonal performance of a single slope passive solar still: the effect of water depths. Desalination, 2007. 207(1-3): p. 184-204.

117. Samee, M.A., U. K. Mirza, T. Majeed and N. Ahmad, Design and performance of a simple single basin solar still. Renewable and Sustainable Energy Reviews, 2007. 11(3): p. 543-549.

118. Badran, O.O., Experimental study of the enhancement parameters on a single slope solar still productivity. Desalination, 2007. 209(1-3): p. 136-143.

119. Meukam, P., D. Njomo, D. Gbane and S. Toure, Experimental optimization of a solar still: application to alcohol distillation. Chemical Engineering and Processing: Process Intensification, 2004. 43(12): p. 1569-1577.

120. Fath, H.E., M. El-Samanoudy, K. Fahmy and A. Hassabou, Thermal-economic analysis and comparison between pyramid-shaped and single-slope solar still configurations. Desalination, 2003. 159(1): p. 69-79.

121. Bahadori, M.N. and F.E. Edlin, Improvement of solar stills by the surface treatment of the glass. Solar Energy, 1973. 14(3): p. 339-352.

122. Baibutaev, K. and B. Achilov, Comparative testing of a solar distiller. Appl. Solar Energy (USSR) (Engl. Transl.) (United States), 1968. 4(5).

123. Shanmugan, S. and F. Essa, Experimental study on single slope single basin solar still using TiO2 nano layer for natural clean water invention. Journal of Energy Storage, 2020. 30: p. 101522.

124. Dumka, P. and D. Mishra, Performance evaluation of single slope solar still augmented with sand-filled cotton bags. Journal of Energy Storage, 2019. 25: p. 100888.

125. Dumka, P., Y. Kushwah, A. Sharma and D.R. Sharma, Comparative analysis and experimental evaluation of single slope solar still augmented with permanent magnets and conventional solar still. Desalination, 2019. 459: p. 34-45.

126. Joshi, P. and G. Tiwari, Energy matrices, exergo-economic and enviro-economic analysis of an active single slope solar still integrated with a heat exchanger: A comparative study. Desalination, 2018. 443: p. 85-98.

127. Rabhi, K., F. Nasri, C. Ali and H.B. Bacha, Experimental performance analysis of a modified single-basin single-slope solar still with pin fins absorber and condenser. Desalination, 2017. 416: p. 86-93.

128. Somanchi, N.S., S. Sagi, T.A. Kumar and S.K. Lakarmuludi, Modelling and analysis of single slope solar still at different water depth. Aquatic procedia, 2015. 4: p. 1477-1482.

129. Madhlopa, A. and C. Johnstone, Model for computation of solar fraction in a single-slope solar still. Solar Energy, 2009. 83(6): p. 873-882.

130. Badran, O. and H. Al-Tahaineh, The effect of coupling a flat-plate collector on the solar still productivity. Desalination, 2005. 183(1-3): p. 137-142.

131. Bergman, T.L., A. S. Lavine, F. P. Incropera and D. P. Dewitt, Fundamentals of heat and mass transfer. 2011, John Wiley & Sons New York.

132. Khakrah, H., A. Shamloo, and S.K. Hannani, Exergy analysis of parabolic trough solar collectors using Al2O3/synthetic oil nanofluid. Solar Energy, 2018. 173: p. 1236-1247.

133. Aboul-Enein, S., A.A. El-Sebaii, and E. El-Bialy, Investigation of a single-basin solar still with deep basins. Renewable Energy, 1998. 14(1): p. 299-305.

134. Anderson, T.N., Investigation of thermal aspects of building integrated photovoltaic/thermal solar collectors. 2009, The University of Waikato.

135. Madhlopa, A., Development of an advanced passive solar still with separate condenser. 2009, The University of Strathclyde.

136. Nishioka, K., K. Miyamura, Y. Ota and M. Akitomi, Accurate measurement and estimation of solar cell temperature in photovoltaic module operating in real environmental conditions. Japanese Journal of Applied Physics, 2018. 57(8S3): p. 08RG08.

137. Keysight, 34970A Data Acquisition/Switch Unit Family. 2020, Keysight.

138. Adhikari, R.S., A. Kumar, and A. Kumar, Estimation of mass-transfer rates in solar stills. International Journal of Energy Research, 2007. 14(7): p. 737-744.

139. Setoodeh, N., R. Rahimi, and A. Ameri, Modeling and determination of heat transfer coefficient in a basin solar still using CFD. Desalination, 2011. 268(1): p. 103-110.

140. Hammami, M., M. Mseddi, and M. Baccar, Numerical study of coupled heat and mass transfer in a trapezoidal cavity. Engineering Applications of Computational Fluid Mechanics, 2007. 1(3): p. 216-226.

141. Rincón-Casado, A., F. J. ánchez de la Flor, E. Chacón Vera, J. Sánchez Ramos, New natural convection heat transfer correlations in enclosures for building performance simulation. Engineering Applications of Computational Fluid Mechanics, 2017. 11(1): p. 340-356.

142. Flack, R.D., The Experimental measurement of natural convection heat transfer in triangular enclosures heated or cooled from below. Journal of Heat Transfer, 1980. 102(4): p. 770-772.

143. Poulikakos, D. and A. Bejan, Natural convection experiments in a triangular enclosure. Journal of Heat Transfer, 1983. 105(3): p. 652-655.

144. Altaç, Z. and N. Uğurlubilek, Assessment of turbulence models in natural convection from two- and three-dimensional rectangular enclosures. International Journal of Thermal Sciences, 2016. 107: p. 237-246.

145. User manual, F., Release 16.1. ANSYS Inc, 2015.

146. Nijegorodov, N., P.K. Jain, and S. Carlsson, Thermal-electrical, high efficiency solar stills. Renewable energy, 1994. 4(1): p. 123-127.

147. Raffel, M., C. E. Willert, F. Scarano, C. J. Kähler, S. T. Wereley and Kompenhans, J. Particle image velocimetry: a practical guide. 2018: Springer.

148. Chung, S.-K. and S.K. Kim, Digital particle image velocimetry studies of nasal airflow. Respiratory physiology & neurobiology, 2008. 163(1-3): p. 111-120.

149. Sharpley, B. and L. Boelter, Evaporation of water into quiet air from a one-foot diameter surface. Industrial & Engineering Chemistry, 1938. 30(10): p. 1125-1131.

150. Rabhi, K., Experimental performance analysis of a modified single-basin single-slope solar still with pin fins absorber and condenser. Desalination, 2017. 416: p. 86-93.

151. Manoj Kumar, P., D. Sudarvizhi and K.B. Prakash, Investigating a single slope solar still with a nano-phase change material. Materials Today: Proceedings, 2021. 45: p. 7922-7925.

152. Attia, M.E.H., A.K. Hussein, S.K. Rout and J. Soliman, Experimental Study of the Effect of Al 2 O 3 Nanoparticles on the Profitability of a Single-Slope Solar Still: Application in Southeast of Algeria, in Advances in Air Conditioning and Refrigeration. 2021, Springer. p. 119-133.

153. Acharya, F.M.S., natural convection in trapezoidal cavities with baffles mounted on the upper inclined surfaces. Numerical Heat Transfer, Part A: Applications, 2000. 37(6): p. 545-565.

154. Varol, Y., H.F. Oztop, and A. Varol, Effects of thin fin on natural convection in porous triangular enclosures. International Journal of Thermal Sciences, 2007. 46(10): p. 1033-1045.

155. Rashidi, S., J. Abolfazli Esfahani, and N. Rahbar, Partitioning of solar still for performance recovery: Experimental and numerical investigations with cost analysis. Solar Energy, 2017. 153: p. 41-50.

156. Rashidi, S., M. Bovand, and J.A. Esfahani, Optimization of partitioning inside a single slope solar still for performance improvement. Desalination, 2016. 395: p. 79-91.

157. Asan, H. and L. Namli, Numerical simulation of buoyant flow in a roof of triangular cross-section under winter day boundary conditions. Energy and Buildings, 2001. 33(7): p. 753-757.

158. Sharpley, B.F. and L.M.K. Boelter, Evaporation of water into quiet air from a one-foot diameter surface. Industrial & Engineering Chemistry, 1938. 30(10): p. 1125-1131.

159. Tiwari, A.K. and G.N. Tiwari, Thermal modeling based on solar fraction and experimental study of the annual and seasonal performance of a single slope passive solar still: The effect of water depths. Desalination, 2007. 207(1): p. 184-204.

160. Panchal, H., et al.,

Sathyamurthy, Ravishankar A. E. Kabeel, S. A. El-Agouz, D. Rufus, T. Arunkumar, A. Muthu Manokar, D. P. Winston, A. Sharma, N. Thakar, K. K. Sadasivuni, Annual performance analysis of adding different nanofluids in stepped solar still. Journal of Thermal Analysis and Calorimetry, 2019. 138(5): p. 3175-3182.

161. Fath, H.E.S., M. El-Samanoudy, K. Fahmy and A. Hassabou, Thermal-economic analysis and comparison between pyramid-shaped and single-slope solar still configurations. Desalination, 2003. 159(1): p. 69-79.

Appendices

Appendix A: Dry air, humid air and brine water thermal properties

To run the mathematical model developed to analyse the performance of SS solar still, the bellow empirical equations have been used to determine the physical properties of dry air, brine water and humid air have as function of temperature [165].

Table 5: Dry air

Specific heat (Cp_{air})	$1055.05 - 0.3475\mathrm{T} + 6.25 \times 10^{-4}\mathrm{T}^2$
Density (ρ_{air})	$353/(T + 273.15)$
Conductivity (λ_{air})	$0.0242 + 7.57 \times 10^{-5}T$
Dynamic viscosity (μ_{air})	$1.7176 \times 10^{-5} + 0.46 \times 10^{-7}T$
Thermal diffusivity (a_{air})	$1.8343 \times 10^{-5} + 0.146 \times 10^{-6}T$
Prandtl number (Pr_{air})	$0.7147 + 0.254 \times 10^{-3}T$
Thermal expansion (a_{air})	$= 1/(T + 273.15)$

Table 6: Brine water (3.5% salt concentration)

Specific heat (Cp_W)	$3958 - 52.3 + 0.837T$
Density (ρ_W)	$1002.6 - 0.505 \times 10^{-1}T - 0.38 \times 10^{-2}T^2$
Conductivity(λ_W)	$0.5536 + 2.238 \times 10^{-3}T - 9.87 \times 10^{-6}T^2$
Kinematic viscosity (ν_W)	$17.199 \times 10^{-4} - 0.3389 \times 10^{-4}T^2$ $+ 0.2 \times 10^{-6}T^3$
Prandtl number (Pr_W)	$12.501 - 0.261T + 1.577 \times 10^{-3}T^2$
Thermal expansion (β_{water})	$1.6 \times 10^{-5} + 9.6 \times 10^{-6}T$

Table 7: Properties of humid air

Dynamic viscosity (μ_{hair})	$1.718 \times 10^{-5} + 4.620 \times 10^{-8} \times T$
Thermal expansion (a_{hair})	$\lambda_{hair}/\rho_{hair} \times Cp_{hair}$
Specific heat (Cp_{hair})	$999.2 + 0.1434 \times T + 1.10 \times 10^{-4}T^{-2} - 6.7581 \times 10^{-8}T^{-3}$
Conductivity (λ_{hair})	$0.0244 + 0.7673 \times 10^{-4}T$
Thermal expansion (β_{hair})	$1/(T + 273.15)$
Density (ρ_{hair})	$353.44/(T + 273.15)$

Appendix B: Uncertainty

In the current research, both outdoor and indoor experiments have been carried out to investigate the productivity of SS solar still and validate CFD model. Knowing that every experimental work is subjected to uncertainties, evaluating their variation is paramount to measure accuracy and reliability of experimental results.

Temperature and yield measurement:

In the current research, outdoor and indoor experiments have been performed. For both experiments, the temperature of surfaces, ambient and water layer were measured using a series of 14 copper constantan (Type-T) thermocouples. Data was then collected using a Keysight data logger for outdoor experiments and Picolog for indoor (PIV) experiment. Using a thermal bath, the thermocouples were calibrated using a platinum resistance thermometer, having an accuracy of ±0.02C.

To measure the yield produced by the fabricated solar distillation system, a graduated cylinder of 3 litters was used, and the uncertainty in reading the instrument was approximatively ±5 ml.

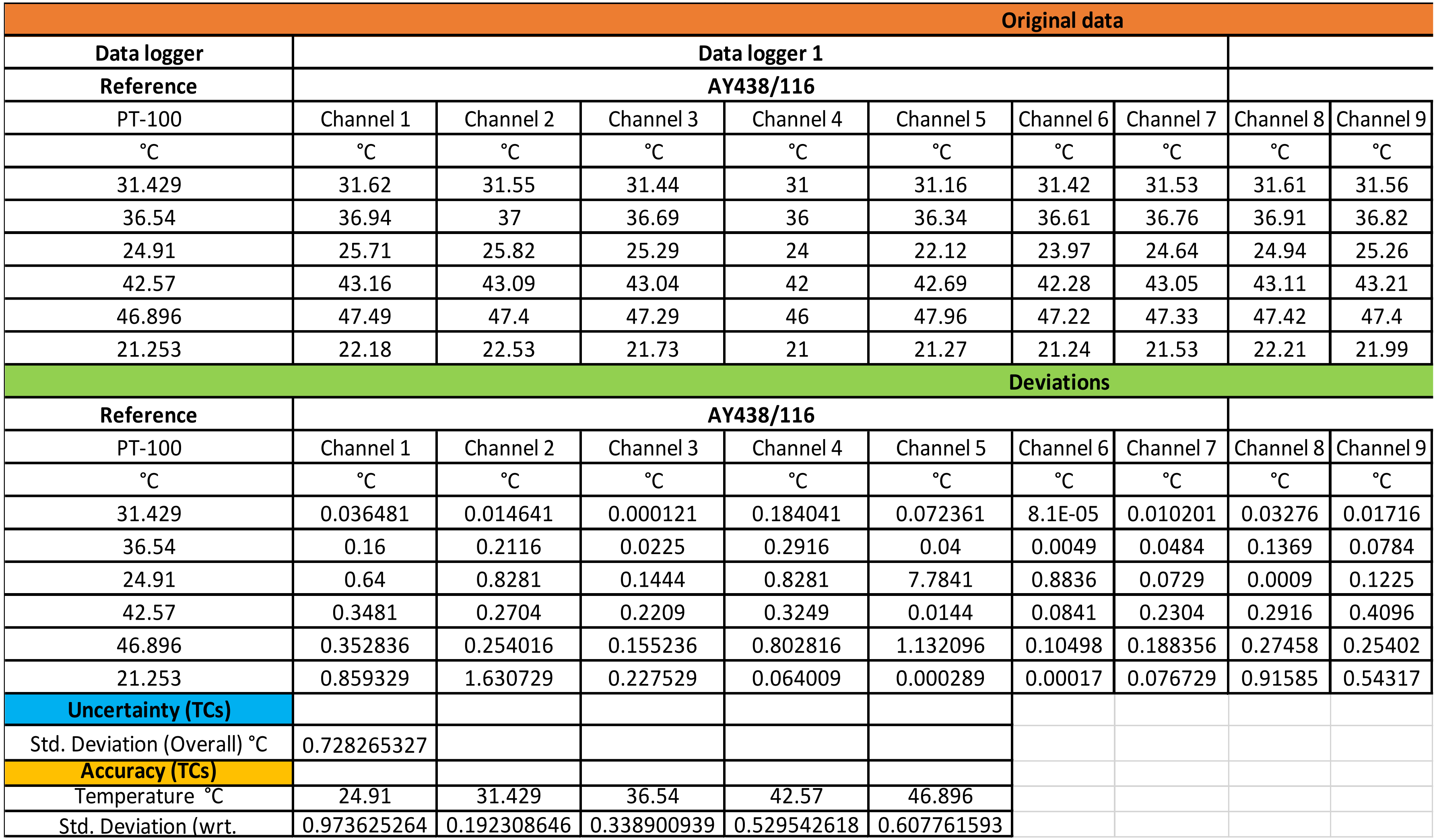

Original data									
Data logger	**Data logger 1**								
Reference	**AY438/116**								
PT-100	Channel 1	Channel 2	Channel 3	Channel 4	Channel 5	Channel 6	Channel 7	Channel 8	Channel 9
°C	°C	°C	°C	°C	°C	°C	°C	°C	°C
31.429	31.62	31.55	31.44	31	31.16	31.42	31.53	31.61	31.56
36.54	36.94	37	36.69	36	36.34	36.61	36.76	36.91	36.82
24.91	25.71	25.82	25.29	24	22.12	23.97	24.64	24.94	25.26
42.57	43.16	43.09	43.04	42	42.69	42.28	43.05	43.11	43.21
46.896	47.49	47.4	47.29	46	47.96	47.22	47.33	47.42	47.4
21.253	22.18	22.53	21.73	21	21.27	21.24	21.53	22.21	21.99
Deviations									
Reference	**AY438/116**								
PT-100	Channel 1	Channel 2	Channel 3	Channel 4	Channel 5	Channel 6	Channel 7	Channel 8	Channel 9
°C	°C	°C	°C	°C	°C	°C	°C	°C	°C
31.429	0.036481	0.014641	0.000121	0.184041	0.072361	8.1E-05	0.010201	0.03276	0.01716
36.54	0.16	0.2116	0.0225	0.2916	0.04	0.0049	0.0484	0.1369	0.0784
24.91	0.64	0.8281	0.1444	0.8281	7.7841	0.8836	0.0729	0.0009	0.1225
42.57	0.3481	0.2704	0.2209	0.3249	0.0144	0.0841	0.2304	0.2916	0.4096
46.896	0.352836	0.254016	0.155236	0.802816	1.132096	0.10498	0.188356	0.27458	0.25402
21.253	0.859329	1.630729	0.227529	0.064009	0.000289	0.00017	0.076729	0.91585	0.54317
Uncertainty (TCs)									
Std. Deviation (Overall) °C	0.728265327								
Accuracy (TCs)									
Temperature °C	24.91	31.429	36.54	42.57	46.896				
Std. Deviation (wrt.	0.973625264	0.192308646	0.338900939	0.529542618	0.607761593				

Figure 90: Thermocouples calibration data.

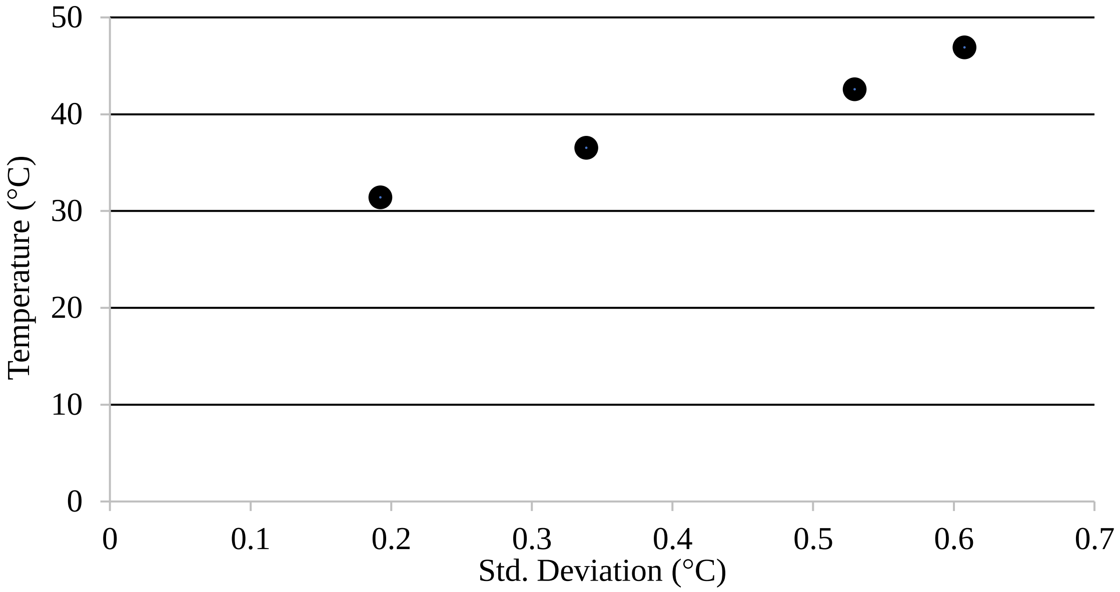

Figure 91: Standard deviation of themocpuples calibration test.

Irradiation and wind measurements

In order to measure solar irradiation and wind velocity in both outdoor experiments of SS solar still with and without the baffle, calibrated sunshine pyranometer type SPN1 from Delta- T Devices and S-WSA-M003 anemometer have been used. Using Keysight 34970A Data Acquisition system, data of total solar irradiation, diffuse radiation and wind speed were recorded and saved. Table 8 and 9 presents the pyranometer and anemometer specifications and uncertainties of solar irradiation and wind speed readings.

Table 8: Pyranometer specifications and accuracy (SPN1-Delta- T Devices)

Overall accuracy: Total (Global) and Diffuse radiation	±5% Daily integrals ±5% ±10 W/m^2 Hourly averages ±8% ±10 W/m^2 Individual readings
Resolution	0.6 W/m^2 = 0.6 mV
Range	0 to >2000 W/m^2
Analogue output sensitivity	1 mV = 1 W/m^2
Analogue output range	0 – 2500 mV
Sunshine status threshold	120 W/m^2 in the direct beam

Table 9: Anemometer specifications and accuracy

Measurement range	0 to 45 m/s
Operating Temperature Range	-40° to 75°C
Accuracy	±4% Individual readings
Resolution	0.38 m/s
Starting Threshold	1 m/s